UC Berkeley
UC Berkeley Electronic Theses and Dissertations

Title
Metal Oxide Nanostructured Materials for Optical and Energy Applications

Permalink
https://escholarship.org/uc/item/1tm116g5

Author
Moore, Michael Christopher

Publication Date
2013

Peer reviewed|Thesis/dissertation

eScholarship.org Powered by the California Digital Library
University of California

Metal Oxide Nanostructured Materials for Optical and Energy Applications

by

Michael Christopher Moore

A dissertation submitted in partial satisfaction
of the requirement for the degree of
Doctor of Philosophy

in

Chemistry

in the

Graduate Division

of the

University of California, Berkeley

Committee in Charge:
Professor Peidong Yang, Chair
Professor Gabor Samorjai
Professor Junqiao Wu

Spring 2013

Metal Oxide Nanostructured Materials for Optical and Energy Applications

Portions of Chapter 2 © 2010 American Chemical Society
Portions of Chapter 3 © 2011 The Royal Society of Chemistry
All other chapters © 2013 Michael Christopher Moore

Abstract

Metal Oxide Nanostructured Materials for Optical and Energy Applications

by
Michael Christopher Moore
Doctor of Philosophy in Chemistry

University of California, Berkeley

Professor Peidong Yang, Chair

With a rapidly growing population, dwindling resources, and increasing environmental pressures, the need for sustainable technological solutions becomes more urgent. Metal oxides make up much of the earth's crust and are typically inexpensive materials, but poor electrical and optical properties prevent them from being useful for most semiconductor applications. Recent breakthroughs in chemistry and materials science allow for the growth of high-quality materials with nanometer-scale features and high surface-to-volume. These nanostructured materials exhibit new and enhanced properties that lead to acceptable performance from previously unsuitable materials or decreased amounts of high-performance materials. Because the fundamental length scales of optical, electrical, and thermal phenomena lie on the nanometer-scale, nanostructured materials present an opportunity to independently enhance or disrupt these properties. Through the careful selection of material composition, morphology, and dimensions, we can design materials for specific applications, such as optics or energy generation and storage.

The integration of high-bandwidth photonic devices with silicon microchips is essential to continue pace with the increases of processing power predicted by Moore's Law. However, there is a large mismatch in the size of electronic and photonic devices, due to the difficulty of confining infrared wavelengths to the nanometer length scale. Nanowires with diameters as small as 200 nm have been shown to be capable of waveguiding visible and UV wavelengths. Zinc oxide nanodisks were grown using a bottom-up synthesis and investigated as optically-pumped UV laser source with dimensions smaller than the free-space wavelength of light (sub-wavelength). Plasmon-enhanced photoluminescence and p-type doping were also investigated in consideration of fabricating a functional laser diode.

Semiconductor alloying has long been a tool for designing materials with specific optical and electronic properties, but growing tunable alloy nanowires require complex syntheses. As an alternative, solid state conversion chemistry allows for the decoupling of the nanowire synthesis and the alloying procedure. This method allows for for bottom up, large scale preparation of complex metal oxide alloys with a high level of control over nanowire morphology, composition, and properties. Conversion chemistry for complex metal oxide nanowires is demonstrated in two material systems, with potential applications in thermoelectrics and photoelectrochemical water splitting.

Thermoelectric materials have generated interest as a means of increasing the efficiency of power generation through the scavenging of waste heat. Alloys of zinc oxide and indium oxide (and other tri-valent oxides) form a complex crystal structure with inherent features on the nanoscale that enhance phonon scattering and are ideal for thermoelectrics. Conversion chemistry provides simple method to prepare $In_{2-x}M_xO_3(ZnO)_n$ (M = In, Ga, Fe, n = integer) nanowires from ZnO nanowires. Single-nanowire thermal and electrical measurements on $In_{2-x}Ga_xO_3(ZnO)_n$ reveal a simultaneous improvement in all contributing factors to the thermoelectric figure of merit, giving an order of magnitude enhancement over similar bulk materials at room temperature.

The increasing environmental concerns associated with fossil fuels motivates the development of technology to inexpensively capture and store solar energy. Photoelectrochemical water splitting uses semiconductor materials to absorb sunlight and produce hydrogen and oxygen from water. Rutile, a form of titanium dioxide, is capable of water photolysis under certain conditions, but its wide band gap prevents it from being a practical solution. Through a conversion chemistry scheme, rutile TiO_2 nanowires are reacted with transition metal oxides to form ilmenite nanowires, $ATiO_3$ (A = Mn, Fe, Co, Ni). When A is sub-stoichiometric, $ATiO_3$-decorated TiO_2 nanowires or periodic heterojunction nanowires are formed. $CoTiO_3$ and $NiTiO_3$ are evaluated as potential photoanode and catalyst materials for water oxidation.

For my father, Bill.

Contents

List of Figures and Tables iv

List of Abbreviations vi

1. Introduction 1

1.1. A brief introduction to semiconductors 1
1.2. Nanostructured materials 4
1.3. Nanophotonics 6
1.4. Thermoelectric generators 9
1.5. Photoelectrochemistry and solar fuels 10

2. Zinc oxide nanolasers 14

2.1. Introduction 14
a. Optical properties of zinc oxide 15
b. Zinc-oxide-based lasers 17
c. p-Type zinc oxide 18
2.2. Synthesis of ZnO nanostructures 19
a. ZnO nanowires 19
b. Procedure for in situ doping of ZnO nanowires 20
c. Procedure for Au-colloid-grown ZnO nanowires 20
d. Patterned substrates for VLS ZnO nanowires 21
e. ZnO pillars and nanodisks 22
2.3. Lasing of ZnO nanodisks 23
2.4. Metal-enhanced photoluminescence 32
2.5. p-Type lithium-doped ZnO nanowires 35

3. Indium oxide–zinc oxide alloy nanowires 40

3.1. Introduction 40
3.2. Conversion synthesis of indium-zinc-oxide-structured nanowires 43
3.3. Typical methods for conversion synthesis 45
3.4. Structural analysis 46
a. Structural analysis of IGZO nanowires 46
b. Structural analysis of IFZO nanowires 51
c. Structural analysis of IZO nanowires 53
d. Structural analysis of other MZO nanowire compositions 57
3.5. Mechanism of conversion synthesis 58
3.6. Optical Properties 61
3.7. Transport properties 63

4. Titanium oxide-ilmenite nanowires **67**

4.1. Introduction 67
4.2. Synthesis of rutile-ilmenite nanowires 69
4.3. Structural analysis of rutile-ilmenite nanowires 70
4.4. Optical and photoelectrochemical properties 75

5. Concluding Remarks **78**

Bibliography **79**

List of Figures and Tables

Figure 1.1: Direct and indirect band gap. 2
Figure 1.2: Quantum confinement effect in nanoparticles. 5
Figure 1.3: Nanowire waveguides and color filtering. 7
Figure 1.4: Energy schemes for photocatalytic water splitting. 11
Figure 1.5: Band positions of various semiconductors at pH 1. 12
Figure 1.6: Tandem (z-scheme) water photolysis system. 13

Figure 2.1: ZnO wurtzite crystal structure. 15
Figure 2.2: Absorbance and photoluminescence in ZnO. 16
Figure 2.3: EQE of ZnO nanowires depend on the excitation power density. 16
Figure 2.4: Lasing in single ZnO nanowires. 18
Figure 2.5: Patterning with nanoimprint lithograpy. 22
Figure 2.6: ZnO nanowire patterning. 22
Figure 2.7: Zinc vaporization synthesis and products. 23
Figure 2.8: Whispering gallery mode lasing in ZnO nanodisks. 24
Figure 2.9: Room temperature lasing of ZnO nanodisks with various diameters. ...26
Table 2.1: Summary of diameter dependence of ZnO nanodisk lasing thresholds at room temperature. 27
Table 2.2: Lasing thresholds of ZnO nanowires and pillars. 27
Figure 2.10: Multi-mode lasing in a ZnO disk. 28
Figure 2.11: Lasing properties of sub-wavelength ZnO nanodisks at 8 K. 29
Figure 2.12: WGM simulations of a sub-wavelength ZnO nanodisk. 31
Table 2.3: Leakage Power Ratio. 32
Figure 2.13: Surface-plasmon enhancement of PL emission in ZnO/Al_2O_3/Au. ...33
Figure 2.14: PL enhancement of ZnO by Al and other metals 34
Figure 2.15: PL and lasing emission in Al-coated ZnO nanodisks. 34
Figure 2.16: SEM images of Li_3N-doped ZnO nanowires. 35
Figure 2.17: Characterization of ZnO:Li nanowires. 36
Figure 2.18: Single-nanowire FET devices for carrier concentration determination. 37
Figure 2.19: p-Type behavior in ZnO nanowires after thermal activation. 39

Figure 3.1: Phase diagram of In_2O_3-ZnO system. 41
Figure 3.2: Indium octahedral layer. 41
Figure 3.3: Zigzag modulation layers. 42
Figure 3.4: Schematic illustration of the synthetic method. 44
Figure 3.5: MZO nanowires...44
Figure 3.6: ZnO nanowire arrays. 45
Figure 3.7: Unannealed metal-coated ZnO nanowires. 46
Figure 3.8: XRD and SEM of IGZO nanowire arrays. 47

Figure 3.9: IGZO nanowires. 48
Figure 3.10: EDS Mapping of IGZO nanowires. 48
Figure 3.11: HR-STEM of IGZO nanowires. 49
Figure 3.12: IGZO metal coating thickness dependence. 50
Figure 3.13: IFZO metal coating thickness dependence. 51
Figure 3.14: IFZO nanowire tips. 52
Figure 3.15: Varying In:Fe in IFZO. 53
Figure 3.16: IZO nanowires. 54
Figure 3.17: IZO nanowires prepared after metal oxidation. 54
Figure 3.18: TEM of annealed nanowires by sealed-tube method. 55
Figure 3.19: SEM of annealed nanowire arrays by sealed-tube method. 56
Figure 3.20: "Sandwich" Annealing of IZO. 57
Figure 3.21: Non-indium-containing MZO nanowires. 57
Table 3.1: Literature annealing conditions of various bulk MZO compositions. 58
Figure 3.22: Edge dislocations at partial layers. 59
Figure 3.23: Schematic diagram of the ZnO nanowire surface in IZO formation. 61
Figure 3.24: UV-visible absorption spectra of ZnO and MZO bulk powders. 62
Figure 3.25: UV-visible absorption and PL spectra of ZnO and MZO nanowire arrays. 63
Figure 3.26: Single-nanowire electrical measurements. 64
Figure 3.27: Thermoelectric measurements. 66

Figure 4.1: Ilmenite crystal structure. 68
Figure 4.2: Computational study of OER activity for doped rutile materials. 68
Figure 4.3: Chemical bath deposition of metal hydroxide coatings. 70
Figure 4.4: Rutile nanowires with various titanate surface particles. 71
Figure 4.5: Heterojunction segmented nanowires. 72
Figure 4.6: Quaternary $Co_{0.5}Ni_{0.5}TiO_3$ nanowires. 73
Figure 4.7: Fully-converted $CoTiO_3$ nanowires. 74
Figure 4.8: Absorbance spectra of ilmenite-rutile nanowires. 75
Figure 4.9: Overpotential required for water oxidation for ATiO$_3$ nanowire electrodes. 76
Figure 4.10: Oxygen evolution of ATiO$_3$-decorated rutile nanowires under illumination. 77

List of Abbreviations

CB	conduction band
CBD	chemical bath deposition
CNTO	cobalt nickel titanium oxide, $Co_{1-x}Ni_xTiO_3$
CTO	cobalt titanium oxide, $CoTiO_3$
CVT	chemical vapor transport
DFT	density functional theory
E_g	band gap energy
EDS	energy dispersive x-ray spectrometry
EJ	exajoule
EQE	external quantum efficiency
FDTD	finite difference time domain
FET	field-effect transistor
FP	Fabry-Pérot
FWHM	full width-half maximum
GZO_n	gallium zinc oxide, $Ga_2O_3(ZnO)n$
HER	hydrogen evolution reaction
IDB	inversion domain boundary
$IFZO_n$	indium iron zinc oxide, $In_{2-x}Fe_xO_3(ZnO)_n$
$IGZO_n$	indium gallium zinc oxide, $In_{2-x}Ga_xO_3(ZnO)_n$
IR	infrared
IZO_n	indium zinc oxide, $In_2O_3(ZnO)n$
LEDs	light-emitting diode(s)
MBE	molecular beam epitaxy
MTO	manganese titanium oxide, $MnTiO_3$
MZO	*metal* zinc oxide, $R_{2-x}M_xO_3(ZnO)_n$
NTO	nickel titanium oxide, $NiTiO_3$
NWs	nanowire(s)
OD/ID	outer diameter/inner diameter
OER	oxygen evolution reaction
PEC	photoelectrochemical
PL	photoluminescence
PMMA	poly(methyl methacrylate)
SEI	semiconductor-electrolyte interface
SEM	scanning electron microscopy
STEM, (HR)-	scanning transmission electron microscopy, (high resolution-)
sub-λ	sub-wavelength
TEM, (HR)-	transmission electron microscopy, (high resolution-)
UV	ultraviolet
VB	valance band
VLS	vapor-liquid-solid
WG(M)	whispering gallery (mode)
XPS	x-ray photoelectron spectroscopy
XRD	x-ray diffraction
zT	thermoelectric figure of merit

Acknowledgements

Foremost, I would like to thank my advisor, Professor Peidong Yang, for giving me the opportunity to work in his group during the past six years. His guidance and insight pushed me to become a better scientist. His dedication to science will be an inspiration for me, wherever my career takes me.

I owe many of my successes to my tremendously helpful and friendly coworkers in the Yang Group. My work would not have been possible without the insight and expertise of my numerous collaborators: Sean Andrews, Dan Gargas, Anna Goldstein, Melissa Fardy, Tomas Larsson, Bin Liu, Hanwei Gao, Ben Yuhas, Hung-ta Wang, Eugenia Toimil-Molares, and Ruoxue Yan. In addition, Chris Hahn, Marty Mulvihill, Joel Henzie, and Neil Dasgupta have been indispensable for scientific, career, and personal support. The Yang Group is a fountain of brilliant, talented people and I'm honored to been part of something special. Additionally, I am thankful for the other members of the 2007 cohort of the Yang Group: Chris Hahn, Sean Andrews, Brian Moshofsky, Ilan Jen-La Plante, and Trevor Ewers (an honorary member). It's amazing that we all survived our first semester, which surely would have been easier without the all-nighters, crazy antics, and Curveball, but also less memorable. I wish them all the best in their careers.

I have made many valuable friendships along the way on this very long academic journey and I wish I could thank all of them for their personal support and encouragement. I want to thank Professors Norman Craig and Martin Ackermann for starting me on my path, as well as their continuing mentorship and wisdom. Outside of lab, I'm grateful for Gavin Platt, Jasmine McCammon, Michael Goldrich, Keoki Seu, and Dusty Garrison, who have helped me make the most of my time in California; Darcy Gervasio, Kate Oberg, and Sara Paule, who have helped me keep my sanity during long phone calls; and Ashley Russell for all of the mid-day coffee breaks.

I owe everything to my family– Tukta, Dawn, and Kathy– who have remained supportive and patient as I have moved increasingly farther away from home in pursuit of education and science. I'm also grateful of all of the support from my father and grandparents, who were unable to see me finish my formal academic training, but encouraged me to never stop learning.

And finally, I want to thank my wife, my love, and my partner in crime, Alyssa, who has endured the late nights, erratic schedule, unending stress, and general insanity of my time in graduate school. I could not have done it with you. I look forward to a long and peaceful life together.

1. Introduction

Nanostructured materials are now one of the most active research areas in chemistry, physics, and engineering. This can be observed by the rapid growth in published papers per year containing the *nano-* prefix: 165,000 new publications were recorded in 2012, compared to 25,000 in 2000 and 2,000 in 1990[1]. One explanation of this trend is the promise that nanomaterials may let us do more with less input during a time period that has been marked by a rapidly growing population, dwindling resources, and increasing environmental pressures.

The goal of this dissertation is to demonstrate the utility of metal oxide nanostructured materials engineered for specific applications. In the first case, single nanostructures for nanoscale laser emitters are engineered to be as small as possible so that they may be integrated with microelectronics. In the latter two cases, materials are designed for energy applications: harnessing thermal energy to generate electricity and harnessing solar energy to drive electrochemical reactions for fuel production. While these devices harness phenomena on the nanoscale, the materials synthesis and availability must ultimately be scaleable to gigawatt- or terawatt-scale to be practical. Metal oxides are abundant and inexpensive, but typically are not useful as semiconductors in their bulk form and must be nanostructured to be potentially useful. This chapter will introduce some important concepts behind nanostructured semiconductor materials and the discussed applications. The following chapters will focus on specific material systems chosen for each application, how they are grown on the nanoscale, and how the properties are tailored for each application.

1.1. A brief introduction to semiconductors

Unlike an atomic or molecular system, the electronic structure of an extended solid consists of bands that form a continuum of energy states, in which electrons or holes (carriers) can move freely. Electrons populate the bands, filling the lowest energy states first, up to the chemical potential (or Fermi level) of the system. Metals exhibit high conductivity because the Fermi level is position so that a band is half-full and carriers can move freely. The defining characteristic of a semiconductor is a band gap (E_g), in which the Fermi level is positioned between two bands so that one is filled with electrons (valance band, VB) and the other is unpopulated (conduction band, CB), as shown in (Figure 1.1).

Conductivity in a semiconductor is a function of the size of the band gap and are considered insulators when the band gap exceeds ~3.5 eV. In semiconductors, carriers can be excited into the conduction band by thermal energy alone and conductivity increases with temperature.

1. Source: Thomson Reuters Web of Knowledge

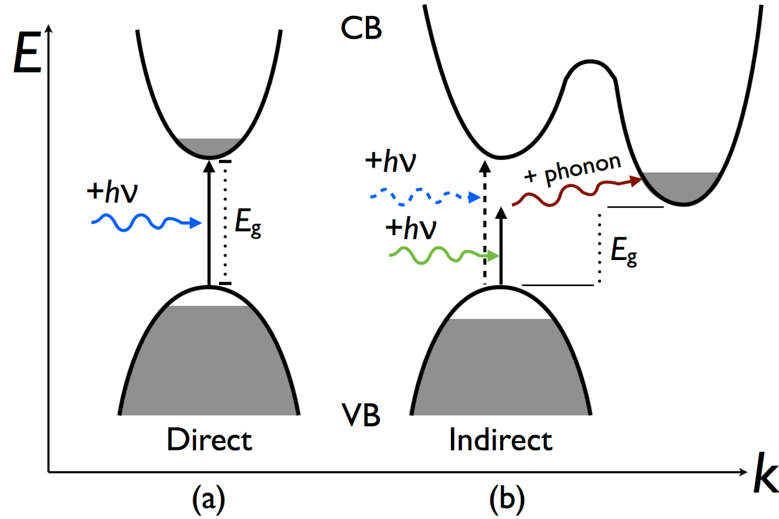

Figure 1.1: Direct and indirect band gap. Illustration of the valance band (VB) and conduction band (CB) in direct (**a**) and indirect (**b**) semiconductors. The gray regions indicates electron population at room temperature. The indirect semiconductor, as depicted, has a smaller band gap and thus has more electrons populating the conduction band. **a**) A photon ($h\nu$) with energy greater than the band gap, E_g, is absorbed to create an electron-hole pair. **b**) A photon ($h\nu > E_g$) can be absorbed with the simultaneous annihilation of a phonon to impart momentum to the electron. A direct band gap can be accessed with higher energy photons (dotted line).

The thermal population of energy bands and states are governed by the Fermi-Dirac distribution and the thermal energy available at a given temperature: $k_B T$ = 0.026 eV at room temperature. Thermal energy is stored in the lattice in the form of quantized lattice vibration (phonons), which are consumed to excite carriers to higher intraband energy states and emitted when carriers move to a lower intraband energy state. To further improve conductivity, semiconductors can be doped with other elements (impurities) introduce new energy bands within the band gap, either slightly below the conduction band (n-type) or slightly above the valance band (p-type), as well as an increase or decrease in the Fermi level, respectively. In the n-type case, the Fermi level is positioned such that defect band is populated with electrons, which are easily excited into the nearby CB. Ultimately, the conductivity of a material is determined by the carrier concentration and mobility, which is a material parameter dependent on the lifetime and effective mass of carriers in the material.

Semiconductors are an extremely broad and rich class of solid materials. While there are a few elements that are inherently semiconductors (silicon and germanium), many semiconductors are binary or multicomponent materials, such as GaAs and CdS. Some semiconductors may be alloyed to form materials with properties intermediate of the input materials, such as InGaN from InN and GaN. Oxide materials tend to have large band gaps due to high electronegativity of oxygen, which contributes to low-laying valance band positions. Some metal oxide materials can be considered semiconductors, such as Cu_2O (2.2 eV), Fe_2O_3 (2.2 eV), TiO_2 (3.0-3.2 eV), and ZnO (3.34 eV), although many of these materials have low hole mobility, again, due to the oxygen character of the valance band.

In materials with a *p*-orbital-like valance band and *s*-like conduction band (or vise-versa), photons with an energy equal to or greater than the band gap can be absorbed to promote an

electron to the conduction band and creating a hole in the valance band, known as an electron-hole pair (Figure 1.1). When an electron and hole encounter one another, they annihilate and release a photon equal to the band gap energy, through recombination. Recombination can also occur non-radiatively, meaning the energy is released as phonons. Absorption occurs readily when the conduction band minimum and valance band maximum have the same position in momentum-(k)-space, known as a direct band gap (Figure 1.1a). In an indirect band gap material (such as silicon), photons cannot be absorbed without a simultaneous interaction with a phonon to supply momentum (Figure 1.1b). This multi-particle requirement greatly reduces absorption and eliminates emission for indirect materials, but other local minima and maxima in the band diagram can act as a direct band gap for improved absorption at higher energies.

Rather than forming free electrons and holes, the electron-hole pair can also exist in a stable configuration known as an exciton, where the electron and hole are loosely bound by Coulombic attraction. This attraction is hydrogen-like and the stabilization energy and bonding radius can be modeled by the Bohr equation. Because of the small effective masses of the electron and hole, the binding energy is weak and is typically on the order of 0.01 eV. Exciton binding energy and Bohr radius are inversely related and typical Bohr exciton radii are ~10 nm. Excitonic effects are important in optical applications, as the exciton enhances absorption at the band gap and increases the average lifetime of an electron-hole pair (due to the difficulty of losing the excitonic energy and relaxing to the CB minimum). Because of the small binding energies, excitons are easily dissociated by the thermal energy available at room temperature and thus excitonic effects are typically only observed at low temperature.

While semiconductor bulk crystals are often grown by crystallization from a molten source, complex semiconductor compositions and thin films are typically prepared by epitaxial growth on a crystalline substrate from a vapor-phase precursor. Epitaxy refers to the growth of a single-crystal material as a continuation of a crystalline wafer or surface (substrate). When growing a film with the same composition as the substrate (homoepitaxy), there is no lattice mismatch and the growth is a perfect continuation of the substrate crystal. However, it is often necessary or desirable to grow an interface of two different materials (heteroepitaxy), which requires careful matching of the crystal structure and lattice parameters. Even in interfaces with a modest amount of lattice mismatch, dislocations and other crystal defects may form in the growth layer, which lead to non-radiative recombination centers that reduce optical quality or trap states that reduce electrical transport. Vapor-phase precursors can be supplied by many methods: evaporation of a solid or liquid source (chemical vapor transport or thermal evaporation), decomposition of a molecular precursor (chemical vapor deposition), a thermal beam of atoms or molecules (molecular beam epitaxy), or any number of physical vapor deposition methods, in which a solid target may be ablated by electron beam (e-beam evaporation), pulsed laser (pulsed laser deposition), or plasma (sputtering). While not all of these materials require high-temperature for vapor delivery, high-temperatures are necessary to promote the equilibrium growth of crystals at the substrate.

Another typical method for materials preparation is through solid state reaction of two crystals in direct contact. In perfect crystals, ions diffuse through the lattice by serially hopping from a lattice site into an adjacent empty site. To overcome the high activation energy of dissociating lattice bonds, the reaction must be heated to a significant fraction of the material melting point and maintained for hours or days. Crystal structures with pores or channels and lattice

defects, such as dislocations, can significantly increase diffusion rates by providing other diffusion mechanisms. The overall reaction rate can also be increased by increasing the interface area of the two reagents. Assuming all kinetic factors are overcome, the reaction will proceed to the most thermodynamically favorable product that minimizes free energy. A phase diagram can be used to predict the product of a solid state reaction for a given temperature, pressure, and composition.

The fundamental element of many semiconductor devices is the p-n junction, which is the building block of transistors, light emitting diodes (LEDs), solar cells, and integrated circuits. The p-n junction is an interface between p- and n-type semiconductors, which when contacted causes the free carriers to flow across the junction and recombine due to the potential difference of the electron-poor (p) and electron-rich (n) materials. As the free carriers are annihilated, a charge imbalance and electric field build up due to the ionized dopants of opposite charge in each material and prevent further current flow. Thus, the potential difference of two materials cannot be resolved and a built-in voltage exists. The size of the non-conductive carrier-depleted region (depletion region or space-charge region) is dependent on the concentration of free carriers in each material. By applying an external voltage larger than the built-in voltage, carriers are forced into the the space charge region until it is saturated and current can freely flow.

The simplest p-n junctions are formed by an abrupt and ordered interface between p- and n-type regions in the same host material (homojunction). A homojunction can be formed from a monolithic material that has been selectively treated to introduce dopants across the junction or by homoepitaxial growth. A heterojunction between p- and n-type semiconductors of different host materials may be necessary if both dopants are not available for a single system. Another use of heterojunctions is in p-i-n quantum wells, where *i* is an intrinsic layer with a band gap smaller than the surrounding p- and n-type regions. In a type I alignment, the CB and VB positions of the quantum well is straddled by the CB and VB of the larger band gap materials. The potential difference encourages injection and confinement of carriers to the emitter layer, which enhances recombination and emission.

1.2. Nanostructured materials

Nanostructures are vaguely defined as an engineered material with at least one dimension less than one micron. Given that the length scales of near-visible light (300-1000 nm); phonon mean free path (50-500 nm); proteins, transistors, Bohr exciton radius, and the electron mean free path (1-100 nm); and molecules (0.1-10 nm), one might define nanostructured materials as those engineered to match the size regime of optical, electronic, chemical, and biological phenomena. While we think of nanomaterials as a modern phenomena, unintentional use of nanoparticles have been observed in ceramics and stained glasses from as early as 400 AD (*1, 2*). Nanomaterials are also readily produced by incomplete combustion: while the discovery of the buckminsterfullerene was produced by pulsed laser (*3*), it turned out that carbon nanostructures could be collected from candle soot (*4*). However, it was not until the development of powerful electron microscopes, scanning tunneling microscopes, and atomic force microscopes in the 1970s and 1980s that we were able to detect and intentionally engineer nanostructured materials.

Figure 1.2: Quantum confinement effect in nanoparticles. Fluorescence of CdSe–CdS core–shell nanoparticles with a diameter of 1.7 nm (left, blue) up to 6 nm (right, red), giving evidence of the scaling of the semiconductor band gap with particle size. This image was adapted from reference (*5*).

Nanomaterials are most famously known for the quantum confinement effect, in which a material's emission and absorption properties are shifted to higher energies with decreasing size (Figure 1.2) (*5*). While a material's natural bandgap can be considered classically, quantum effects must be considered when the material dimensions are on the order of the electron wavefunction. Rather than a continuous band of energies, quantum confined materials have bands made of discrete energy levels that can be approximated by the particle in a box model using the electron effective mass. The additional energy associated with confinement increases the energy of the band gap. Instead of a continuous density of states, the density of states of a nanostructure has discontinuous jumps in population at each energy level.

While quantum confinement does lead to interesting new effects in the optical and electronic properties, the most important property of nanostructured materials is a high surface-to-volume ratio. Surfaces are important because the majority of chemical reactivity in materials simply because it interfaces with other chemical species, in addition to the breaking of the bulk symmetry and dangling bonds. For catalysts, which are often prepared from precious metals, a low surface-to-volume ratio means many of the atoms are locked away in the bulk and unreactive. The rates of charge transfer processes and solid-state diffusion occur at interfaces (two surfaces in contact) increase with better surface-to-volume ratio. Lattice strain in alloys or epitaxial interfaces can be relieved through lattice relaxation and restructuring at the surfaces, which is not possible in the bulk, leading to lower defect formation. For this reason and the high-quality syntheses typically used in nanomaterials growth, nanostructured materials are often single-crystalline and free of line and plane defects. This leads to improved mechanical properties, high compression and tensile strength, and better optical and electrical properties than bulk materials. With the enhanced properties of nanostructured materials, it is not only possible to use less of a given material to achieve the same level of performance, but to substitute other enhanced materials that are more abundant or inexpensive.

There are a number of synthetic techniques and mechanisms for producing nanostructured materials depending on the desired morphology, composition, and material quality. Solution-phase growth is a popular method for growing nanomaterials owning to its low-temperature, typically inexpensive precursors, and potential for scalability. Nanoparticles were first

prepared using the hot injection method, using time and precursor concentration to limit crystal growth to the nanoscale (*6*). However, optical and electrical devices demand high-quality materials grown and thus, many high-temperature vapor phase methods for epitaxial thin-film materials have been adapted for nanomaterials. While some crystal systems have a fast-growth direction and naturally favor one-dimension growth, it is typically necessary to use a metal catalyst to promote nanowire growth.

Vapor-liquid-solid (VLS) growth has been demonstrated in many semiconductor materials as a route to diameter-tunable high-quality single-crystalline nanowires (*7*). The growth substrate is coated with droplets of an inert metal, which melts and is liquid at the reaction temperature. Vapor-phase precursors dissolve into the liquid droplet and alloy with the liquid until the solubility limit. Once saturated, the droplet composition is in equilibrium, but continued impingement of precursor from the vapor-phase drives the precipitation of solid material with the nanowire morphology. Additionally, quantum dots have also been demonstrated with vapor phase growth by carefully selecting a substrate with lattice strain to promote island and particle growth, rather than thin film (*8*).

While the semiconductor and electronics industries are the most prominent beneficiaries of advances in nanostructured materials thus far, many fields may soon follow. The fundamental components for photonics for producing, guiding, and detecting light have already been demonstrated at the nanoscale (*9-11*). Nanowire-based artificial photosynthesis may eventually convert sunlight, water, and carbon dioxide directly into a storable liquid fuel (*12*). The cost-effective recovery of electricity from low quality waste heat may be possible with nanowire-based thermoelectrics (*13*). CdS/Cu_2O nanowire photovoltaics to convert sunlight into electricity at higher efficiencies than bulk materials (*14*). Silicon-nanowire-based anodes for lithium-ion batteries may lead to improved energy densities without significant degradation of capacity with usage (*15*). Because charge transfer processes occur across interfaces and surfaces, essentially all devices used for energy collection and storage stand to benefit from nanostructured materials design.

1.3. Nanophotonics

The semiconductors industry has made phenomenal process over the last 50 years by decreasing the size of transistors and increasing computer power according to Moore's Law. While there are many potential difficulties with decreasing the fabrication process to 14 nm and below, the limited bandwidth of metal-based interconnects to transmit data within the processor is expected to be a major limitation. While the telecommunications industry relies on laser light transmitted over fiber optics to pass data at rates greater than 100 gigabits per second, the device size and optical materials are poorly matched to silicon microelectronics (*16*). Near IR wavelengths are best transmitted in SiO_2 optical fibers, but the diffraction limit ($\sim\lambda/2$) restricts near IR optical devices to roughly 0.5 μm. Due to silicon's indirect band gap, III-V semiconductors in the InGaAsP alloy family are typically used in photonic devices, but these materials typically have poor epitaxy with silicon. Any practical photonics solution for microelectronics-scale interconnects would require emitters, waveguides, and detectors on the nanoscale, that is be integrated with the silicon fabrication and electronics.

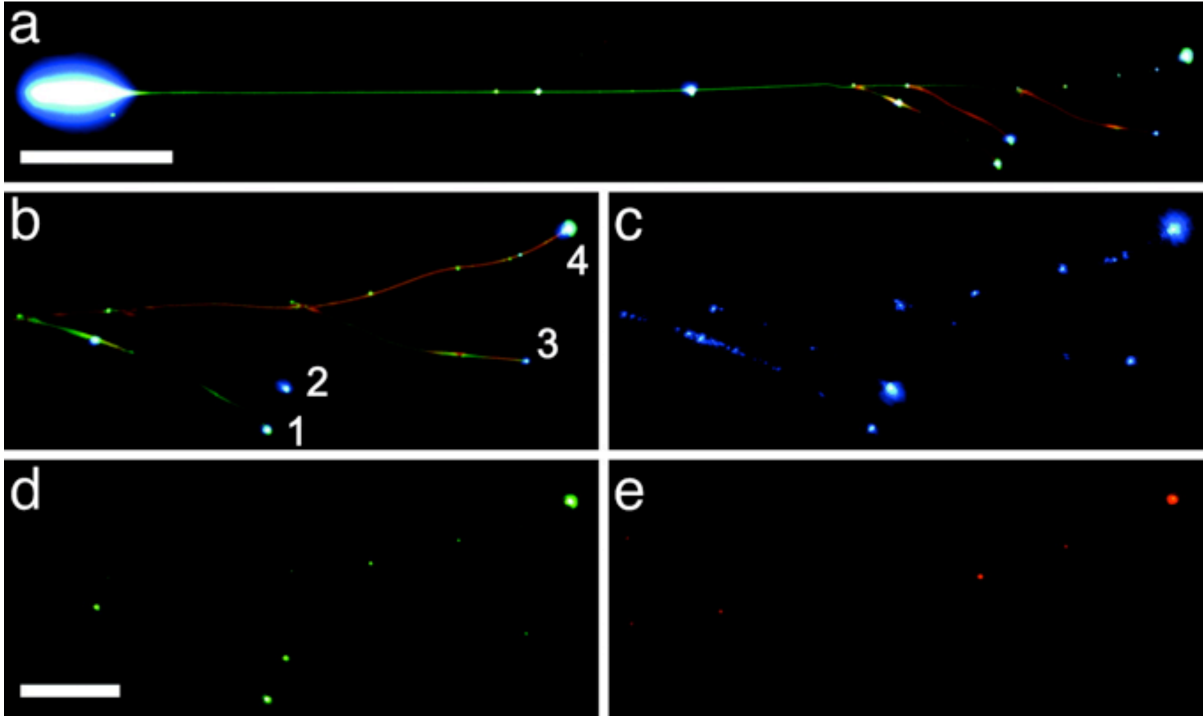

Figure 1.3: Nanowire waveguides and color filtering. **a**) Dark-field image of a four-ribbon assembly as it guides white PL generated at the pump spot (left) and separates it into a different color at the end of each ribbon (right). (Scale bar: 50 μm.) **b**) Magnified view of the emission region. The branch ribbons 1–3 emit green, aqua, and blue light because of their progressively smaller cross sections (350 x 140 nm, 260 x 175 nm, and 210 x 135 nm, respectively). Their 50% cutoff wavelengths were determined by near-field scanning optical microscopy to be 543, 502, and 478 nm. The stem ribbon is 260 nm x 240 nm x 390 μm. **c**) Nonresonant blue light is transmitted to the end of all four ribbons, whereas (**d**) green light is much more strongly guided by ribbon 1 than by ribbon 3 and (**e**) red light is filtered out by all three branches. (Scale bar for **b–e**: 20 μm). This image was adapted from reference (*17*).

Semiconductor nanostructured materials have several features that are well-suited to photonic devices and developing new techniques for incorporating photonics on silicon micro-electronics (*18, 19*). Quantum well heterojunction structures have long been used in LEDs and lasers to force carriers into a confined region to improve the recombination probability. While channel waveguides etched into silicon have been demonstrated (*20*), semiconductor nanowires have several features that are well-suited to wave-guiding light, including dimensionality and size control, diverse optical and electronic properties, low surface roughness (*10*), and the ability to operate above or below the diffraction limit. Practical light emission from silicon is unlikely given its indirect band gap, although silicon Raman lasers have been demonstrated (*21, 22*). The challenges include room-temperature lasing cavities smaller than the wavelength of light (sub-λ), electrically-pumped devices, and integration of III-V or II-VI materials with silicon.

Akin to an optical fiber, tin oxide nanowires have been shown to be effective waveguides for visible light through total internal reflection, given its index of refraction (n = 2.1) and high transmission of visible wavelengths (E_g = 3.6 eV) (*10*), as demonstrated in Figure 1.3. Light can be introduced to the cavity by scattering from a white light source focused at the end of the nanowire, through laser excitation to produce visible defect PL emission, coupling in an etched silica optical fiber (*23*), or even through coupling in a (optically-pumped) nanowire light source

(*10*). The transmission characteristics are dependent on the nanowire dimensions and long wavelength light is more easily scattered, allowing the nanowire to also act as a tunable short-pass filter (*10*). And much like an macroscale linear cavity resonator, the ends of the nanowire act as mirrors and resonant frequencies can be observed in shorter nanowires according to Fabry-Pérot (FP) resonance equation:

$$\Delta\lambda = \frac{\lambda^2}{2L\left(n - \lambda\left(\frac{dn}{d\lambda}\right)\right)}, \tag{1}$$

where $\Delta\lambda$ is the mode spacing and L is the cavity length. Finally, because the nanowires are smaller than the wavelength of light, some amount of the electric field intensity exists outside the nanowire, which can be used to excite dye droplets on the nanowire (*17*), to excite silver nanoparticles for surface enhanced raman scattering (SERS) measurements (*24*), or for sensing with pH-sensitive dyes (*23*). With a nanowire grown from a nonlinear material, such as $KNbO_3$, it is also possible to observe frequency upconversion in single nanowires (*25*).

Soon after the discovery of the optically-pumped ruby laser in 1960, an electrically-pumped GaAs semiconductor diode laser was demonstrated in 1962 (*26*). As in atomic laser systems, the primary requirements of semiconductor laser operation are (a) a population inversion of carriers in the CB and VB to provide optical gain, (b) a laser cavity resonant with the emission wavelength that passes through the gain material, and (c) that the optical gain is much larger than the cavity and device losses. The lasing threshold is defined as the optical or electrical energy necessary to overcome the losses. The successful operation of a laser is marked by (a) a superlinear increase of emission energy with increasing pump power beyond lasing threshold, (b) a narrowing of the emission band, and (c) the emission of coherent light. While the initial demonstration of GaAs was a simple homojunction that required cryogenic cooling to operate, semiconductor lasers quickly advanced with improved fabrication techniques to improve the confinement of carriers, such as double heterostructure and multiple quantum well diodes.

By taking advantage of the inherent Fabry-Pérot cavity of the nanowire geometry, optically- and electrically-pumped nanowire lasers have been demonstrated (*9, 27*). However, these nanowires have lengths of several microns, which leads to a Fabry-Pérot mode spacing that supports several lasing modes. The target requirements for a nanophotonic laser source is single-mode room-temperature operation from a silicon-integrated, electrically-pumped cavity smaller than the emission wavelength. While room-temperature sub-wavelength (sub-λ) lasing has been demonstrated (*28*), there are no known reports of all conditions simultaneously.

Surface plasmons, the coherent electron oscillations attributed to shininess in metals, has been linked to several extraordinary phenomena in light and metal materials (*29-34*). A silver film deposited on an InGaN quantum well (with GaN dielectric spacer layer) was shown to improve band edge emission by 14 times when optically excited due to the coincidence of the silver surface plasmon resonnance with the InGaN emission energy (*35*). By increasing the emission efficiency with metal coatings, it is hoped that sufficient gain for lasing can be more easily accomplished in sub-λ cavities with lower quality factors. This has led to integration of plasmonics with photonics through metal-insulator-metal lasing cavities (*36, 37*) and optical antennas (*38, 39*), as well as the development of the surface plasmon laser (or spaser) (*40-42*).

1.4. Thermoelectric generators

The worldwide consumption of energy for electricity generation and transportation produces vast amounts of low-quality waste heat that cannot be captured efficiently and economically by turbine generators. Thermoelectric devices are solid-state systems that can directly convert heat to electricity or induce cooling by flowing a current. These devices are robust and long lasting without maintenance due to the lack of moving parts and thus of interest in the electricity generation, industrial, and transportation industries as a means of increasing fossil fuel efficiency and reducing carbon emissions (*43-45*). However, these devices have historically been too inefficient and expensive (and fossil fuels too inexpensive) to use thermoelectric generators for electricity generation except for in niche applications such as in deep space probes.

Efficient thermoelectric behavior relies on low thermal conductivity to maintain a temperature gradient, but high electrical conductivity to maximize current. The efficiency of a thermoelectric material is related to the material-dependent figure of merit, zT,

$$zT = \frac{S^2 \sigma T}{k} \qquad (2)$$

where S, σ, T, and k represent the Seebeck coefficient, electrical conductivity, absolute temperature, and thermal conductivity, respectively. Though this has been a topic of scientific study for a number of decades, material engineering directed at maximizing zT has been complicated by several interdependencies of the previously mentioned parameters, limiting the efficiency (*46*). Specifically, the Seebeck coefficient's inverse dependence on carrier concentration is at odds with the electrical conductivity's direct dependence. An additional problem is that electrons carry both charge and heat, causing a synchronous increase in the electrical and thermal conductivities with carrier concentration. While commercial viability of thermoelectric devices is predicted at $zT \approx 3$, the interplay of these parameters has limited zT of bulk materials to ~1 at 300 K until recently (*47*).

Theoretical studies pioneered by Hicks and Dresselhaus predict that it is possible to increase zT by using low dimensional materials (*48, 49*). Phonon transport is disrupted by structural features on the order of the mean free path, which is on the order on 50-500 nm in doped semiconductors (*50*). Because the electron mean free path is generally less than 10 nm, charge transport is unaffected. Increased surface-to-volume ratio also increases the effectiveness of surface roughening for boundary scattering (*13, 51*). Additionally, high quality epitaxial films and VLS-grown nanowires are often single-crystalline and have few material defects, leading to enhanced charge transport compared to bulk materials. Quantum confinement can lead to an asymmetric density of states around the Fermi Level, enhancing the power factor ($S^2\sigma$). Other nanostructure-driven phenomena, such as carrier-pocket engineering, energy filtering, and the semimetal-semiconductor transition, may directly modify the Seebeck coefficient of a material without affecting its electrical conductivity (*52*).

In bulk materials, the only way to reduce thermal conductivity independently of electrical conductivity was through the use of high atomic weight materials, such as Bi_2Te_3 alloyed with Sb, Sn, and Pb. However, the zT of such devices remained below 1 from their discovery in the late 1950s until the mid 1990s. As predicted, nanostructured thin-films of Bi_2Te_3 and Sb_2Te_3 where reported to have zT ~ 2.4 at room temperature in 2001 (*53*). In the next year, PbSeTe/

PbTe quantum dot superlattices with a zT ~ 1.3-1.6 at room temperature were used to demonstrate Peltier cooling with a 43.7 K temperature difference across the device (at 299.7 K) (*54*). In 2004, a bulk preparation of $AgPb_{18}SbTe_{20}$ was demonstrated with a zT of 2.2 at 800 K, owing to its inherent disordered nanostructuring, as well as contributions from heavy atomic weight elements (*55*). More recently, thermoelectrics have been proposed for a third potential application: concentrating solar thermal energy with a large inexpensive metal plate and forcing the heat to disipate through thermoelectric generators as an inexpensive alternative to low-efficiency photovoltaics devices (*56*).

1.5. Photoelectrochemistry and solar fuels

Sunlight is an abundant source of clean, renewable power that supplies 36,000 terawatts of power to the earth's surface on (24-hour) average, far more than the 50 TW world consumption predicted by the late 21st century. Unfortunately, while chemical bonds can easily store 30 MJ of energy per kilogram of fuel, a square meter of the earth's surface might only receive that much solar energy over the course of an entire day. Combined with the effects of clouds, precipitation, seasons, and the earth's diurnal rotation, it will not be possible to power our society on photovoltaics alone. Many forms of energy storage have been considered to help smooth and match grid demand with renewable electricity supply, including liquid metal batteries (*57*), pumped hydroelectric, flow batteries, underground compressed air, and flywheels (*58, 59*). Pumped hydroelectric is currently the cheapest and has the best energy capacity among these options, but has poor energy density and requires specific terrain. Given the high specific energy density of chemical bonds, electrochemical production of hydrogen or simple hydrocarbons would allow for indefinite storage of energy that could be released on demand by combustion in large power plans or in on-site fuel cells, used as carbon-neutral fuels for transportation, or even used as feedstocks for the petrochemical industry. However, electrolyzers for producing hydrogen from water are expensive due to the platinum electrodes needed to catalyze the reaction, which isn't even efficient at oxidizing water and requires a large overpotential, reducing efficiency.

Photoelectrochemical (PEC) water photolysis is a potential method of storing solar energy in hydrogen by converting solar energy directly to oxygen and hydrogen using a semiconductor material that must fulfill several requirements. (a) The overall water photolysis reaction requires 1.23 V under standard conditions and is a combination the hydrogen evolution reaction (HER) and oxygen evolution reaction (OER) half-reactions:

$$2H^+ + 2e- \rightarrow H_2 \qquad \text{(HER)}$$

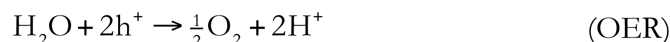

$$H_2O + 2h^+ \rightarrow \tfrac{1}{2}O_2 + 2H^+ \qquad \text{(OER)}$$

For a spontaneous reaction, the semiconductor VB and CB must straddle the HER and OER redox potentials at 0 V and +1.23 V versus NHE, respectively (Figure 1.4). During water photolysis, a photon is first absorbed in the depletion region created by the semiconductor-electrolyte interface (SEI). The electron-hole pair is separated and driven to the surface by the built-in field, from which the electrons and holes are injected into the electrolyte to reduce or oxidize

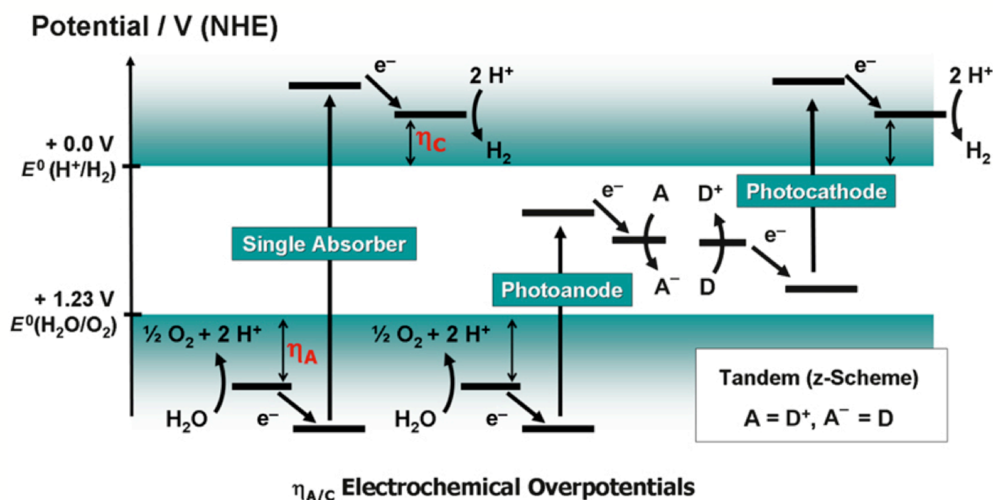

Figure 1.4: Energy schemes for photocatalytic water splitting. In the single absorber case, a single photon must generate electron-hole pairs at suitable potentials to both reduce and oxidize water, with sufficient overpotential to overcome kinetic barriers. A lower bandgap can be used for the photoanode and the photogenerated electrons are extracted with an electrode or chemical oxidant. The photocathode requires an electron source (electrode or reducing agent) to enable photocatalytic water reduction. In the tandem (or z-scheme) configuration, photoanode and photocathode are combined in series to split one molecule of water after absorbing four photons. This requires a directional redox shuttle or an external power source. A, electron acceptor; D, electron donor. This image was adapted from reference (*60*).

water. (b) In order to overcome the kinetic barrier and other energy losses at the SEI, an overpotential voltage is usually required in addition to 1.23 V requirement. While co-catalysts are typically deposited on the surface to reduce the overpotential requirement, these are typically expensive precious metals. While non-previous co-catalysts are a very active research area, an semiconductor with an inherently active surface is preferable. (c) The band gap of a material should be kept as small as possible, 1.5-2.0 eV, to maximize overlap with the solar spectrum. (d) The semiconductor must be stable to corrosion during illumination in aqueous electrolyte solutions, including in strongly acidic or basic conditions. (e) From a commercialization perspective, any viable materials also need to be abundant, inexpensive, and have low toxicity.

While there are several semiconductors with appropriate band positions to undergo water photolysis, there are no known materials that meets all of the parameters (Figure 1.5). Materials such as CdS and GaP appear to have ideal band alignments, but are rapidly degraded during operation (*61, 62*). Anatase TiO_2 and $SrTiO_3$ readily produce hydrogen in water, but have band gaps in the UV region, which only comprises 5% of the solar spectrum (*63, 64*). Rutile TiO_2 was utilized in the very first demonstration of water photolysis, but because the CB lies just below the HER potential, it must rely on non-neutral pH conditions to change the redox potentials, as well as UV light (*65*). Alloys have been prepared to engineer materials with more favorable band gaps for water photolysis, such as TaON (*66*), InGaN (*67*), and $(GaN)_{1-x}(ZnO)_x$ (*68*), however, the quantum efficiency of $(GaN)_{1-x}(ZnO)_x$ is only 5.9%.

Another approach to water photolysis is through the tandem or z-scheme design, which relies on two semiconductors connected in series to supply the necessary voltage (Figure 1.4) (*69*), similar to photosynthesis in plants (*70*). In dividing the photolysis reaction, smaller band gap semiconductors can be used to absorb more of the solar spectrum and each electrode can be

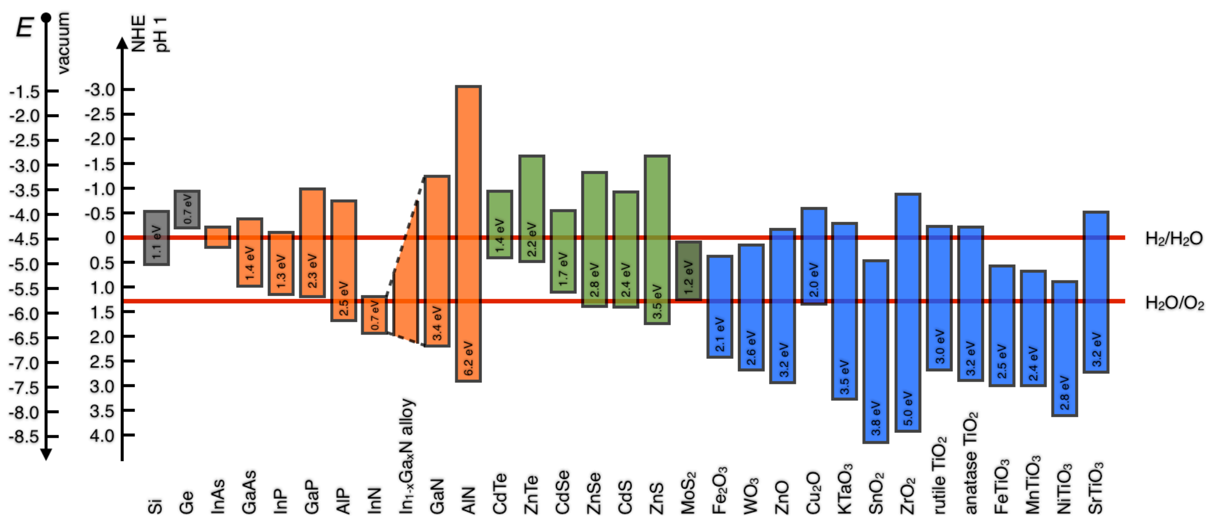

Figure 1.5: Band positions of various semiconductors at pH 1. A plot of the band gap of selected elemental (gray), III-V (orange), II-VI (green), and oxide (blue) semiconductors, relative to the water reduction and oxidation potentials. The valance band maximum and conduction band minimum of each material is indicated by the bottom and top of the colored box, respectively.

specialized for a specific half-reaction. The photoanode and photocathode must be contacted ohmically to transfer photoelectrons from the anode to the cathode, but this can also be accomplished through redox couples in solution if linkage is not possible. The use of electron acceptors and donors as sacrificial reagents allows for the testing of one electrode at a time. There are several possible configurations for electrodes prepared as wafers. The optimal arrangement is back to back with transparent substrates and a transparent conducting material to link the electrodes, so that the higher energy semiconductor transmits lower energy photons to the second electrode (Figure 1.6a). Alternatively, the electrodes can be placed side-by-side with a 1/2 reduction in the areal efficiency, but this allows the use of non-transparent electrodes or two materials of similar band gap. The overall efficiency of a tandem cell can be estimated by overlapping individually measured photocurrent-voltage curves for the photoanode and photocathode materials (Figure 1.6b).

There are several advantages to using nanomaterials with high surface area, especially nanowires, for PEC. Nanowire arrays typically have reduced reflection, relative to materials with smooth surfaces, as well as effective light trapping due to scattering within the array, which improves the probability of absorption (*71*). Ordered periodic arrays and embedded nanoparticle scatterers can further improve the light trapping effect and reduce the effect of incident angle of illumination (*72*). The nanowire geometry also decouples light absorption from charge separation and diffusion processes (*73*). While complete light absorption typically requires 100-200 nm in a direct semiconductor, indirect materials typically require tens of microns. The SEI results in band bending in the semiconductor, providing an electric field to drive minority carriers to the surface to react. Because the minority diffusion length of a semiconductor is $L_D = (D\tau)^{1/2}$, where D is the diffusivity and τ is the lifetime, the active region is equal to the depletion region thickness (W) and minority diffusion length. As many oxide materials suffer from poor minority diffusion length, the nanowire is an ideal geometry to maximize the active region to inactive bulk region without affecting light absorption. Because the open-circuit voltage is decreased by

increasing junction area, it is important that the nanowire diameter is $2(L_D+W)$ to minimize losses and inactive material. Finally, the increased surface area availability leads to decreased overpotential requirements and reduced photocurrent density, allowing for lower activity (and less expensive) co-catalysts to be substituted (*74*).

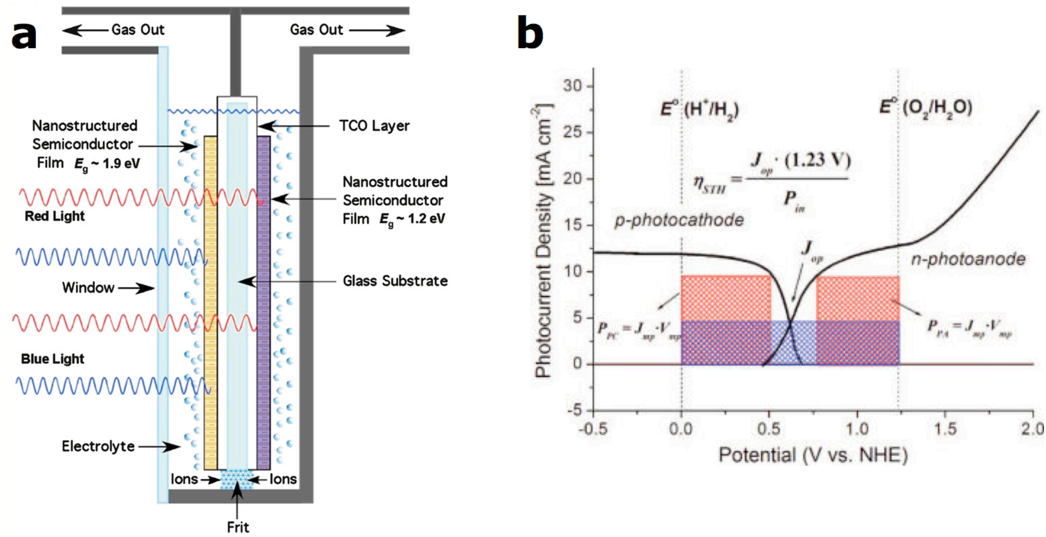

Figure 1.6: Tandem (z-scheme) water photolysis system. a) Illustration of a tandem water photolysis cell. Blue and red light are absorbed by the large bandgap (front) and small bandgap semiconductors (back), respectively. E_g, bandgap energy; TCO, transparent conductive oxide. **b**) Overlaid current density-potential behavior for a p-type photocathode and an n-type photoanode, with overall efficiency projected by the power generated $P_{STH} = J_{op}$ (1.23 V) by the cell for splitting water. These images were adapted from references (*60, 74*).

2. Zinc oxide nanolasers

Since lasing was first observed, there has been a trend toward more stable, compact, efficient laser cavities. Nanolasers with all three dimensions smaller than the wavelength of emitted light (sub-λ) offer many advantages, including low lasing thresholds and power consumption. A practical nanolaser should be a high-gain material at room temperature with a low-loss lasing cavity, electrically pumped, and integrable with silicon microfabrication techniques. Zinc oxide is a suitable material, given its high exciton binding energy and high dielectric constant, for efficient UV lasing at room temperature. In this chapter, we look at the feasibility of sub-λ lasing from ZnO nanostructures, their synthesis, and the possibility of electrically pumped ZnO.

Parts of this chapter were reprinted (adapted) with permission from D. J. Gargas, A. Ni, S.-W. Chang, Z. Zhang, S.-L. Chuang, and P. Yang; Whispering Gallery Mode Lasing from Zinc Oxide Hexagonal Nanodisks, *ACS Nano* **4**, 3270 (2010). Copyright 2010 American Chemical Society.

2.1. Introduction

Zinc oxide is a wide band gap semiconductor (3.37 eV at room temperature) that has become the subject of intense focus owing to its excellent optical properties, abundance, low-toxicity, and the ease of growing high quality materials (*75*). The large exciton binding energy of ZnO (60 meV) leads to enhanced band edge absorption and emission at room temperature and above (*76-78*). Due to formation of native defects (possibly oxygen vacancies), ZnO is inherently n-type, but can be doped with aluminum and group-IIIb elements to further increase the carrier concentration (*79*). Gallium nitride is another semiconductor with a similar band gap as zinc oxide (3.4 eV at room temperature), which has flourished in optoelectronic devices despite higher cost, a more complicated synthesis, and lower exciton binding energy (*80*). This is a direct result of successful p-type doping (GaN:Mg) and UV-to-IR band gap tuning (AlGaInN alloy system), which are both challenges for ZnO (*81, 82*). While many papers on lithium and phosphorous p-doped ZnO have been published, functional homojunction devices remain elusive (*83-85*). Band gap tuning can be accomplished by alloying with CdO or MgO, allowing tunability over a range 4.15–2.65 eV (*75*).

Zinc oxide adopts the hexagonal wurtzite crystal structure in which both oxygen anions and zinc cations adopt a hexagonal close packed lattice with the Zn sublattice shifted by 1/4<001> to form alternating close packed layers in the <001> direction (Figure 2.1). As a result, zinc oxide has a dipole moment along the <001> axis and [001] are polar surfaces consisting of all oxygen or all zinc ions, while all faces parallel to <001> are non-polar faces (*86*). In

order to minimize the higher-energy (001) surfaces, <001> axis is a fast growth direction, leading to elongated crystals with hexagonal cross section to maximize [100] surface area and minimize free energy (*78, 87*). The anisotropy in the <001> axis not only leads to interesting structural properties, but is also the source of piezoelectricity, spontaneous polarization, and nonlinear optical effects (*88, 89*). Wurtzite is the only stable structure for ZnO under ambient conditions, although metalstable zinc blende ZnO has been grown by epitaxial stabilization and the rocksalt is preferred at pressures greater than 9.6 GPa (*90, 91*).

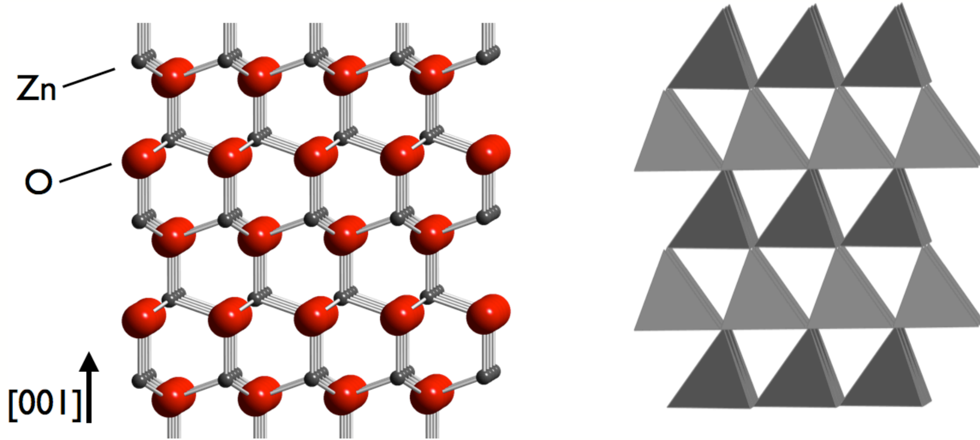

Figure 2.1: ZnO wurtzite crystal structure. Atomic and polyhedra structure models of zinc oxide. Zinc cations and polyhedra are indicated in gray and oxygen anions in red.

2.1.a. Optical properties of zinc oxide

Zinc oxide has been studied extensively as a optical material. It is an efficient absorber of UV light with a room-temperature peak absorbance coefficient, α, of 2 x 10^5 cm^{-1} (absorption length, λ_α = 50 nm) at 3.40 eV, which corresponds to the A exciton (Figure 2.2a) (*92*). The fine structure of it's band edge photoluminescence (PL) emission at low temperature, including phononic and excitonic transitions, are well-understood (Figure 2.2b), but several defect bands in the visible region are still a topic of research (*93*). In particular, the defect band centered around 490-520 nm (2.4-2.5 eV) is commonly observed in ZnO and is typically attributed to oxygen vacancies due to its response to oxygen partial pressure during high-temperature growth or annealing (*92, 94*). However, it has also been attributed to surface defects, zinc vacancies, an oxide antisite defect, and copper impurities, depending on the growth method (*95-98*). The refractive index in ZnO is $n \approx 2.0$ across the visible spectrum and $n_{ZnO} \approx 2.4$ at the band edge (*99, 100*).

While the external quantum efficiency (EQE) of bulk ZnO has long been estimated at 1-3%, recent measurements by Gargas et al. on CVT-grown ZnO nanowires estimate the EQE to be 20% (*101*). Controversially, this same study noted a dependence in the band-edge to defect emission ratio and EQE on excitation power density (Figure 2.3b). At low pump power, the green emission was dominant and the EQE low. At high pump power on vertical nanowire arrays (and presumably thick or bulk samples) where 99% of the excitation power was absorbed,

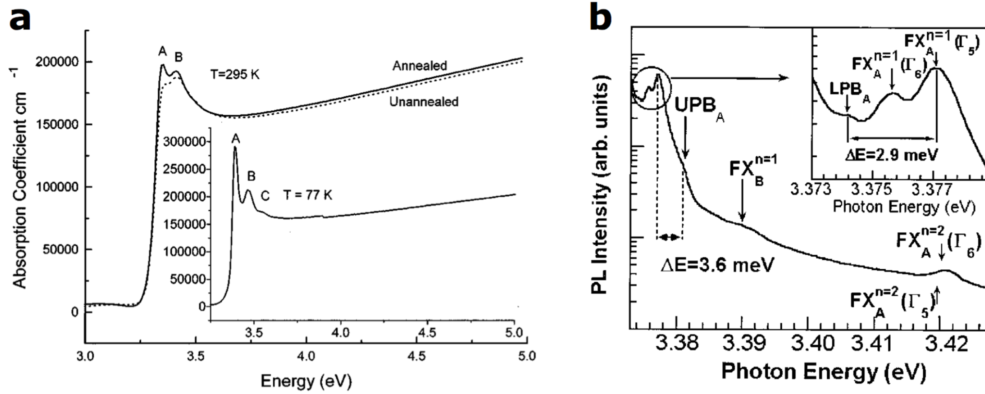

Figure 2.2: Absorbance and photoluminescence in ZnO. **a**) The absorption coefficient as a function of photon energy at room temperature and 77 K in ZnO thin films. **b**) The free exciton fine structure at 10 K of a bulk single crystal of ZnO. These images were adapted from references (*92, 93*).

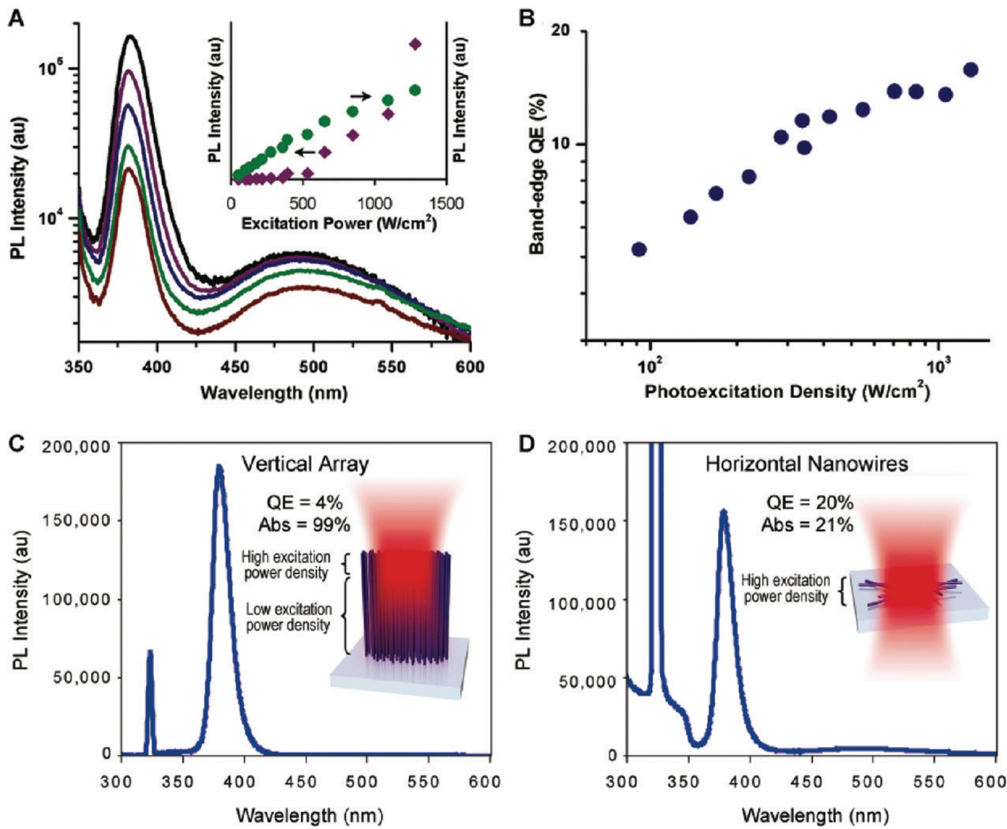

Figure 2.3: EQE of ZnO nanowires depend on the excitation power density. **a**) PL spectra of ZnO nanowires collected at increasing excitation power density shows nonlinear growth of the band-edge peak at 380 nm compared to the defect peak at 500 nm. (log scale) Inset graph shows PL intensity of band-edge peak (purple diamonds) and defect peak (green squares) vs excitation power density. **b**) Band-edge EQE vs excitation power density, I, plotted on a log-log scale. **c-d**) PL spectra and schematics of excitation configurations shown for (**c**) vertical arrays and (**d**) horizontal nanowires. EQE measured from horizontal nanowires is more accurate due to uniform excitation power density while the EQE measured from vertical array is an average of emission from high and low power density excitation. This image was adapted from reference (*101*).

the EQE was 4% (Figure 2.3c). However, at high pump power on thin films of dispersed nanowires with only 21% absorption, the EQE was 20% (Figure 2.3d). It reasons that while the first absorbance length of a thick sample receives high-pump power, excitation powers are low in the rest of the sample and the green emission dominates. The author also suggests a link between oxygen partial pressures, n-type carrier concentration, and the green defect emission (*101*).

2.1.b. Zinc-oxide-based lasers

The earliest report of lasing in zinc oxide was a bulk crystal pumped by an electron beam at low temperature in 1966 (*102, 103*). However, it was not until 1997 that ZnO was first considered to be a practical lasing system after a report of optically pumped lasing at room temperature in a thin film grown by molecular beam epitaxy (MBE) (*104*). Later studies of MBE-grown ZnO nanocrystalline thin films revealed that the laser threshold was minimized in 55-nm grains and increased with decreasing grain size and that lasing was not possible below 30 nm (*105*). The lasing mechanism is mostly attributed to exciton-exciton collisions, although an electron-hole plasma mechanism is observed at high pump powers. ZnO lasing was first observed in nanowire arrays and then cleaved single nanowires in 2001, which unleashed a wave of new research on ZnO nanostructures and nanolasers (*9, 106, 107*). In 2009, lasing from pristine isolated vertical ZnO nanowires grown on sapphire was measured (*108*).

ZnO nanowire-based lasers are based on the same fundamental principles as a larger optically-pumped laser system, except the nanowire serves as both a Fabry-Pérot cavity and the gain medium (Figure 2.4b). The cavity is established by the well-defined (001) crystal faceting in ZnO nanowires and the natural reflectivity of the ZnO-air boundary due to the large difference of refractive indices ($n_{air} \approx 1$) (*9*). The nanowires are optically pumped by a pulsed laser operating at a wavelength sufficient to excite carriers from the valance band into the conduction band and with sufficient excitation power density to create a population inversion. Spontaneous emission from relaxation occurs over a broad range of energies near the band gap, but lasing occurs when a photon resonant with the cavity stimulates emission of coherent photons and the optical gain exceeds the cavity losses. Thus, a laser should display three properties: a narrowing of emission peak width, a superlinear increase in the emission-power plot, and coherent light (*109*).

Based on the Fresnel equations, the ZnO-air boundary is only 18% reflective for a head on relection (0°), for a total cavity efficiency of 3%. In vertical ZnO nanowires, the second boundary with the sapphire substrate is even less reflective ($n_{sapphire} \approx 1.8$) and the cavity is only 1% efficient overall. Despite a high gain of 177 cm^{-1} at 220 kW/cm^2 pump irradiation (*110*), the nanowires must be grown very long to overcome the cavity losses, typically on the order of microns, as in (*108*). While a ZnO nanowire might be considered to be a sub-wavelength laser in two dimensions, the lasing cavity is much larger than its emission wavelength. For the nanowire in Figure 2.4, the Fabry-Pérot mode spacing is calculated to be 1.53 nm. Given that semiconductor PL emission is much broader than atomic transitions (15.9 FWHM in Figure 2.4), several lasing modes are typically observed in a single nanowire. To achieve a single-mode sub-wavelength nanolaser, a different geometry is needed.

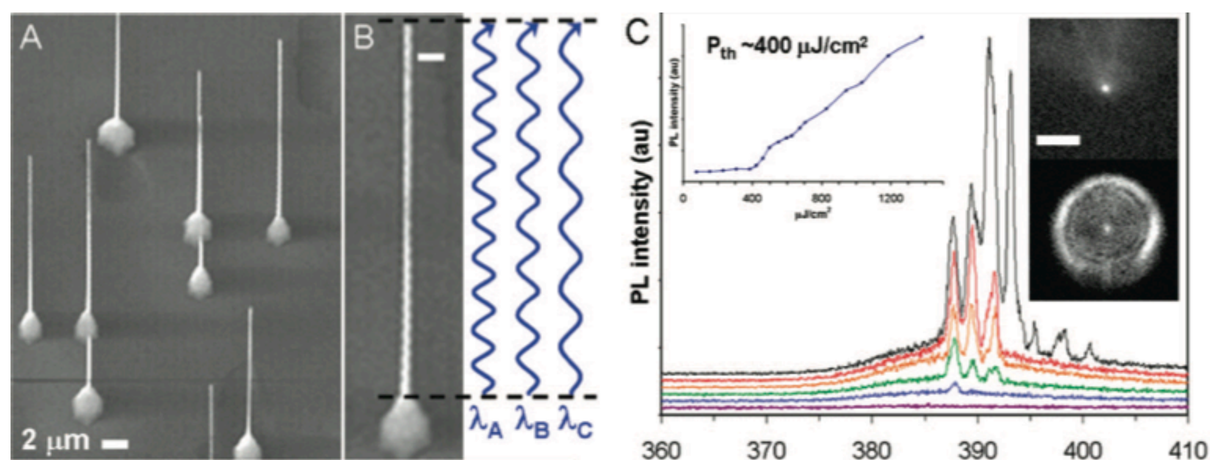

Figure 2.4: Lasing in single ZnO nanowires. (a) SEM image of ZnO vertical nanowire cavities grown on sapphire substrate. (b) SEM image of single vertical nanowire with diagram showing Fabry-Pérot lasing modes as wavelengths λ_A, λ_B, λ_C. Scale bar is 300 nm. (c) Lasing spectra of single ZnO vertical nanowire cavity. Left inset: power dependence graph showing lasing threshold at roughly 400 μJ/cm2. Right inset: dark-field scattering images of a ZnO vertical nanowire cavity from white light illumination (top) and lasing induced by 266 nm pulsed excitation (bottom). Scale bar is 2 μm. This image was adapted from reference (*108*).

Whispering gallery mode (WGM) lasing has been demonstrated in a variety of materials and circular structures (*111-119*). Recent studies have shown ultra-low threshold continuous-wave lasing microdisks (*120*) and visible and near-IR lasing in sub-wavelength diameter structures (*28, 121*). As opposed to Fabry-Pérot modes, which achieve lasing by reflecting off the end facets of a linear cavity, whispering gallery modes undergo total internal reflection around the walls of the disk. WGM lasing has been demonstrated in the hexagonal faceting of ZnO nanostructures (*122-127*). At a reflection angle of 30 degrees, over 96% of the optical mode is reflected at the ZnO-air interface, thus whispering gallery modes provide low-loss, high-efficiency resonant pathways for optical gain. To date, the smallest diameter of the ZnO structures reported in WGM lasing is 650 nm (*123*).

2.1.c. p-Type zinc oxide

While ZnO is readily prepared as an n-type material, p-type doping is difficult and elusive in zinc oxide. A reliable synthesis for high-quality p-type ZnO would make it a far more attractive semiconductor and optical material and a competitor to gallium nitride-based devices (*84, 128-130*). Most ZnO syntheses are unintentionally n-doped due to the formation of native defects and hydrogen impurities (*131-135*). p-Type ZnO is a challenge due to the low solubility of acceptor defects (*136, 137*), the poor selection of shallow acceptors (*138, 139*), the compensating effects of the native defects (*140-142*), and poor stability of p-ZnO (*143*).

Possible acceptor defects include: oxygen vacancies, zinc interstitials, group-I/Ib substitutions for zinc, and group-V substitutions for oxygen. With the exception of lithium, group-I/Ib substitutions are deep acceptors and are not suitable (*137, 144*). However, the small ionic radius of Li drives interstitial formation, which acts as a donor and compensates p-type behavior (*145*). While nitrogen would seem to be ideal dopant given its similar ionic radius and electronic

structure, it is difficult to introduce without compensation from other impurities, such as dinitrogen impurities or hydrogen (from ammonia) (*146*). All other group-V species are predicted to be deep acceptors (*137*), despite numerous published reports of p-type ZnO from phosphorous and arsenic (*147-151*). It is suggested that large ionic radii of these elements leads to complex defects that may act as acceptors (*138, 152*). Unfortunately, many of these reports contain unrealistically high hole concentrations or mobilities, insufficient characterization, poor detail of material quality and long-term stability, and irreproducibility.

Measuring the electrical properties of p-type ZnO is particularly difficult and prone to misinterpretation. Conductivity in ZnO has been shown to be highly dependent on annealing conditions, surface modifications, and even atmospheric composition during the measurement (*153-155*). This has been attributed to Fermi level pinning at surface states, hindering measurements of he conductivity in the underlying material (*156, 157*). Zinc oxide exhibits a strong photoconductivity effect and is shown to have enhanced n-type conductivity under illumination, which can mask p-type behavior (*158, 159*). Hall effect measurements on ZnO thin films are sensitive to contact placement and sample inhomogeneity and can potentially identify the wrong carrier type (*160, 161*). In ZnO nanowires, carrier type and concentration is usually deduced from field-effect transistor (FET) measurements, which are fraught with uncertainty in the low-mobility, low carrier concentration samples expected in p-ZnO (*155, 162*).

2.2. Synthesis of ZnO nanostructures

2.2.a. ZnO nanowires

Zinc oxide nanowires (NWs) are synthesized using a vapor-liquid-solid (VLS)-catalyzed chemical vapor transport (CVT) synthesis (*163*). Equal masses of zinc oxide powder and graphite (1:6.8 mol ZnO:C) are well-mixed by mortar and pestle and packed into a alumina boat, 48 mm x 9 mm. A 3 mm x 5 mm sapphire substrate cleaned by ultrasonication in acetone and coated ~3 nm of sputtered gold is placed directly on the ZnO/C powder near the downstream end of the boat. The boat is loaded into a 50-mm long, 12.75-mm outer diameter quartz tube and placed in the center of a tube furnace with a 1-inch diameter quartz process tube. The carrier gas is 64 sccm of 0.94% O_2/Ar balance and the system is allowed to purge for 10 minutes before reacting. The furnace is ramped to 900 °C as quickly as possible (~14 minutes) and typically held at 900 °C for 8 minutes to prepare 10 μm nanowires. When high-quality, low-defect nanowires are necessary, the cooling rate is limited to 6 °C/min until 700 °C and then passively cooled to room temperature.

While the position of the boat in the tube furnace is not essential (but should be positioned consistently), the position of the substrate on the boat is very important for controlling sample uniformity, quality, and reproducibility. Proper VLS-growth is reliant on a narrow set of conditions and relies on a specific Zn partial pressure for a given oxygen partial pressure. Because the Zn vapor is only produced from the exposed ZnO/C surface and then diffuses over the substrate, the available Zn vapor is linked to the exact substrate position. A further complication is that the oxygen gas can also combust graphite, so the oxygen partial pressure decreases

with distance from the opening of the quartz inner tube. An ideally positioned substrate produces a vertical nanowire array with uniform length from edge to edge. Poorly positioned substrates will have a upstream-downstream length variation, unoriented nanowires, or buffer layer or film growth at the nanowire bases. The substrate position is continually adjusted to optimize for sample uniformity and optical quality according to SEM and EQE characterization.

2.2.b. Procedure for *in situ* doping of ZnO nanowires

Additional precursors can be added to the VLS-catalyzed CVT reaction described for ZnO nanowires for intentional n-type and p-type doping. As CVT growth occurs under near-equilibrium conditions, the final dopant concentration is a factor of the ratio of dopant:Zn partial pressure at the substrate and some lattice incorporation factor. The required dopant concentration may vary widely for different applications: 0.5% Ga for n-type ZnO:Ga nanowires (*164*), 6% Li for p-type ZnO:Li,N nanowires (*165*), or 50% In for InZnO alloy nanowires (Chapter 3). Ideal precursors have similar vapor pressures as ZnO/C at 900 °C so that the precursor can be mixed into ZnO/C (assuming compatibility) and tuned (to a limited extent) by stoichiometric control, thus assuring that the dopant vapor is present at the substrate. Precursors that have much higher vapor pressures at 900 °C, can make use of the natural temperature gradient of the tube furnace and be positioned in a lower temperature region in a second boat, either upstream or downstream of the substrate. Precursors that have much lower vapor pressures than ZnO/C can be positioned in a boat at the furnace center with a higher furnace setpoint with the substrate located downsteam according to the temperature gradient.

p-Type doping of ZnO nanowires has been attempted using several phosphorus and lithium precursors, including Zn_3P_2 (T_m = 420 °C, T_b = 1100 °C), P_2O_5 (T_m = 340 °C, $T_{subl.}$ = 360 °C,), LiOH (T_m = 462 °C, $T_{decomp.}$ = 924 °C), and Li_3N (T_m = 813 °C). P_2O_5 and LiOH are poor candidates for this synthesis, as the low sublimation temperature of P_2O_5 prevents reliable vapor pressure control (as 360 °C is much lower than the reaction temperature) and hydrogen is a suspected n-type dopant in ZnO. Zn_3P_2 was introduced to the reaction both by stoichiometric addition to the ZnO/C precursor and by placement upstream over the 400-600 °C range, as well as by ex situ methods. Li_3N was initially attempted mixed into ZnO/C but found to disrupt all ZnO growth, suggesting that Li_3N vaporizes at much lower temperatures than the reported melting point. Ultimately, Li_3N was placed in a second boat down 9-14 cm downstream of the substrate in 600-800 °C range. Due to the steep temperature gradient at the furnace edge and the volume of the Li_3N precursor, the temperature might vary by 100 °C or more across the length of the boat. Thus, the Li_3N vapor pressure would decrease over the course of the reaction as the precursor is depleted making reproducible results difficult.

2.2.c. Procedure for Au-colloid-grown ZnO nanowires

Growing ZnO nanowires from commercially-prepared gold colloid solutions requires some modification to the typical ZnO nanowire synthesis (Chapter 2). Substrate preparation is very important to minimize foreign material that can lead to nucleation centers for uncatalyzed or self-catalyzed growth directly on sapphire. Best results are acheived by minimizing the time between removing substrates from the sonication bath and beginning the CVT reaction. Because

of this, substrates cannot be prepared in advance or in batches. The ZnO/C boat and quartz tube should be prepared before continuing.

Au colloid solution (BB international/Ted Pella) was diluted with Millipore-filtered deionized water by a factor of 100-1000 to control the nanowire density. This solution can be prepared in batch and stored. Sapphire (11-20) substrates are sonicated in acetone for at least 30 minutes, then dried with a nitrogen blow gun. 4 μL of 1:150 diluted 20 nm Au colloid solution is pippetted onto the sapphire substrate during drying. "Coffee ring" drying patterns are reduced by using the pippette tip to agitate the surface. Once dry, the substrate is loaded into the plasma etcher and cleaned with oxygen plasma for 2 minutes on high (18 W) at 200-300 mTorr. The plasma etcher chamber should be kept pumped down between uses for faster evacuation.

The growth rate of colloid-grown ZnO nanowires is much faster than sputtered-film-grown nanowires under the same conditions due to increased Zn vapor availability per growth site. To prepare 10 μm-long nanowires, the substrates are reacted at 900 °C for 8 minutes with a flowrate of 10 sccm 0.94% O_2/Ar balance, which promotes slower growth. Under the same conditions, 10 μm-long nanowire arrays from sputtered-films require 30 minutes or more.

2.2.d. Patterned substrates for VLS ZnO nanowires

The substrate fabrication is complicated due to the following requirements: epitaxial vertical growth from sapphire (11-20), the need for a VLS catalyst, and a thermally-stable mask to prevent both metal droplet diffusion and uncatalyzed (or self-catalyzed) ZnO growth directly on the substrate (Figure 2.5). Cleaned sapphire substrates were coated with films of SiO_2 and 400-nm poly(methyl methacrylate) (PMMA). A nanoimprint master for a square lattice with 250 nm posts and 500 nm pitch was used to imprint the PMMA layer. Dry etching is necessary to remove the remaining polymer at the bottom of each imprint, but a Cr layer is first deposited by angled-substrate electron beam evaporation to protect the unimprinted PMMA surface. The substrates are then etched in hydrofluoric acid vapor to transfer the pattern into the silica layer. To deposit the VLS catalyst, Au was deposited by electron beam evaporation (source normal to sample), which deposits some Au in the etch pits directly on sapphire. The remaining PMMA was dissolved in acetone, removing the metal layers and leaving behind the patterned silica with Au deposits. ZnO nanowires were grown using a typical CVT synthesis with normal or slightly shortened reaction times.

Nanoimprinted substrates were prepared using 66-, 100-, and 200-nm thick silica layers and Au thicknesses of 5-100 nm. In order to produce a single nanowire from the 250-nm pit, it was expected that a large amount of gold was required to produce a single catalyst droplet with a diameter equal to the pit. Due to the large amount of Au, it followed that a deep pit would be needed to contain the large amount of gold. However, the best results were obtained from 66- and 100-nm thick silica layers with 5-15 nm Au coatings (Figure 2.6a-c). Thicker silica layers tended to result in multiple nanowires growing from single pits (Figure 2.6d). Nanowire arrays grown from a 50-nm thick Au film resulted in kinked nanowires and other poorly defined nanostructures (Figure 2.6e).

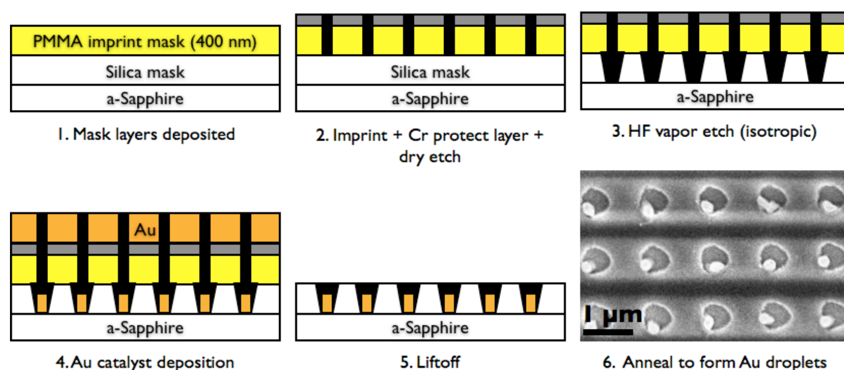

Figure 2.5: Patterning with nanoimprint lithograpy. Schematic illustration of the lithography procedure (**1-5**) and an SEM image of the finished substrate (**6**) showing the patterned holes and Au droplet. The horizontal stripes are charging due to the insulating silica and sapphire layers.

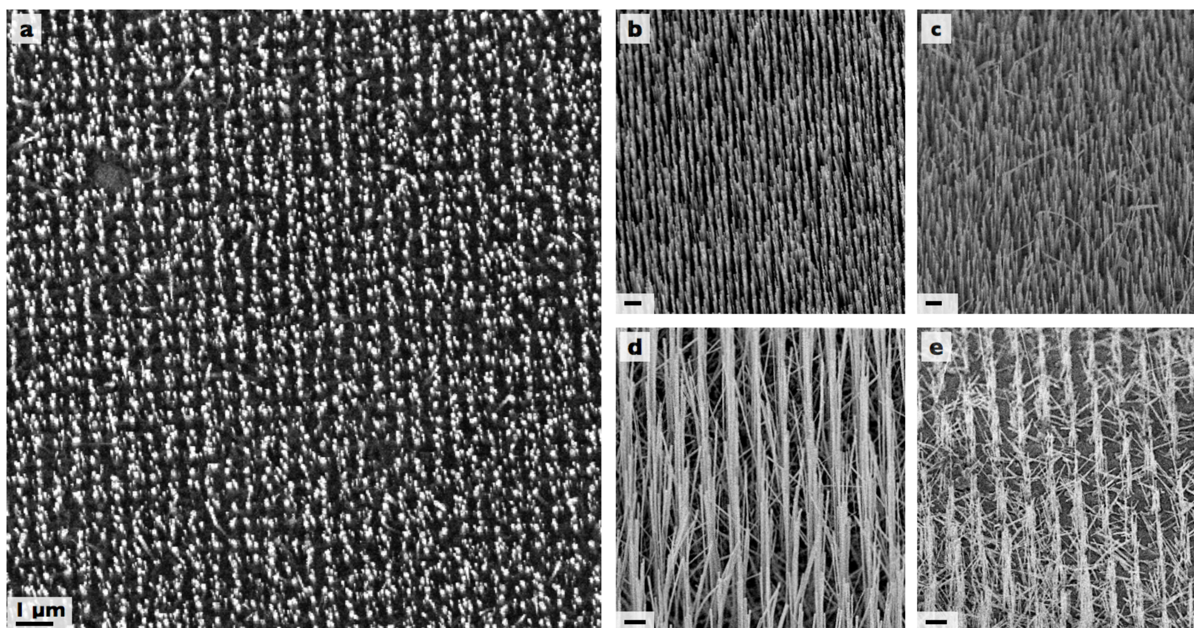

Figure 2.6: ZnO nanowire patterning. a-b) Top-down (**a**) and 45° (**b**) SEM images of ZnO nanowires on 66-nm SiO_2 mask with 15 nm Au. **c-d**) 45° SEM images of ZnO nanowires grown with 15 nm Au on 100-nm (**c**) and 200-nm (**d**) SiO_2 mask. **e**) 45° SEM image of ZnO nanowires grown with 50 nm Au on 200-nm SiO_2 mask.

2.2.e. ZnO pillars and nanodisks

The ZnO pillar and nanodisk syntheses require much higher zinc vapor pressures than ZnO nanowire growth and thus relies on the direct vaporization of Zn powder rather than the carbothermal reduction of ZnO. The procedure is similar to previously reported methods for preparing ZnO tetrapods and "nanocombs," or dendritic nanowire structures (*166, 167*). A wide range of ZnO morphologies can be grown from the same basic reaction by varying the oxygen concentration in the carrier gas. For a given Zn vapor pressure (controlled by precursor temper-

ature), nanowires may be prepared at low oxygen concentrations (~0.1%), straight-walled tetrapods at moderate oxygen concentration (0.5–5%), and a mixture of reverse-tapered tetrapods and nanocombs were formed at high oxygen concentration (5–10%) (Figure 2.7b-e). On a 3 mm x 5 mm substrate, a mixture of structures might form based on the local vapor pressures.

An alumina boat is filled with a small amount of Zn powder (~1 g spread out for pillars and as little as 50 mg in a compact pile for nanodisks) and placed in the center of a tube furnace with a 1-inch quartz process tube (Figure 2.7a). A clean 600-nm thermal oxide/silicon substrate is placed 4-10 cm downstream of the Zn source. The carrier gas is 12 sccm of 0.5% O_2/Ar balance and the system is allowed to purge for 10 minutes before reacting. The furnace is ramped to 800 °C as quickly as possible (~12 minutes). For pillars, the furnace may remain for this temperature for 15–30 minutes. For large nanodisks (~1 μm diameter), the reaction times ranged from 5–10 minutes. For ~600 nm diameter nanodisks, the furnace was turned off once the furnace finished ramping to 800 °C and opened to quench growth. In order to achieve nanodisks smaller than 400 nm, the furnace was ramped to ~700 °C in 10 minutes and then quenched.

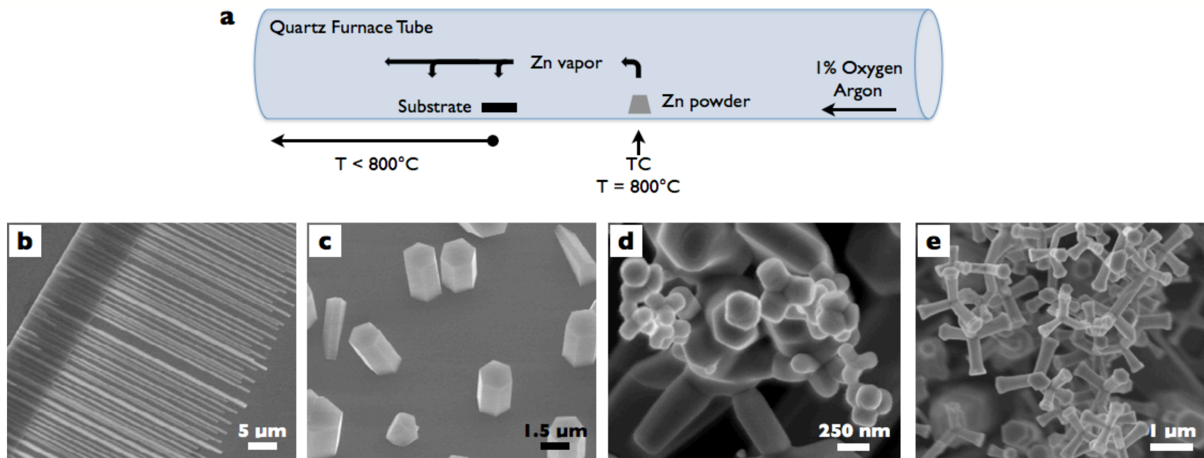

Figure 2.7: Zinc vaporization synthesis and products. a) A schematic of the reaction setup at the center of the tube furnace. TC, thermocouple. **b-e**) SEM images of some of the resulting products from low (b) to high (e) oxygen concentration: dendritic nanowires (b), nanopillars (c), tetrapods (d), reverse-tapered tetrapods (e).

2.3. Lasing of ZnO nanodisks

Although there has been much progress on nanoscale WGM lasers, most reports utilize top-down fabricated materials such as quantum wells or embedded quantum dot layers that require numerous steps for fabrication as well as subsequent patterning. Bottom-up synthesized nanostructures, on the other hand, have inherent advantages over top-down fabricated structures such as high crystallinity, smooth surface faceting, material homogeneity, sample density and high-throughput assembly. Several reports have shown nanowire and nanorod lasers grown on various substrates, in both high-density and dilute arrays (*9, 108, 122, 168, 169*). However, for

WGM structures that require low aspect ratios, there exists significant challenges in realizing bottom-up grown WGM lasers with nanoscale dimensions. An additional challenge concerning WGM structures is that the optical gain in a nanoscale resonator must be sufficiently high to compensate for low optical mode confinement. As the diameter is reduced, the WG mode extends further out of the disk which results in less perfect mode overlap with the gain material. Therefore, to maximize optical gain and minimize non-radiative processes, nanodisks with high crystallinity and low defect density are essential. Finally, spatial isolation is also crucial for optically investigating single nanoscale lasers, which, depending on the method of optical pumping, requires approximately 2-10 μm between nanodisks. Up to this point, reports on bottom-up synthesized nanodisks have not stressed optical isolation for individual optical characterization (*123*).

ZnO nanodisks of varying dimesions were growth on silicon oxide through a CVT process optimized for low density growth with distances approximately 5-10 μm between neighboring disks. Substrates of prepared nanodisks were characterized by SEM to identify potential nanodisks for optical study, based on the size, morphology, and isolation. An illustration depicting the lasing of a whispering gallery mode is shown in Figure 2.8a in which an optical mode internally reflects off the side walls of a hexagonal disk and escapes into the far-field.

Figure 2.8b shows spatially isolated ZnO nanodisks grown on a silica substrate. Low density arrays ideal for individual optical characterization were achieved by optimizing oxygen concentration and reaction temperature during synthesis. Figure 2.8c-h show cross-section scanning electron microscopy (SEM) images of CVT grown ZnO nanodisks with diameters varying from 491 to 815 nm. Diameters were measured from edge to edge. However, as optical simulations will show, the WG mode is in close proximity to the sharp corners, thus hexagonal disks must overcome greater mode loss than those of top-down fabricated circular disks.

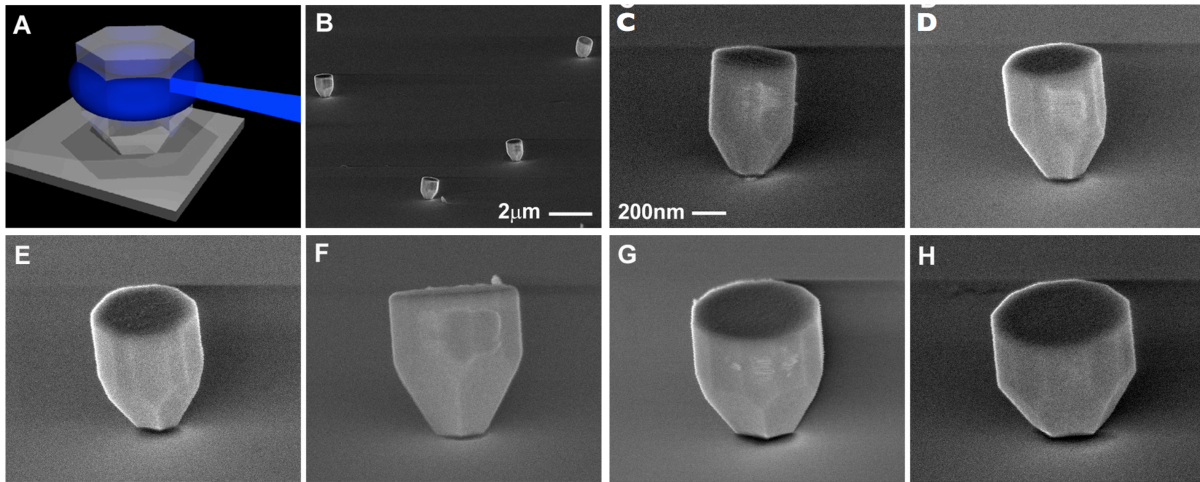

Figure 2.8: Whispering gallery mode lasing in ZnO nanodisks. **a**) Nanodisk illustration showing whispering gallery mode coupling into the plane or vertical direction via surface scattering. **b**) Far-field SEM image of ZnO nanodisks grown by CVT on a SiO_2 substrate. **c-h**) SEM images of various diameter ZnO nanodisks with hexagonal or truncated-hexagonal faceting that supports whispering gallery mode lasing. Disk diameters (measured edge to edge) are 491 nm (**c**), 561 nm (**d**), 612 nm (**e**), 750 nm (**f**), 785 nm (**g**), and 815 nm (**h**).

Interestingly, the base of each ZnO nanodisk is tapered such that the region in contact with the substrate is significantly smaller than the nanodisk diameter. This reduces the area of low-contrast index at the ZnO-silica interface, which normally couples the optical mode into the substrate and hinders the lasing process. Instead, the tapered base provides a high index-contrast barrier and acts as a reflector. In effect, it pushes the optical mode away from the substrate and confines it better to the upper part of the nanodisk. This process optimizes mode overlap with the ZnO gain medium and more efficient lasing is achieved. Unlike top-down fabricated disks, the tapering process for ZnO nanodisks occurs naturally during CVT growth, which eliminates the need for additional steps to isolate the optical mode within the disk, such as back-etching or substrate removal.

Figure 2.9 shows PL spectra from various ZnO nanodisks with different diameters when optically pumped by pulsed laser at room temperature. The large nanodisk in Figure 2.9a has a diameter of 842 nm and a height of 750 nm, and reveals a tapered base approximately 300 nm high. At low pump powers the PL spectrum is broad and featureless (Figure 2.9b bottom curve), however as the pump power is increased above the lasing threshold a lasing peak appears at 391 nm with a full-width-half-maximum (FWHM) linewidth of 0.8 nm. A plot of the integrated peak intensity vs. pump power (Figure 2.9b inset) shows a sharp rise at approximately 500 $\mu J/cm^2$, which indicates the transition from spontaneous to stimulated emission (*170*). Figure 2.9c shows a medium sized nanodisk with a diameter of 612 nm and height of 550 nm, also with a tapered base. Similar to the larger disk, a lasing peak at 389 nm with a FWHM linewidth of 0.7 nm appears as the pump power is increased above the lasing threshold (Figure 2.9d). While one would expect the lasing peak to blue-shift as the disk diameter is reduced, in reality the lasing wavelength is determined by the overlap of the WG mode within the gain medium spectral bandwidth of ZnO (i. e. the peak modal gain), which for most disks occurred between 385-391 nm. As observed in Figure 2.9, a reduction in disk diameter causes the lasing mode to shift into the spectral window of optimal gain at approximately 390 nm.

The power dependence plot for the 612 nm disk (Figure 2.9d inset) shows a slightly larger lasing threshold of 860 $\mu J/cm^2$. The increase in lasing threshold can be attributed to the smaller nanodisk cavity volume. A smaller diameter provides less spatial overlap between the WG mode and the ZnO gain medium, resulting in an optical mode that "spills" out of the external boundary of the nanodisk (*113*). This reduced confinement causes a decrease in quality factor (Q) due to the increase of the leakage power. This effect is even more pronounced in the smaller nanodisk shown in Figure 2.9e which has a diameter of 491 nm and a lasing threshold of 1500 $\mu J/cm^2$ (Figure 2.9f inset). The lasing spectra in Figure 2.9f show a slower onset of the lasing peak at 390 nm and a larger FWHM of 1.2 nm, which indicates a more lossy nanodisk cavity and lower quality lasing mode.

A plot of ZnO nanodisk diameter vs. lasing threshold at room temperature is shown in Figure 2.9g. The best-fit line (red curve) is approximately $1/D^2$, which suggests the lasing threshold is dependent on multiple parameters involving nanodisk diameter. Previous studies show both WG mode quality factor (Q) and confinement factor (Γ) depend on disk diameter (*112, 171*), and since lasing threshold is inversely proportional to Q and Γ, a $1/D^2$ relationship is expected for disk diameter and lasing threshold. Most importantly, the lasing threshold scales inversely with the power of nanodisk diameter, rather than disk height, which is the evidence of whispering gallery mode lasing rather than Fabry-Pérot lasing in the vertical direction.

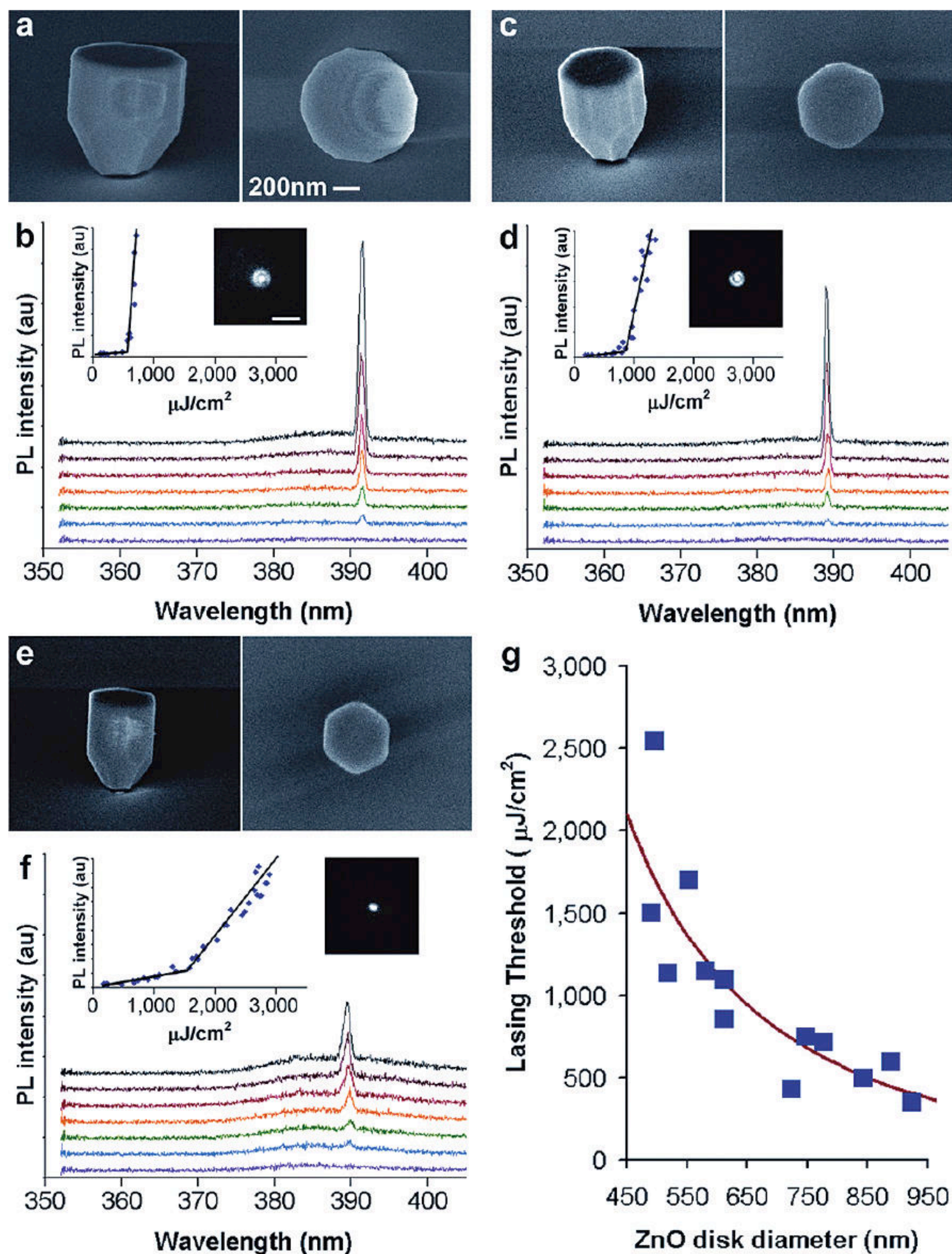

Figure 2.9: Room temperature lasing of ZnO nanodisks with various diameters. Cross-section and top-down SEM images of ZnO nanodisks are shown in (**a**), (**c**), and (**e**) with diameters 842 nm, 612 nm, and 491 nm, respectively. Lasing spectra collected at increasing pump powers are shown in (**b**), (**d**), and (**f**) for corresponding nanodisks in (**a**), (**c**), and (**e**), respectively. Inset graphs show integrated PL intensity vs. pump power, and PL images of nanodisk lasing (scale bar = 10 μm). **g**) Room temperature lasing threshold vs. disk diameter. ZnO nanodisk lasing thresholds (blue squares) are plotted as a function of nanodisk diameter. The curve (red line) is the best fit to a $1/D^2$ trend.

The lasing threshold of ZnO nanodisk lasers (Figure 2.9g, Table 2.1) compares favorably to lasing in other ZnO nanostructures, such as single nanowires and pillars (Table 2.2) (*108*). Similar lasing thresholds of 370 and 360 μJ/cm^2 were measured in a 933-nm-diameter nanodisk and 9.5-μm-long nanowire. In calculating the optical path length in these structures, 2.8 μm in the nanodisk ($L_{WGM} = 3D$) and 19 μm in the nanowire ($L_{FP} = 2L$), it is obvious that the WGM cavities are much more efficient than the FP cavities. In addition to the poor reflectivity of the FP end facets, less than 25% of the field intensity is confined in a 100-nm nanowire (and gain medium) (*172*), whereas the field intensity is likely >90% confined within a 933-nm nanodisk. Despite the greatly reduced path length, the ZnO nanowire is more efficient in terms of material usage; a 100-nm nanowire has a volume of 0.08 μm^3, while the 933-nm nanodisk has a volume of 0.56 μm^3. ZnO pillars, which range from 5-15 μm long and have diameters of ~1 μm, display very low thresholds compared to ZnO nanodisks and nanowires, likely due to their high mode confinement and the complex resonant modes possible by their large size (Table 2.2).

Table 2.1: Summary of diameter dependence of ZnO nanodisk lasing thresholds at room temperature.

ZnO nanodisks			
Diameter (nm)	Height (nm)	Pathlength (μm)	Lasing Threshold (μJ/cm^2)
933	990	2.8	370
842	750	2.5	500
612	550	1.8	860
491	630	1.5	1500

Table 2.2: Lasing thresholds of ZnO nanowires and pillars. Some ZnO nanowire data was previously reported in reference (*108*).

ZnO nanowires			ZnO pillars	
Height (μm)	Pathlength (μm)	Lasing Threshold (μJ/cm^2)	Height (μm)	Lasing Threshold (μJ/cm^2)
19.0	38.0	350	12.0	140
9.5	19	360	9.9	175
8.1	16.2	400	5.1	200

For ZnO nanodisks with diameters of approximately 1 μm and larger, multiple lasing modes were observed under pulsed excitation. Figure 2.10 shows the PL spectrum of a disk with a diameter of 970 nm that contains multiple lasing modes in the ZnO spectrum. This is due to the size of the disk cavity being large enough to support more than one resonant mode that overlaps with the spectral bandwidth of ZnO. For disks with diameters below 1 μm, the spacing

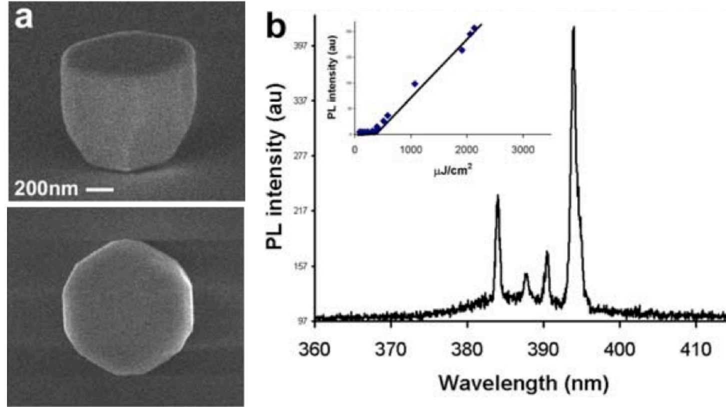

Figure 2.10: Multi-mode lasing in a ZnO disk. a) Cross-section and top-down SEM images of 970-nm-diameter disk. b) PL spectrum showing multiple lasing modes. (Inset: power-dependence plot showing lasing threshold of approximately 350 μJ/cm^2.)

between resonant modes is larger than the bandwidth of ZnO band-edge PL, causing only a single resonant mode to overlap with the PL spectrum (Figure 2.9). At a wavelength of 390 nm and a refractive index of 2.45 for ZnO, the calculated mode spacing, $\Delta\lambda_{WGM}$, is 22 nm for an 842 nm diameter disk for both TE- and TM- modes (*122*). For the smaller diameter nanodisks reported in this paper, the mode spacing is even greater. Ultimately, since the spectral bandwidth of ZnO PL at room temperature is roughly 16 nm, the appearance of two resonant modes in the ZnO PL spectrum is highly unlikely.

Due to the reduction in optical mode confinement with decreasing nanodisk size, at a certain diameter the cavity losses outweigh the optical gain and lasing will not occur. Utilizing our control of nanodisk diameter, we set out to determine the smallest diameter ZnO disk that can achieve lasing. For room temperature lasing this occurs at approximately 490 nm. However, to achieve whispering gallery mode lasing in a sub-wavelength diameter disk, we optically pumped nanodisks at a temperature of 8 K. Low temperature makes the lasing process easier in ZnO nanodisks in two ways: (1) non-radiative processes associated with phonon coupling are significantly reduced, and (2) high intensity excitation can be probed without causing thermal damage to the nanodisks. Figure 2.11 shows two sub-wavelength diameter disks that achieved lasing at 8 K. SEM images of the nanodisks with dimensions (height x diameter) of 791 nm x 375 nm and 606 nm x 283 nm are shown in Figure 2.11a and 2.11d, respectively. The 375 nm diameter disk exhibits a clear lasing peak at approximately 375 nm and a lasing threshold at roughly 250 μJ/cm^2. Similarly, the 283 nm diameter disk shows a lasing peak at approximately 374 nm, however at a much larger threshold of 3000 μJ/cm^2. As discussed above, the increased lasing threshold is due to the reduced diameter, particularly when it is smaller than the free space lasing wavelength. Especially in the case of the 283 nm diameter disk, significant portion of the whispering gallery mode exists outside the nanodisk, which results in much less overlap with the ZnO gain medium.

To quantify the overlap between the whispering gallery mode and the ZnO nanodisk, optical mode simulations were performed by finite difference time domain (FDTD) method (*173*), using a freely available software package with subpixel smoothing for increased accuracy (*174*). FDTD simulations were used instead of a conventional method based on effective optical

path length (ray optics) due to the small diameter of the nanodisks. For larger cavites, one can usually estimate the threshold gain of the fundamental whispering-gallery mode using the effective optical path length around the cavity, which is proportional to the edge length of the polygon (*112, 113*). Specifically, this type of the estimation is based on the analogue of traveling-wave lasers, in which the wave amplitude has to return to itself after the absorption/amplification during the wave propagation and transmission loss occurs whenever the fictitious ray of the lasing mode hits the polygon surface. It should be noted that the validity of this approximation lies in the well-guided modal profile along the growth direction of the polygon cavity and the diameter of the disk is much larger than the resonant wavelength, namely, the radiation loss is dominated by the power leakage at the sidewalls, not from the top and bottom of the polygon. However, with the decrease of the disk diameter close to the resonant wavelength, more field penetrates into the substrate below or leaks out the disk from the top. From the FDTD calcu-

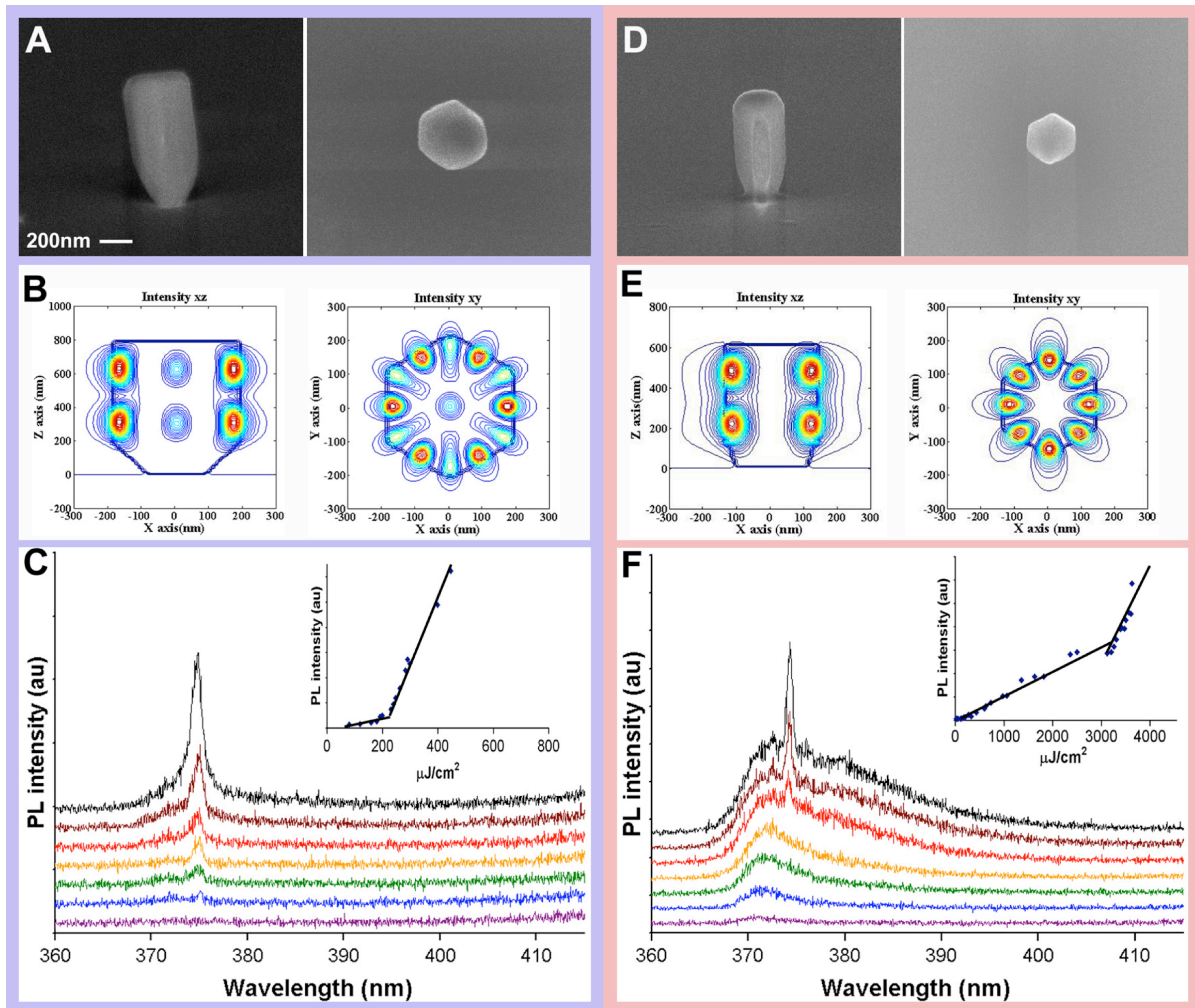

Figure 2.11: Lasing properties of sub-wavelength ZnO nanodisks at 8 K. Cross-section and top-down SEM images showing nanodisks with dimensions (height x diameter) of (**a**) 791 nm x 375 nm and (**d**) 606 nm x 283 nm. Optical mode simulations of the calculated $|E|^2$ field in the xy-plane are shown in (**b**) and (**e**) for nanodisks in (**a**) and (**d**), respectively. Lasing spectra are shown in (**c**) and (**f**) for nanodisks in (**a**) and (**d**), respectively. Inset graphs show integrated PL intensity vs. pump power.

lations, although the main radiation losses indeed come from the sidewalls, those from the top and bottom of the nanodisk are not negligible. Furthermore, the field profile from the FDTD calculation indicates that the possible lasing modes are not fundamental whispering-gallery mode of the polygon cavity. These facts make the estimation of the threshold gain of this 3D polygon cavity from an *effective optical length* impractical.

Instead, the proper way to estimate the threshold gain G_{th} of a possible lasing mode is to use the formula below:

$$G_{th} = \frac{2\pi n_g}{\Gamma_E \lambda Q} \quad (3)$$

where n_g, λ, Γ_E and Q are group index of the material, resonant wavelength, energy confinement factor, and quality factor, respectively. This relation originates from the general gain-loss balance condition of the rate equation and is valid for all types of cavity modes. In our case, the FDTD calculation can give λ, Γ_E and Q. Since in the calculation the material loss is assumed small, the calculated quality factors in the paper are from the radiation losses of the cavity, which include power leakages in *all directions*. Accordingly, G_{th}'s for different structures can be obtained. Detailed derivations of this formula are shown in Ref. (*173*).

Using this method, $|E|^2$-field intensities were calculated for the horizontal and vertical planes of the 375 nm and 283 nm diameter disks and are shown in Figure 2.11b and 2.11e, respectively. The calculated mode wavelengths for the 375 nm and 283 nm diameter disks are 376 nm and 374 nm, respectively, which agree well with the experimentally observed lasing peaks. For the 283 nm diameter disk, the optical energy confinement factors (*175*) of the polarization components parallel ($\Gamma_{||}$) and normal ($\Gamma_{\perp}$) to the silica substrate are 0.105 and 0.541, respectively, and the quality factor (Q) is 93. Despite having a diameter much less than the wavelength of the lasing mode, the 283 nm disk managed to contain almost 65% of the mode energy within its structure. This is in part due to the tapered base that pushes the mode away from the substrate into the upper part of the nanodisk.

To quantitatively compare the advantages of a tapered-base cavity, the energy confinement factor and Q were also calculated for a 283 nm diameter cavity with vertical sidewalls. A comparison of the nanodisk mode patterns with and without a tapered base is shown in Figure 2.12. In the non-tapered structure, the optical energy confinement factors, $\Gamma_{||}$ and $\Gamma_{\perp}$, of the nanodisk are 0.092 and 0.521, respectively, and Q is only 77. Consequently, more field penetrates into the substrate, which indicates that the tapered base geometry confines the mode in the nanodisk better. This results in the smaller leakage power from the substrate. For a nanodisk with a tapered base, the quality factor is improved by 20.7%, and the corresponding threshold material gain can be decreased from 10,889 cm^{-1} to 7351 cm^{-1}.

To further investigate the effect of the tapered-based structure on the leakage power, we calculate the ratio of the leakage power from the substrate over the total leakage power and compare these values for tapered-based and vertical-sidewall structures. The leakage power is calculated by simulating an artificial box that encompasses the nanodisk as well as a portion of the substrate underneath. The Poynting vectors are then determined by the FDTD program, which yields the corresponding radiation powers from the six facets of the box at any moment. To obtain the radiation powers of a specific resonant mode, the mode is excited using a dipole

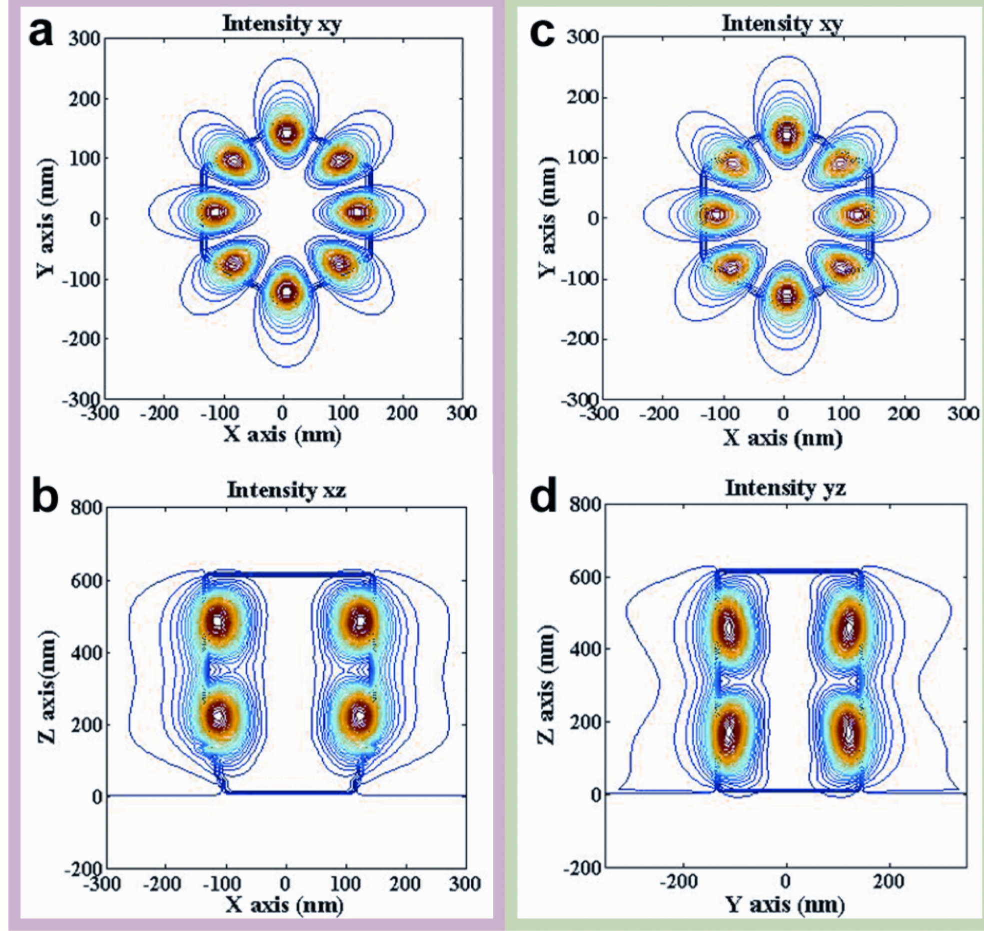

Figure 2.12: WGM simulations of a sub-wavelength ZnO nanodisk. Calculated $|E|^2$ field of the nanodisk with dimensions 283 nm × 606 nm (diameter × height) in the (**a**) xy-plane and (**b**) yz-plane. The calculated mode has a resonant wavelength of 374 nm and a quality factor of 93. The simulations shown in (**c**) and (**d**) are for the same nanodisk without the tapered base. This mode has similar field patterns in the xy and yz planes to those in (**a**) and (**b**) except for the field above the substrate surface. Its wavelength and Q are 378 nm and 77, respectively. Comparing (**b**) and (**d**), the tapered-base nanodisk has less field penetrating into the substrate, leading to a higher quality factor.

source with a narrow bandwidth. After the source is turned off the radiation powers from all six facets are calculated in time. To obtain the averaged radiation power, the radiation powers are summed over several optical cycles and divided by the total optical cycles.

This method is used to calculate the leakage powers from the top (P_{air}), sidewalls (P_{xy}) and bottom (P_{sub}) of the simulated box, respectively, for the structures with and without tapered-bases. The ratios for each component over the total leakage power, the sum of P_{air}, P_{xy} and P_{sub}, for both cases are tabulated in Table 2.3. The ratios of P_{sub} over the total leakage power for tapered-based and vertical-sidewalls cases are 0.172 and 0.186, respectively. The calculation shows that the radiation power from the substrate can be reduced by 7.5% using the tapered base. Although the energy confinement factors Γ_E in the nanodisk for these two cases are only 3% different, the confinement factors in the substrate are 0.168 in the tapered-based case and 0.213 in the vertical-sidewall case. This indeed shows that more energy leaks into the substrate for the vertical-sidewall case.

By combining a low-loss lasing mechanism into a high-gain semiconductor material, ZnO nanodisks have achieved lasing in the smallest diameter WGM structures to date. The observed lasing in 491 nm diameter and 283 nm diameter disks at room temperature and low T (8 K), respectively, represent the smallest diameter semiconductor structures for both chemically synthesized and top-down fabricated WGM structures. Furthermore, when normalized to the refractive index at the lasing wavelength (ZnO = 2.45, GaAs = 3.5, InP = 3.5), ZnO nanodisks exhibit the lowest ratio of diameter-to-lasing wavelength that were previously demonstrated with InGaAs and InP WGM disks at near-IR wavelengths (*28, 121*).

Table 2.3: Leakage Power Ratio.

	leak power ratio		
	sidewall	air	substrate
Tapered-based	0.738	0.09	0.172
Vertical sidewalls	0.723	0.091	0.186

2.4. Metal-enhanced photoluminescence

Surface plasmons, electron oscillations on the surface of metals that are excited by light, are known to enhance light absorption and Raman scattering. It is believed that the discontinuous metal coating on a semiconductor with a thin dielectric spacer layer somehow increases the internal quantum efficiency of the emitter, which is dependent on the ratio of the radiative recombination rate to the total recombination rate. The enhancement cannot be due to light absorption enhancement, which occurs when the metal is placed as an antenna and increases the surface area over which light can be absorbed– in this case, the metal coats the semiconductor and leads to a decrease in photons that can be absorbed. Instead, it is thought that the intense local electric field at the metal surface increases both the radiative and nonradiative decay rates, although the radiative rate more so. However, this only accounts for part of a small part of the enhancement- by decreasing the exciton lifetime, carriers are more quickly returned to the ground state to be reexcited.

To take advantage of this effect, a conformal Al_2O_3 layer was deposited on the surfaces of a ZnO nanowire vertical array using atomic layer deposition (ALD). The alumina coating was optimized at 6 nm in ZnO, similar to the values reported in the literature. With a thinner or absent spacer layer, carriers are injected into the metal and lost through nonradiative processes, quenching the emission. The ALD deposition and alumina layer did not affect PL emission by more than ±15% (Figure 2.13), which was recorded from the same exact location. A discountinuous ~1 nm film of gold was sputtered onto the ZnO/Al_2O_3 NW arrays. The PL emission from the laser spot on the $ZnO/Al_2O_3/Au$ arrays was visibly brighter (Figure 2.13f). A plot of the enhancement factor (EF = final PL/initial PL) versus wavelength reveals a peak of 34-times enhancement at the band edge, while the defect emission was slightly reduced (Figure 2.13a). The features around the band edge the EF peak suggest that the radiative rate enhancement may

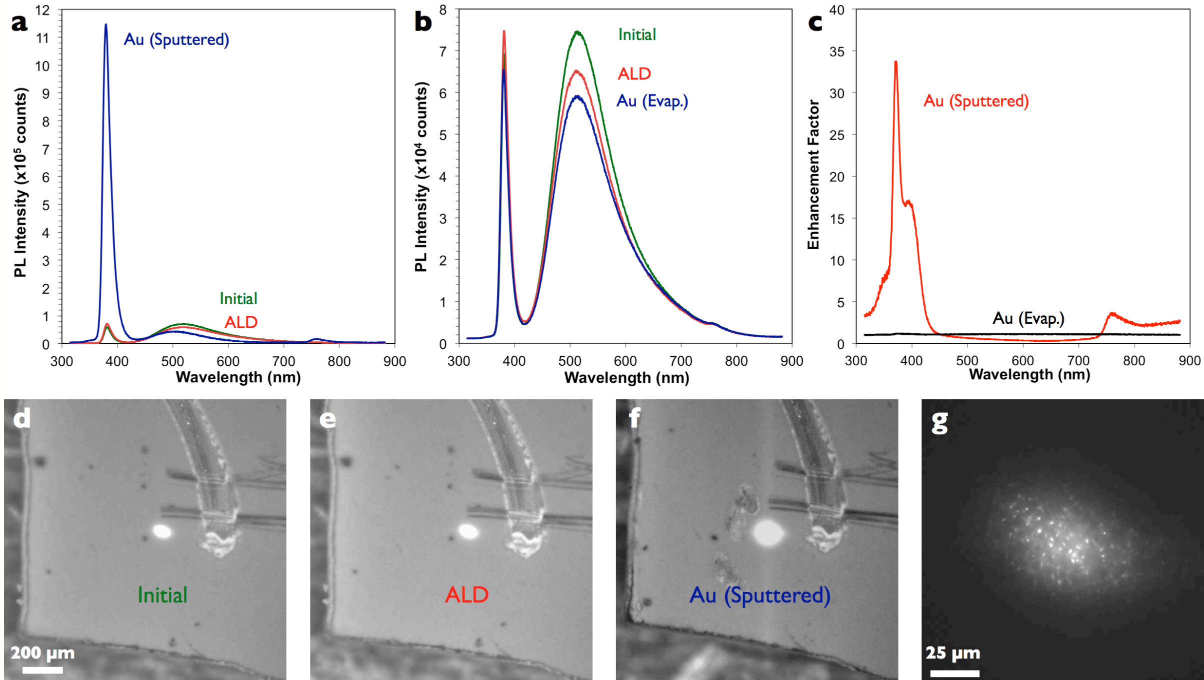

Figure 2.13: Surface-plasmon enhancement of PL emission in ZnO/Al_2O_3/Au. a) Evolution of the PL spectra for the same spot on a ZnO NW array initially (green), after 6 nm Al_2O_3 ALD deposition (red), and 1 nm sputtered Au deposition (blue). **b**) As in panel (**a**), but with an e-beam evaporated Au coating (blue). **c**) The enhancement factor for the samples prepared in panels (**a-b**). **d-f**) White-light illuminated field of view (5x objective) with laser spot for the initial (**d**), after ALD (**e**), and after sputtered Au (**f**), for the series in panel (**a**). The substrate has been intentionally scratched to aid in positioning. **g**) PL emission of vertical ZnO nanowires (50x objective). Note,that the y-axis of (**a**) is $x10^5$ counts and (**b**) is $x10^4$ counts.

depend on the emission mechanism, although features are seen in the EF plot for other materials (Figure 2.13c). The experiment was repeated using an e-beam evaporator-deposited Au film, which resulted in a small decrease in PL emission and a featureless EF plot (Figure 2.13b).

Other metals were tested for enhancement effects in ZnO, including Al and Pd. The ZnO/Al_2O_3/Al array showed the best performance, with a peak enhancement factor of 74 at the band edge and a 10x improvement of the defect (Figure 2.14a). The optimal conditions for PL enhancement was determined to be a 6-nm thick Al_2O_3 layer with a 3-nm sputtered Al discontinuous film. Of the three sputtered metals test, the weakest enhancement was from palladium, which has weak surface plasmon activity (Figure 2.14b). Silver is expected to have enhancement factors intermediate of Al and Au, given its peak surface plasmon resonance relative to the others. Al and Pt were also deposited by e-beam evaporation but did not have any significant increases in PL emission (Figure 2.14b). While sputtering results in a discontinuous, rough film that is typically associated with plasmonic activity, the evaporated films were relatively smooth, uniform, and apparently plasmon-inactive films, which only served to attenuate the pump intensity.

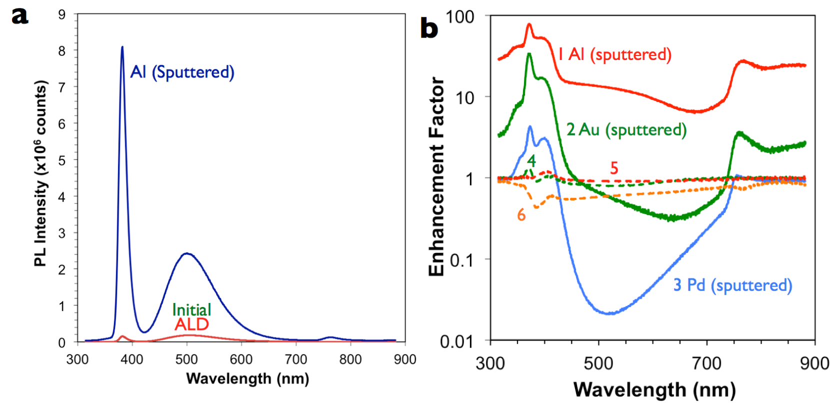

Figure 2.14: PL enhancement of ZnO by Al and other metals a) Evolution of the PL spectra for the same spot on a ZnO NW array initially (green), after 6 nm Al_2O_3 ALD deposition (red), and 3 nm sputtered Al deposition (blue). Note that the y-axis is x10^6 counts. **b**) The enhancement factor for several metal coatings on ZnO/Al_2O_3: sputtered Al (1), sputtered Au (2), sputtered Pd (3), evaporated Au (4), evaporated Al (5), and evaporated Pt (6).

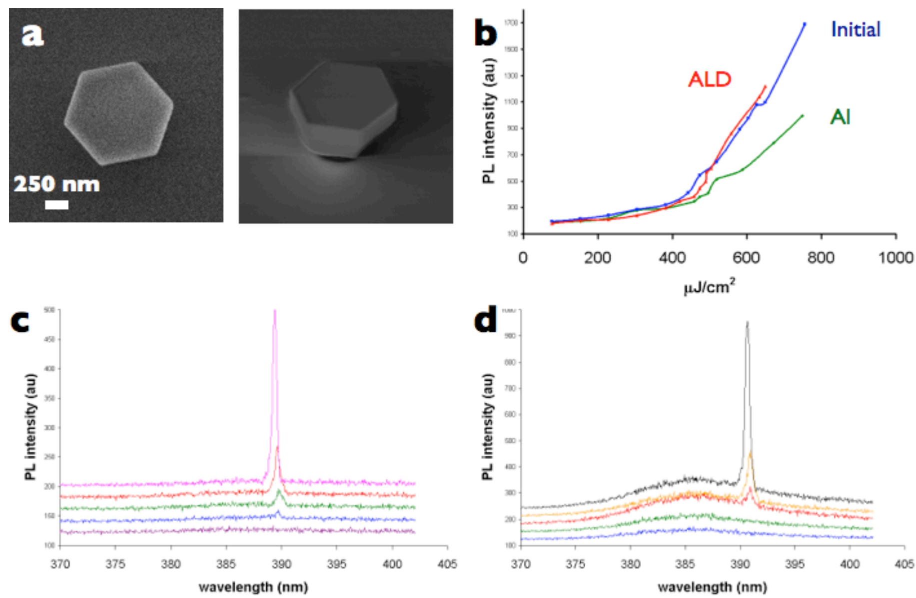

Figure 2.15: PL and lasing emission in Al-coated ZnO nanodisks. a) Cross-section and top-down SEM images of a ZnO nanodisk with diameter of 1050 nm and height of 425 nm. **b**) Integrated PL intensity versus pump power for the uncoated ZnO nanodisk (blue), after 6 nm Al_2O_3 ALD deposition (red), and 3 nm sputtered Al deposition (green). **c-d**) Lasing spectra collected at increasing pump powers for the untreated ZnO nanodisk (**c**) and after Al2O3 ALD and Al depositions (**d**).

Towards the ultimate goal of metal-enhanced laser operation, a similar Al_2O_3/Al treatment was applied to the ZnO nanodisks, with the lasing power series and lasing threshold collected at each step. However, the metal coating did not have a large effect on the spontaneous emission at pump energies below the lasing threshold. In the 1050 nm ZnO nanodisk shown in Figure 2.15, a superlinear increase in emission was observed, but the laser emission was weaker than equivalent pump power in the uncoated nanodisks. The lasing threshold did not appear to

change significantly. In a large number of tested ZnO nanodisks, especially those with decreasing diameter, there was no apparent superlinear increase or lasing threshold observed. Similar tests on ZnO NWs, which has better overlap between the available surface area and mode leakage, revealed similar results. It is reasonable that as the metal coating increases the radiative rate, the radiative lifetime is decreased and it is more difficult to maintain a population inversion for lasing. However, preliminary results suggest that many of these samples display *increased* radiative lifetime, which cannot currently be explained.

2.5. p-Type lithium-doped ZnO nanowires

Lithium-doped ZnO nanowires were grown using Li_3N as a solid dopant precursor. The lithium doping level was varied by adjusting the position of the dopant across the natural temperature gradient of the furnace. ZnO:Li nanowires were characterized using SEM imaging to select for conditions that stunted nanowire growth (indicating the influence of Li vapor), but does not completely halt nanowire growth, and then further optimizing around these conditions. ZnO nanowires were grown with a range of lithium precursor temperatures from 25 °C, which had no effect on the growth, to 770 °C. (Figure 2.16). At the high end of precursor temperature range, the prepared samples were often completely non-conductive. Beyond 770 °C, the nanowire growth conditions were severely perturbed and poor growth and morphology control were observed.

Elemental characterization for lithium is very difficult due to its low atomic number. Lithium (in the ground state) does not have a K_α transition and cannot be measured in energy dispersive x-ray spectrometers. Lithium has a small photoionization cross-section for x-ray photoelectron spectroscopy (XPS) that only allows for detections when concentrations are ~5% and higher. Neither lithium or nitrogen peaks were observed in XPS of Li_3N-doped ZnO (Figure 2.17a). Some previous reports have observed a shift in the x-ray diffraction pattern after lithium incorporation, particularly in the the *a* lattice parameter (*176, 177*). The highly ordered nature of the ZnO nanowire arrays makes observation of the *a* parameter difficult and no consistent shift has been observed (Figure 2.17b). Fortunately, lithium incorporation in the lattice is readily observed in low-temperature PL studies (*176, 177*). At 10 K, the band edge emission of Li_3N-

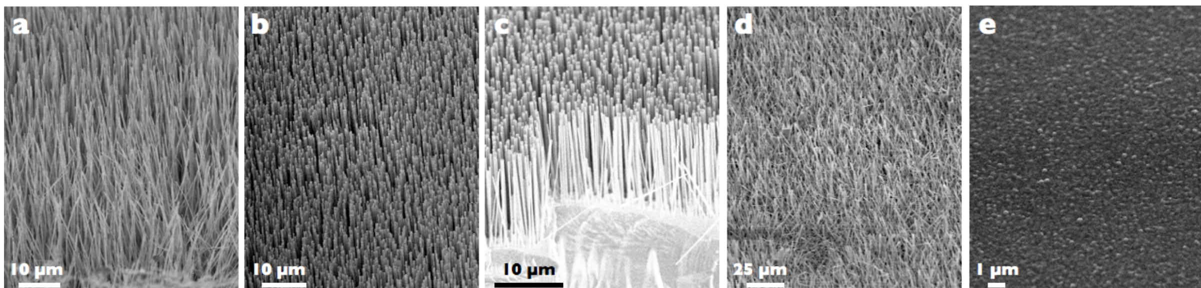

Figure 2.16: SEM images of Li_3N-doped ZnO nanowires. a) ZnO nanowires grown without a lithium precursor. **b-d**) ZnO nanowires grown with Li3N precursor position at 200 °C (**b**), 670 °C (**c**), and 710 °C (**d**). **e**) At high temperature, no nanowire growth is observed.

doped ZnO nanowires is redshifted by 9.6 nm and significantly broadened (FWHM = 1.0 nm in ZnO, 12.5 in ZnO:Li), which is similar to literature reports (Figure 2.17c-d).

The electrical conductivity, carrier concentration, and carrier type of prepared ZnO nanowires were measured by single-nanowire FET devices. Electrical devices were made by either drop-casting or micro-manipulating nanowires onto a Si chip with 200 nm of thermal oxide on the surface. The nanowires were top-contacted in one of two methods: (a) four-point probe using metallic contacts defined by standard photolithography techniques or (b) two-point probe using a TEM grid as a mask for an electron-beam evaporated metal film without any wet chemistry. Although the four-point method is a superior method that allows for voltage and current to be measured independently, the all dry method was preferred due to concerns of the stability of p-ZnO during exposure to solvents. The photolithography mask for the four-point measurement also has resistive heating elements to generate a temperature gradient across the device, allowing for single-nanowire Seebeck measurements. Ti/Au was used as the contact metal and Ohmic contact was achieved after rapid thermal annealing (*155, 162*).

For ZnO nanowires and ZnO:Li prepared by low doping temperatures (< 500 °C), the two-point single-nanowire FET devices displayed a gating effect typical of n-type semiconductors with moderate carrier concentrations (Figure 2.18a). The transconductance plot (I_{sd} vs V_g, V_{sd} = 0.5 V) shows a turn-on voltage (V_{th}) at negative gate voltage, no measurable current through the wire below the V_{th}, linear increase of the current above V_{th} (Figure 2.18b). For ZnO:Li nanowires prepared with doping temperatures over the range of 500–770 °C, *normally off*

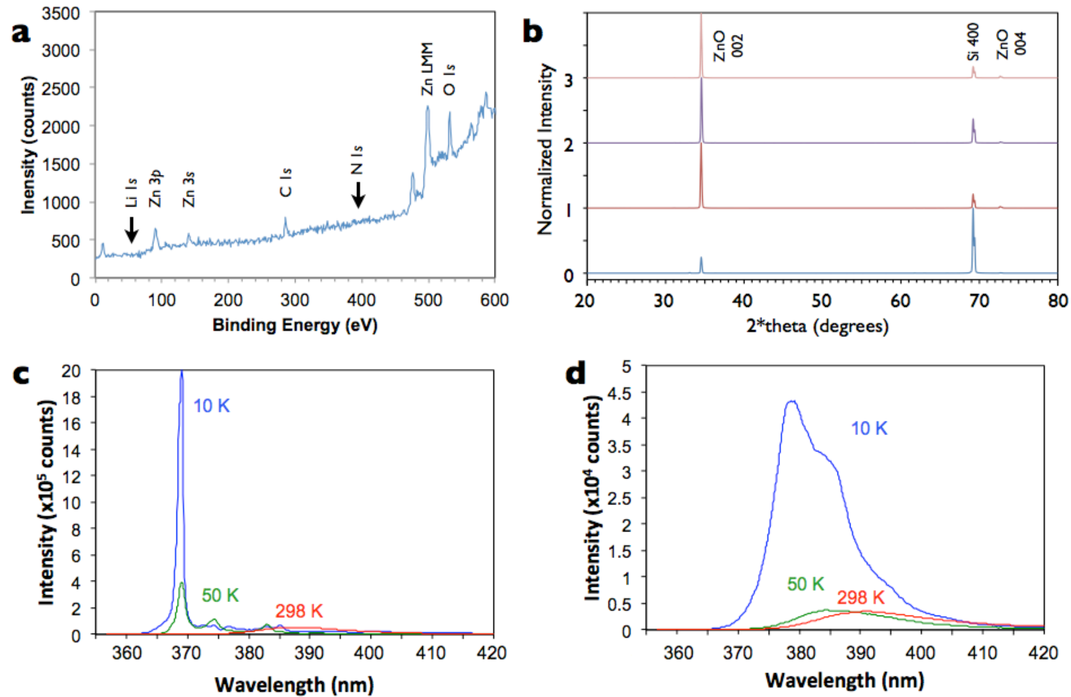

Figure 2.17: Characterization of ZnO:Li nanowires. **a**) X-ray photoelectron spectrum of Li_3N-doped ZnO nanowires. Peaks are observed for Zn, O, and C, but not Li or N. **b**) X-ray diffraction pattern of highly-oriented Li_3N-doped ZnO nanowires. **c-d**) Photoluminescence emission spectra for ZnO (**c**) and Li_3N-doped ZnO nanowires (**d**) at 10 K, 50 K, and 298 K.

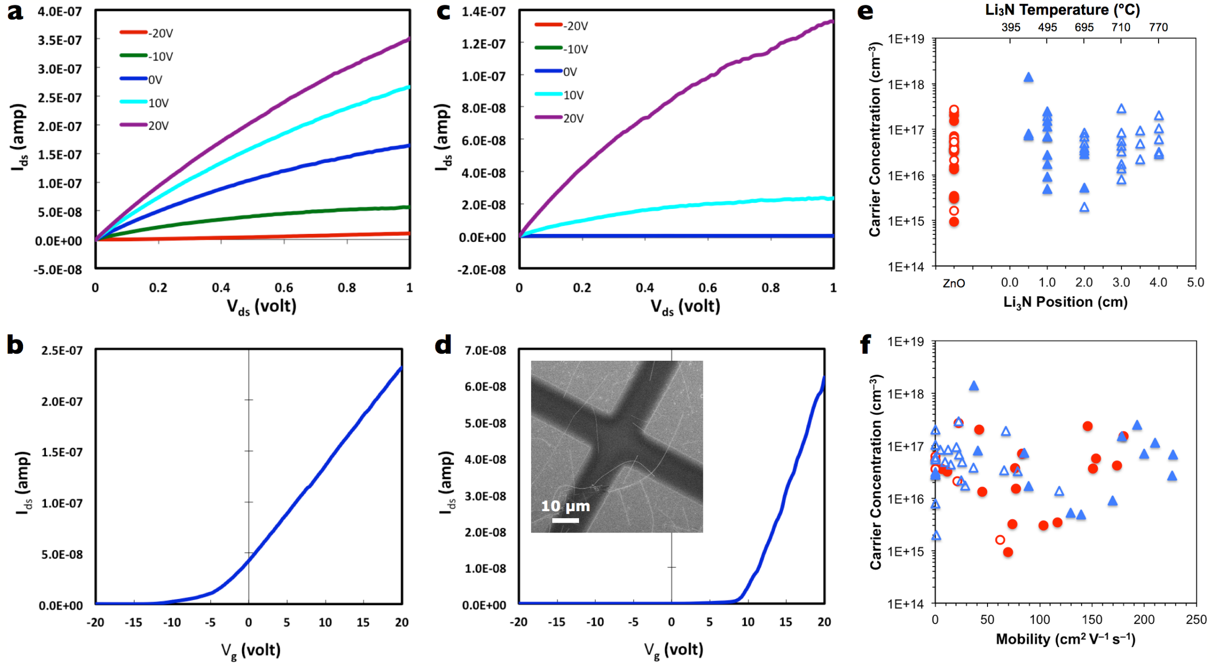

Figure 2.18: Single-nanowire FET devices for carrier concentration determination. a-d) *I-V* curves for ZnO (**a-b**) and 3.5-cm Li_3N-doped ZnO (**c-d**) nanowires. In (**a**) and (**c**), I_{sd}-V_{sd} behavior is plotted for several gate voltages and indicates Ohmic n-type semiconductor behavior. In (**b**) and (**d**), the transconductance plot is shown for two devices with V_{sd} = 0.5 V. For ZnO (**b**), this FET device has a negative V_{th} and is characterized as normally-on, while ZnO:Li (**d**) displays a positive V_{th} and is characterized as normally-off. **d, inset**) SEM image of a two-point FET-device defined by a TEM grid mask and an e-beam evaporated metal film. **e-f**) FET-measured carrier concentration has a function of Li_3N position and temperature during growth (**e**) and field-effect mobility (**f**). Normally-on FET behavior (**b**) is indicated by red, filled circles and normally-off FET behavior (**d**) is indicated by blue, open circles.

FET behavior is observed (Figure 2.18d), meaning that the V_{th} occurs at positive gate voltage, indicating that the nanowire has very poor conductivity, possibly due to the conduction channel being fully depleted (*178*). For samples above 740 °C, a very large number of the prepared FET devices were completely insulating and showed no gate response.

The field-effect mobility can be determined by the slope of the linear region of the transconductance plot,

$$\frac{dI_{sd}}{dV_g} = \frac{\mu C}{L^2}, \tag{4}$$

where μ is the mobility, C is the capacitance, and L is the length of the nanowire channel (*155, 162*). The capacitance is determined by the device materials and dimensions,

$$C = \frac{2\pi\varepsilon_0\varepsilon_{SiO_2}L}{\ln\left(\frac{4h}{d}\right)}. \tag{5}$$

The capacitance equation assumes that the nanowire is completely surrounded by gate dielectric, which is not true for our device geometry. This is an acceptable assumption for nanowires with

diameters below 100 nm, but in large nanowires, the applied electric field from a bottom-gate is non-uniform and poorly modeled by equation (5). Assuming the validity of the capacitance model and that field-effect mobility is a reasonable value, the carrier concentration for *normally on* FET devices is given by

$$n_c = \frac{V_{th} C}{q\pi\left(\frac{d}{2}\right)^2 L}. \qquad (6)$$

This equation does not hold for normally off devices, which returns a meaningless negative number.

The carrier concentration of single nanowires from several Li_3N-doped ZnO nanowire conditions is aggregated in Figure 2.18e, with negative results (from normally off devices) shown in empty shape data points. There is no apparent trend in carrier concentration as a function of the preparation conditions, although there is a clear trend in device behavior: almost all devices from $T_{Li} \geq 695$ °C are normally off. However, analysis of the mobility results indicates that there is also a very large range in calculated mobilities (Figure 2.18f). Mobilities larger than 100 cm/Vs are unrealistic for ZnO and suggest that the NW-FET model does not hold here, probably due to large nanowire diameters and low carrier concentrations.

Annealing the as-grown samples in oxygen at 450 °C for 30 minutes successfully converted the as-grown Li_3N-doped ZnO ($T_{Li} = 770$ °C) to p-type behavior (*177*). Out of concern over the two-point FET devices, these devices were prepared using the four-point probe, which would allow for more accurate FET measurements as well as a Seebeck coefficient measurement, which gives an unambiguous positive or negative value for p-type or n-type majority carrier behavior. FET measurements were performed on a single device before and after annealing, which showed the change from n-type to p-type conduction for the nanowire FET device. The Seebeck measurement was also in agreement, showing the change from approximately –400 μV K^{-1} to +400 μV K^{-1}, which corresponds n-type and p-type behavior, respectively. Follow-up experiments are now being carried out to reproduce the experimental results and study the stability of these p-ZnO nanowires.

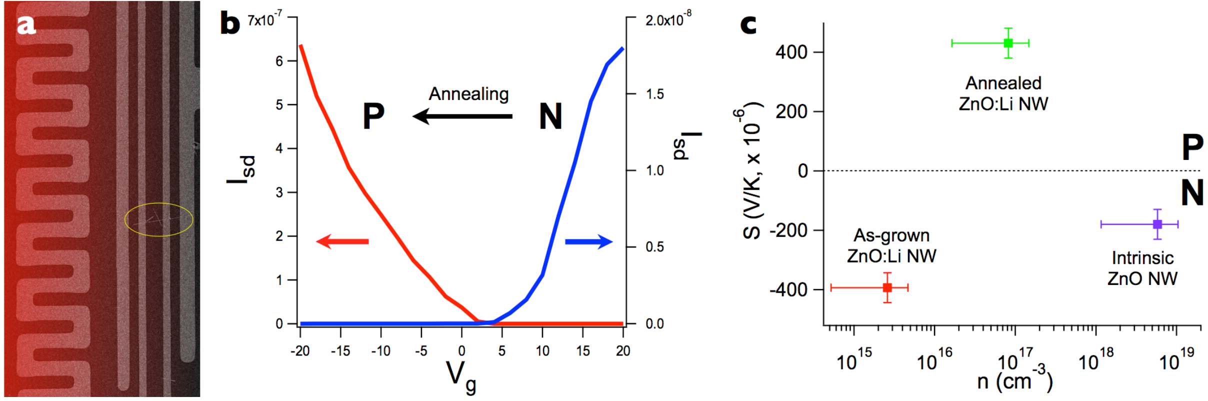

Figure 2.19: p-Type behavior in ZnO nanowires after thermal activation. a) An SEM image of the four-point probe used to characterize FET performance and the Seebeck coefficient before and after annealing. The circle is added to highlight the position of the nanowire. False-color added to show temperature gradient during Seebeck measurement. b) I_{sd}–V_g curve showing FET behavior before (blue, N) and after (red, P) annealing. c) The measured Seebeck coefficient versus FET-calculated carrier concentration for intrinsic ZnO (purple), as-grown ZnO:Li (red), and thermally-activated p-ZnO (green).

3. Indium oxide–zinc oxide alloy nanowires

While nearly all single elements and binary compounds have been characterized and evaluated for potential applications, ternary and quaternary compounds present a vast number of unexplored materials. These multicomponent materials provide an opportunity to tune the structural and physical properties to the requirements for specific technological applications. In this chapter, we look at alloys of zinc oxide with tri-valent metal oxides such as indium, gallium, and iron oxide. These materials display enhanced optical and transport properties that are potentially useful in energy applications. A simple solid state reaction allows for the preparation of several new nanowire compositions in the indium oxide-zinc oxide crystal structure system. Using optical measurements and single-nanowire thermal and electrical measurements, these materials are evaluated for applications in photoelectrochemical water oxidation, transparent conducting oxides, and thermoelectric materials.

Parts of this chapter were previously published in Chemical Science. S. C. Andrews, M. A. Fardy, S. Aloni, M. Zhang, V. Radmilovic, and P. Yang. Atomic-level control of the thermoelectric properties in polytypoid nanowires, *Chemical Science* **2**, 706 (2011) - Reproduced by permission of The Royal Society of Chemistry.

3.1. Introduction

The indium oxide–zinc oxide alloy system has the peculiarity of forming a periodic structure of single layers of indium oxide interspersed between layers of zinc oxide with near-perfect periodicity (*179, 180*). The periodicity of the structure is related to the ratio of indium oxide to zinc oxide indicated by the chemical formula, $In_2O_3(ZnO)_n$, where $n+1$ layers of ZnO form for every layer, or inclusion, of indium oxide. Indium zinc oxide alloys have typically been prepared as bulk powders by mixing stoichiometric amounts of indium oxide and zinc oxide and annealing at temperatures in excess of 1100 °C to induce solid-state diffusion (*181*). The phase diagram in Figure 3.1 shows the different phases formed over the range 1100–1400 °C, as well as how n corresponds to Zn concentration. Later work has expanded this crystal structure to alloys of zinc oxide with gallium oxide, iron oxide, and other tri-valent metals (*182-185*). Additionally, mixtures of metals can be used in varying ratios, such as indium gallium zinc oxide (IGZO), $In_{2-x}Ga_xO_3(ZnO)_n$. The term *metal* zinc oxide (MZO) is used to describe the general family of materials with the chemical formula $R_{2-x}M_xO_3(ZnO)_n$ and an IZO-like structure without regard to specific elemental composition.

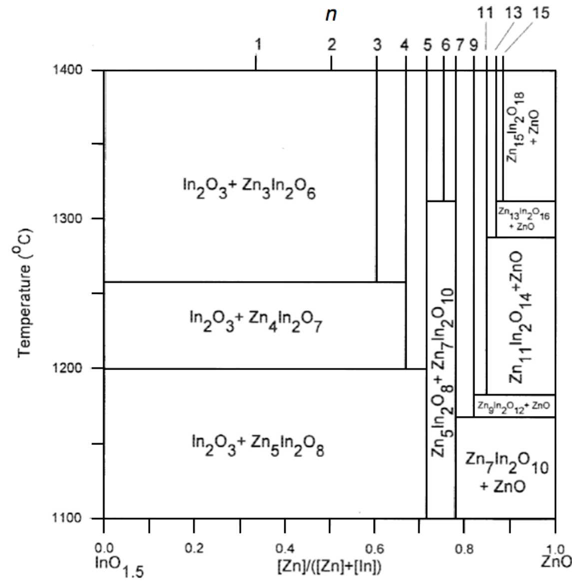

Figure 3.1: Phase diagram of In_2O_3-ZnO system. The lower x-axis indicates Zn at % and the upper x-axis represents *n*, which describes the periodicity of the crystal structure by the chemical formula, $In_2O_3(ZnO)_n$. This image was adapted from reference (*181*).

The structure of indium zinc oxide (IZO) and related structures have been an area of intense research. Zinc oxide adopts the wurtzite crystal structure, with hexagonal close-packed O anions stacking in the [001] direction and Zn cations filling half of the tetrahedral holes. In IZO, a close-packed layer of InO_2^- (edge sharing InO_6 octahedra) insert between ZnO (002) planes (Figure 3.2). Each oxygen in the InO_6 octahedra is shared with one ZnO tetrahedron, resulting in an inversion of the wurtzite structure across the InO_2^- layer, known as an inversion domain boundary (IDB) (*185, 186*). The InO_2^- inclusion layer is also associated with a stacking fault, which together with the IDB, results in a stacking sequence of AaBbAaB**bAc**CaAcCaA (capital and lowercase letters correspond to metal and oxygen atoms, respectively). As a result, the wurtzite lattice is translated by 1/3<100> on opposite sides of the InO_2^-. The location of the octahedral InO_2^- within the stacking sequence is denoted by the bold **bAc**.

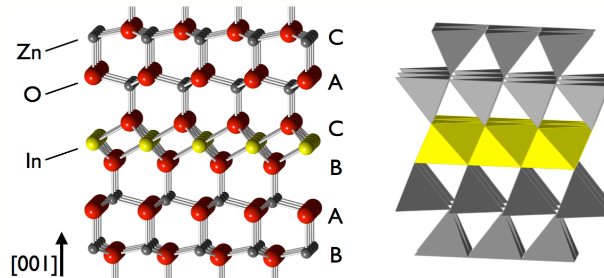

Figure 3.2: Indium octahedral layer. Atomic and polyhedra structure models of indium zinc oxide around the indium oxide inclusion. The InO_2^- layer is position between ZnO (002) layers and inverts the wurtzite lattice, changing stacking from ABAB to ACAC. Zinc cations and polyhedra are indicated in gray, oxygen anions in red, and indium cations and polyhedra in yellow.

In order to form a bond with the neighboring InO_2^- layer, the wurtzite "slab" must contain a second inversion domain boundary to reorient the polarity of the lattice (*187*). Early structure models identified that InO^+ trigonal bipyramidal defects could serve to reinvert the polarity and restore charge balance, but disagreed as to whether they were randomly distributed in the wurtzite slab or formed an additional planar layer (*184, 188*). "Zigzag" contrast patterns within the slab layers were identified as a second form In ordering, but were too poorly resolved to lead to a structure and were inconsistently observed, especially for $n < 6$ (Figure 3.3a) (*189-192*). The complete structure was finally solved by density functional theory (DFT) calculations, which determined that the zigzag IDB structures created less lattice strain and were more energetically favorable than other IDB configurations (Figure 3.3b) (*187, 193*). These DFT calculations also suggested that the lattice strain of a planar InO^+ trigonal bipyramidal layer decreases as the thickness of the $InZn_nO_{n+1}^+$ slabs decreases, possibly accounting for the absence of zigzags in low-*n* compositions (*193*). The decreased coordination number of the zigzag defect means that it is preferentially filled by the smaller cation when multiple defects are present, such as Ga in IGZO (*193*). Thus, in terms of the generalized chemical formula for MZO, the structure can be broken into RO_2^- layers and $MZn_nO_{n+1}^+$ slabs, where *R* is larger than *M*.

Group-III elements have long been used as substitutional dopants in zinc oxide to improve n-type electrical conductivity (*194*). As a low-indium alternative to indium tin oxide, amorphous IGZO is of particular interest as a transparent conducting oxide, as the defect band position of gallium substitutions allows it to be populated at room temperature (*195*). The lattice strain created by accommodating larger indium atoms in IZO results in a decrease in the band gap, which has generated interest in its application for photoelectrochemical water oxidation (*196*). The octahedral and zigzag layers disrupt phonon transport, reducing the thermal conductivity of IZO. The combination of low thermal conductivity and high electrical conductivity makes IZO particularly interesting as a thermoelectric material (*197*).

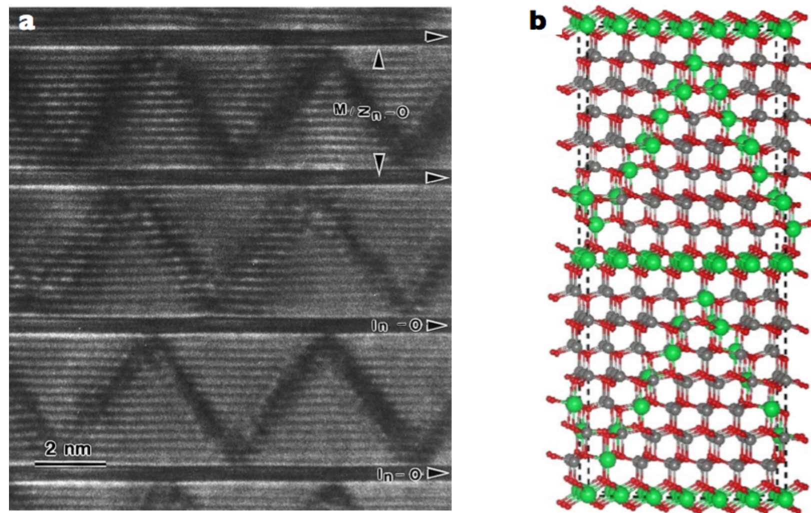

Figure 3.3: Zigzag modulation layers. **a**) TEM image of zigzag modulation layers in $In_2O_3(ZnO)_{13}$. **b**) The predicted structure model for $In_2O_3(ZnO)_6$, showing the zigzag modulation layers in the $InZn_nO_{n+1}^+$ slab. The large green, medium gray, and small red balls indicate the In, Zn, and O atoms, respectively. These images were adapted from references (*190, 193*).

Oxide materials are an area of research for thermoelectric devices due to their low thermal conductivity, high stability, and general low cost and abundance, although low electrical conductivity remains an obstacle (*198*). Aluminum-doped zinc oxide was reported to have a zT of 0.3 at 1273 K, remarkably high for a material without any nano-structuring (*194*). New oxide materials with complex crystal structures, such as layered cobalites and doped perovskites, have even higher zT values (*46, 198*). Indium zinc oxide has been investigated as a thermoelectric material due to its nanoscale features for phonon scattering and increased electrical conductivity from n-type doping by group-IIIa substitutional defects. Several reports have agreed on a zT value of approximately 0.1 at 1000 K for bulk indium zinc oxide, with values as high as 0.33 at 1073 K for yttrium-substituted $In_2O_3(ZnO)_5$ (*197, 199-202*).

Efforts are now underway to prepare indium zinc oxide thin films and nanowires to further study and develop these possible applications. IGZO thin films have been prepared by laser ablation of IGZO bulk powder to deposit an amorphous layer on a ZnO substrate by and followed with annealing at 1400 °C to produce a single-crystalline film (*203*). IZO and IGZO nanowires have been grown using a chemical vapor transport synthesis similar to the ZnO nanowire CVT synthesis described in Chapter 2 (*204-206*).

3.2. Conversion synthesis of indium-zinc-oxide-structured nanowires

The CVT synthesis of zinc oxide nanowires provides various methods to control material parameters such as diameter, length, nanowire orientation, and nanowire density. An ideal synthesis for $R_{2-x}M_xO_3(ZnO)_n$ nanowires would allow for easily manipulation of R and M elemental identities, elemental ratio (x), and (R+M):Zn ratio (n) with perfect sample uniformity, in addition to retaining control of all nanowire and array properties. However, simultaneous control of all of these parameters rapidly increases the complexity and difficulty of the synthesis. CVT-grown IZO and IGZO nanowires syntheses usually exhibit poor morphology control and sample uniformity issues (*205-208*).

Utilizing a three-step process shown schematically in Figure 3.4, the conversion method for MZO nanowires allows for better control of the material composition, structure, and properties through rational manipulation. First, ZnO nanowire arrays are grown using a CVT synthesis, which allows for control of general nanowire dimensions and array properties. The nanowire arrays are coated with 5-25 nm of various metals using thermal and electron beam evaporation systems. For some metals, it is necessary to use an oxygen plasma etcher to oxidize the metal coating. The sample is then annealed at 900 °C in oxygen gas to form arrays of polytypoid alloy nanowires. Since as much as 100 nm of metal coating may be necessary to achieve low n compositions for typical ZnO nanowire dimensions, the metal deposition and annealing steps are repeated as many times as necessary.

Many metals can be deposited using an e-beam evaporator, including indium, gallium, iron, erbium, and yttrium (a limited number may deposited by thermal evaporation but include indium and gallium). By using a quartz crystal monitor to measure film thickness, mixed metal ratios can be controlled, as well as total metal loading for controlling (M+R):Zn ratio. Several

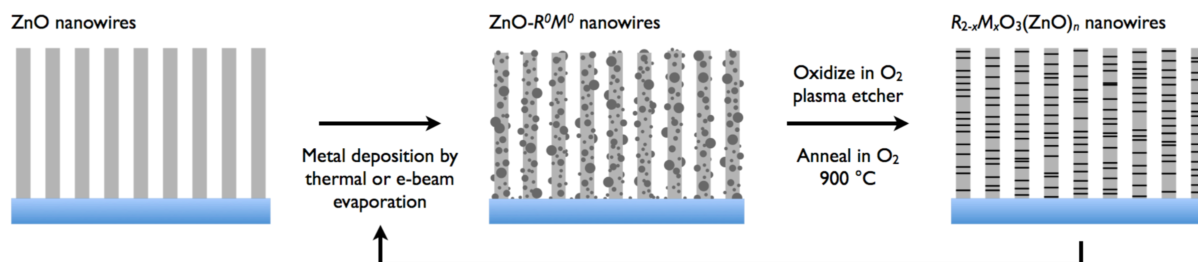

Figure 3.4: Schematic illustration of the synthetic method.

elemental compositions of MZO nanowires have been prepared the conversion synthetic method, including IZO, IGZO, indium iron zinc oxide (IFZO), gallium zinc oxide (GZO). TEM images of inclusion formation and elemental analysis (energy-dispersive x-ray spectroscopy) are primarily used to confirm the reaction products (Figure 3.5). While bulk powder preparations of group-IIIb- and lanthanide-series-containing compositions, as well as iron zinc oxide, have been reported in literature (*182, 183, 199, 209*), these compositions have not been prepared as nanowires using the conversion method, most likely due to the very high annealing temperatures required.

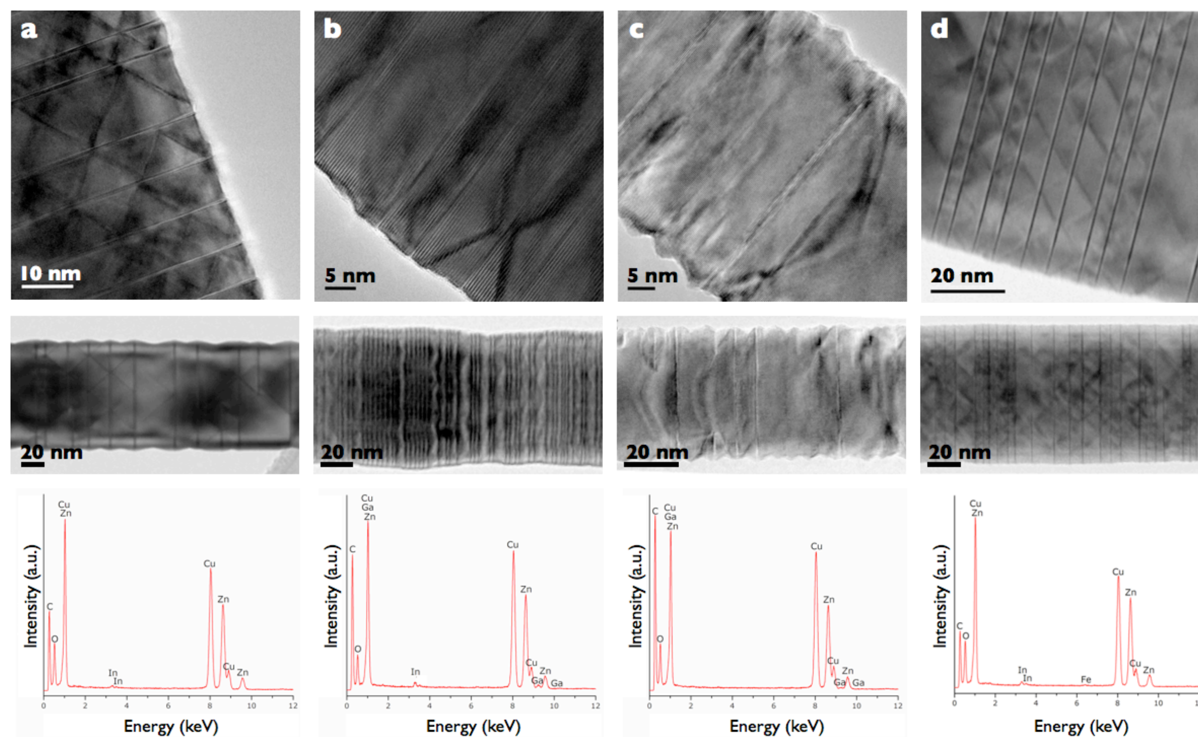

Figure 3.5: MZO nanowires. TEM images (top, middle) and energy-dispersive x-ray spectra (bottom) of nanowires prepared with 15 nm of In (**a**), 10 nm of In and 10 nm of Ga, x≈1 (**b**), 10 nm of Ga (**c**), and 5 nm of In and 5 nm of Fe, x≈0.67 (**d**).

One major limitation of the conversion synthesis is that a true single-phase composition is never obtained in MZO nanowires. This is primarily due to the natural variability of bottom-up grown nanowires, the inhomogeneity of the evaporator-deposited metal coating, and the tendency for metal coating to melt, form droplets, and diffuse. Rather than referring to a specific *n* value for the MZO nanowires prepared by conversion, prepared samples are referred to by the metal coating thickness, e.g. 15 IZO, 10/10 IGZO, 10 GZO, and 5/5 IFZO in Figure 3.5. Replacing the evaporator-deposited metal coating with a conformal technique such as atomic layer deposition would help improve the uniformity of single nanowires, but the nanowire array would still be vary according to the ZnO nanowire diameter distribution.

3.3. Typical methods for conversion synthesis

The ZnO nanowire arrays are grown using the previously discussed chemical vapor transport and VLS catalyzed methods (see Section 2.2). The metal evaporation source is located above the nanowire array and cannot coat the nanowires even from top to bottom. For this reason, vertically-oriented, low-density nanowire arrays are ideal. Arrays of shorter nanowires also mitigate coating inhomogeneity, but nanowire lengths of at least 10 μm are needed for single-nanowire transport measurements. Smaller diameter nanowires require less amount of metal loading to achieve smaller *n* values. The substrate must also be stable to at least 900 °C, if not 1100 °C. To achieve these requirements, samples are prepared on sapphire a-plane (11-20) substrates using 20 nm gold colloids (diluted 1:150) as a VLS catalyst. The Au colloids allow for significantly lower density arrays and smaller nanowire diameters than a sputtered Au film, but reduce the verticality of the synthesis (Figure 3.6).

The substrates were mounting on a rotating, unheated stage in a combined thermal and electron beam evaporation system. Sources are positioned normal to the stage, so the substrates were mounted with a ~10° angle to increase vapor penetration into the nanowire. Indium and gallium metal are typically deposited by thermal evaporation, while iron and other metals are deposited by e-beam evaporation, using a 0.1-0.4 Å/s deposition rate. The order of metal deposition was not observed to have any effect for IGZO or IFZO nanowires. Deposition of a

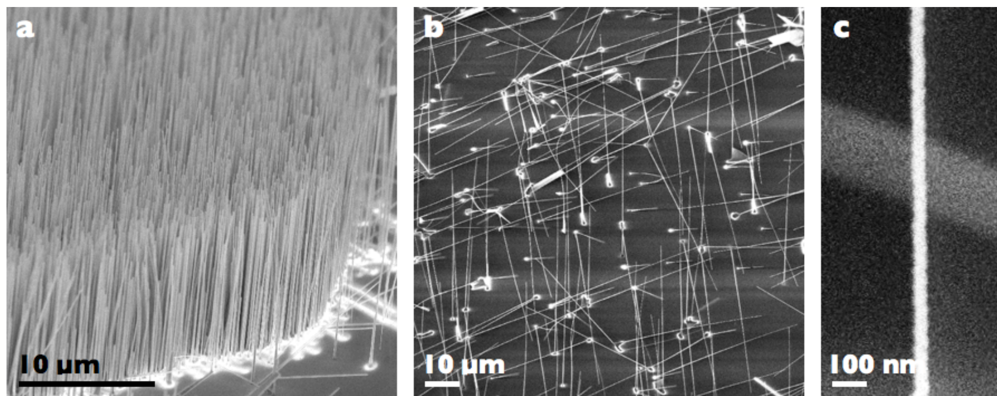

Figure 3.6: ZnO nanowire arrays. a-b) prepared from sputtered Au (**a**) and 30 nm Au colloids (**b**). **c**) This isolated nanowire measures 42 nm in diameter.

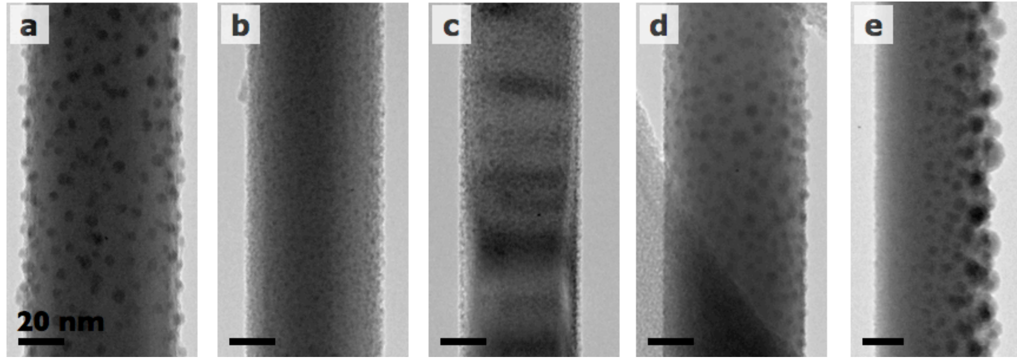

Figure 3.7: Unannealed metal-coated ZnO nanowires. TEM images of ZnO nanowires coated with 10 nm of In (**a**), 10 nm of Ga (**b**), 5 nm of In and 5 nm of Fe (**c**), 5 nm of In and 5 nm of Ga (**d**), and 10 nm of In and 10 nm of Ga (**e**),

mixed metal coating of 10 nm of In and 10 nm of Ga results in a non-conformal coating of metal droplets on the nanowire surface (Figure 3.7). Using an oxygen plasma to oxidize the metal coating has been shown to improve alloy formation in some alloy systems, particularly for IZO. The substrates were oxidized using a 18 W plasma etcher for 30 minutes in 200-300 mTorr of O_2 gas.

Solid state diffusion of the metal coating into ZnO nanowires is accomplished by annealing at high temperatures. Indium inclusion formation has been observed as low as 800 °C but occurs appreciably at temperatures of 900 °C and higher. ZnO nanowires decompose readily at these temperatures in inert atmosphere and in air. Oxygen gas is used as the carrier gas with a approximate flowrate of 50 sccm. At 900 °C, indium inclusion formation occurs rapidly, with partial inclusions visible after 5 minutes. Due to ZnO decomposition, it is ideal to keep the annealing time as short as possible: one hour at 900 °C is usually sufficient. However, MZO nanowires display better thermal stability and are stable at 900 °C for several days. At this temperature, no significant differences are observed in IGZO samples annealed for 4 hours and 96 hours; periodicity or sample uniformity do not appear to improve with further annealing at 900 °C. In addition, no significant differences are observed in samples that are rapidly cooled versus samples with slow (10°C/min) cooling rates.

3.4. Structural analysis of conversion-synthesized MZO nanowires

3.4.a. Structural analysis of IGZO nanowires

The solid-state diffusion process used to generate the MZO nanowires maintains the original morphology of the nanowire array and only minor etching is observed, as seen in the SEM images taken before (Figure 3.8a) and after (Figure 3.8b) alloy formation. The dimension of MZO nanowires made in this study vary depending on the ZnO nanowire synthesis and the overall metal layer thickness. The typical diameters of the initial nanowires are 80-130 nm for

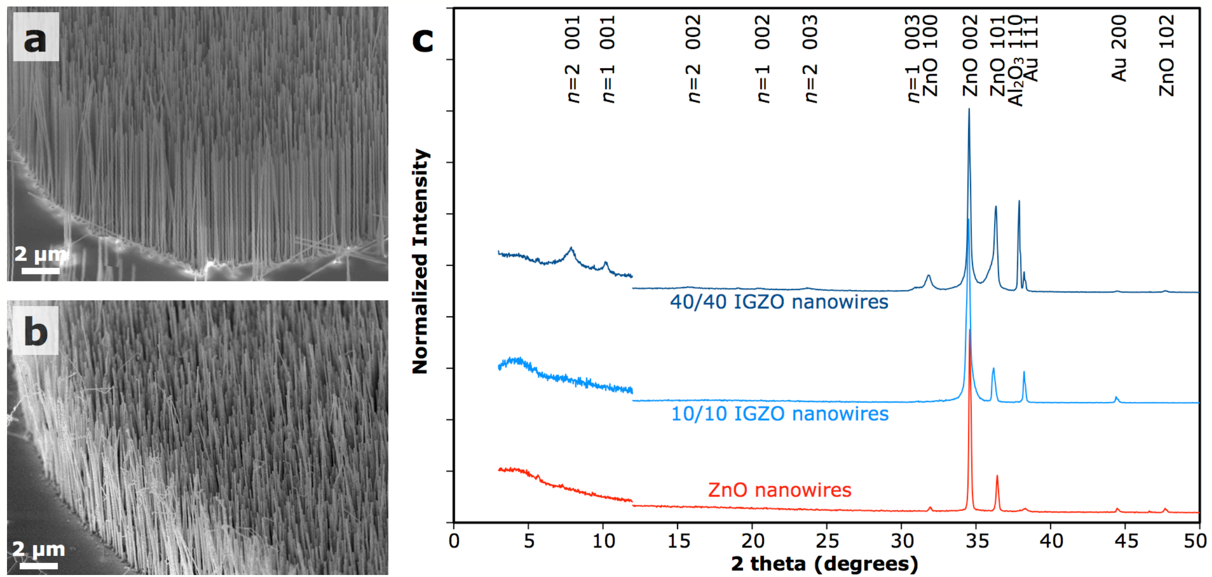

Figure 3.8: XRD and SEM of IGZO nanowire arrays. a-b) Scanning electron microscope images of ZnO (**a**) and 10/10 IGZO (**b**) nanowires. **c**) X-ray diffraction of ZnO (bottom), 10/10 IGZO (middle), and 40/40 IGZO (top) nanowires using a Cu K_α source. The peaks at 10° and 7° correspond to the n = 1 and n = 2 spacings predicted for IZO. The weak peak at 5° is an instrument artifact.

sputtered-film-grown ZnO and 30-60 nm for colloid-grown ZnO. The strong 002 peak in the x-ray diffraction (XRD) pattern indicates that the ZnO nanowire array is highly oriented and largely maintains the orientation after the conversion (Figure 3.8c). No In_2O_3 or Ga_2O_3 peaks were observed in the 10/10 IGZO sample, but the weak unidentified peaks in the 40/40 IGZO sample may belong to an alloy of indium and gallium oxide. In the IGZO nanowire alloys, there is little shift from the position of the ZnO nanowire diffraction peaks, but peak broadening towards smaller angles is observed, suggesting the formation of non-uniform alloys. No peaks below 30° are observed for ZnO or 10/10 IGZO, but new peaks appear in the low-angle region (<10°) for the 40/40 IGZO sample, corresponding to spacings of 0.86 and 1.12 nm, which are in good agreement with the predicted lattice constants for IZO with n = 1 and n = 2 (*193*). The relative peak heights suggest that n = 2 is the dominant composition in 40/40 IGZO. In addition, weak higher-order peaks for n = 1 and n = 2 are observed in the 15-30° range.

Transmission electron microscope (TEM) images of 10/10 IGZO nanowires (Figure 3.9a) show modulated contrast along their longitudinal axis in nearly all nanowires imaged, which can be attributed to the formation of the indium inclusion layer. To confirm the structure of our nanowires, Z-contrast scanning transmission electron microscopy (STEM) imaging was done using a 300 kV double-Cs-corrected STEM capable of 50 pm resolution. In Z-contrast images, the intensity is approximately proportional to the mean square of the atomic number of the constituent atoms. Thus, using Z-contrast imaging, the position of In (Z = 49) can be unambiguously determined, but Ga (Z = 31) and Zn (Z = 30) cannot be distinguished from one another since their atomic numbers differ by only one. Oxygen cannot be imaged due to its relatively small atomic number. Figure 3.9b is a Z-contrast image of a 10/10 IGZO nanowire clearly showing the presence of In-enriched layers (brightest lines) oriented perpendicular to the [001] direction, in agreement with the bulk IZO structure.

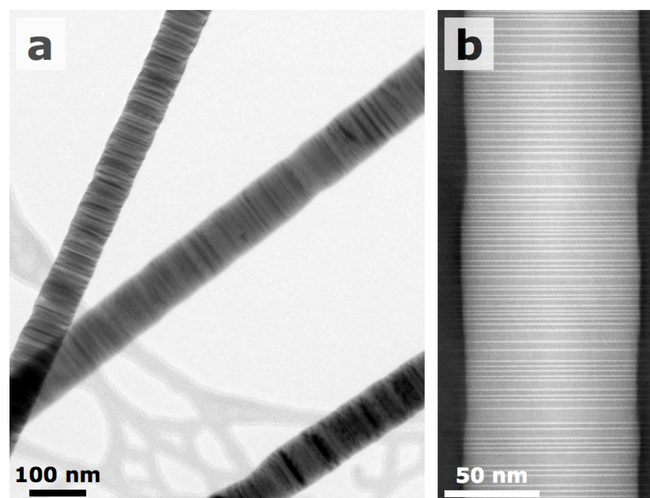

Figure 3.9: IGZO nanowires. **a**) TEM image of multiple IGZO nanowires. **b**) Z-contrast STEM image of a 10/10 IGZO nanowire. The Z contrast in the image clearly shows that In atoms are preferentially located within layers oriented perpendicularly to the nanowire growth direction.

Energy dispersive x-ray spectrometry (EDS) confirms the presence of In, Ga, and Zn in the IGZO nanowires (Figure 3.5), with an In:Ga atomic ratio of approximately 1:1 in all nanowires. The (In+Ga):Zn ratio varies depending on the diameter of the starting ZnO nanowire and local metal coating thickness. EDS two-dimensional mapping is used to study elemental concentration in a 28 nm x 50 nm region of 10/10 IGZO. The STEM image in Figure 3.10a is overlaid with EDS maps in for In, Ga, and Zn in Figure 3.10b-d. The In map shows that In is concentrated in single layers perpendicular to the nanowire and correspond with the bright regions in STEM, while Ga and Zn tend to be present throughout the region. While a decrease in Zn signal is observed at the octahedral layers, Ga appears to also concentrate in the octahedral layers, suggesting that their true composition is $In_{1-x}Ga_xO_2^-$. Zigzags were seen in all four types of alloys synthesized in this study (Figure 3.5), but were not apparent in those alloys with small *n*. Also, since the trigonal bipyramidal sites may be occupied by In, Ga, or Zn atoms in the IGZO nanowires, the zigzags appear faint in the Z-contrast images and in some cases are not discernable.

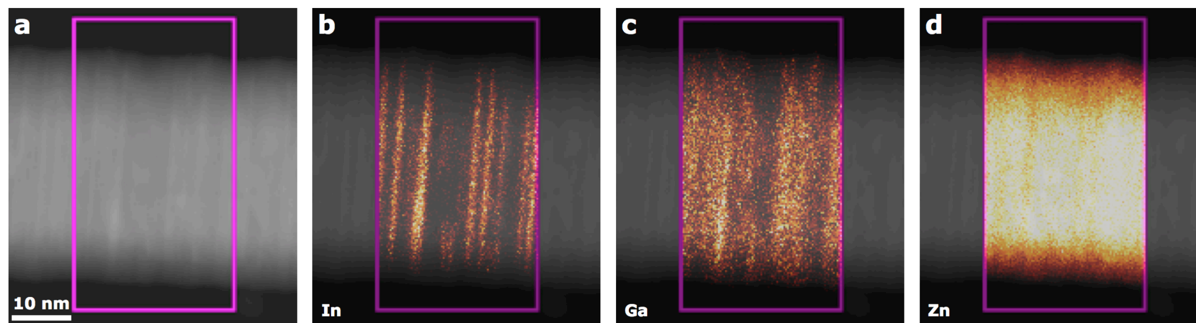

Figure 3.10: EDS Mapping of IGZO nanowires. STEM image of an IGZO nanowire (**a**) and the corresponding EDS element maps for In (**b**), Ga (**c**), and Zn (**d**) overlaid on the original image.

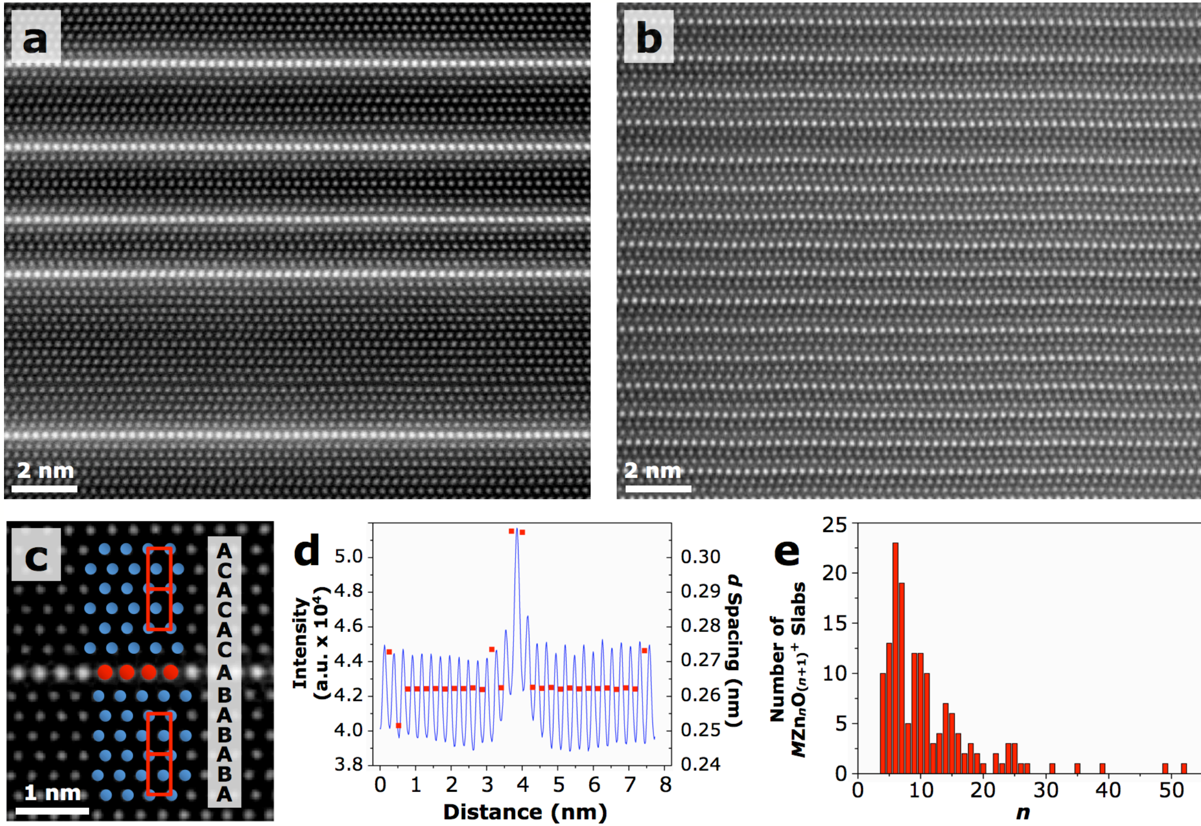

Figure 3.11: HR-STEM of IGZO nanowires. a-b) HR-STEM image of 10/10 IGZO (**a**) and 40/40 IGZO (**b**) nanowires showing individual RO_2^- layers sandwiched between multiple $MZn_nO_{n+1}^+$ layers. **c**) HR-STEM image highlighting the change in stacking sequence across a RO_2^- layer. **d**) Intensity line profile and *d* spacing across a RO_2^- layer taken from a HR-STEM image. On either side of the inclusion, the *d* spacing shows an expansion of ~17% relative to that of pure ZnO. **e**) Frequency of different *n* values of the $MZn_nO_{n+1}^+$ layers measured from HR-STEM images of several 10/10 IGZO nanowires.

High-resolution (HR)-STEM is used to confirm that the atomic structure of converted IGZO nanowires is the MZO structure, as shown in Figure 3.11a-b for 10/10 and 40/40 IGZO. The In atoms sit on individual planes and are separated by wurtzite $MZn_nO_{n+1}^+$ slabs of varying thickness, although zigzags are rarely observed. Only single layers of In atoms were observed in the 10/10 IGZO nanowires, consistent with the layers being composed of octahedrally-coordinated InO_2^-, which has been shown to be the most stable configuration for In within the MZO structure (*193*). Careful study of Figure 3.11a reveals the IDB and stacking fault behaviors of the octahedral layer, diagrammed in Figure 3.11c. In agreement with XRD, the *d* spacings in the $MZn_nO_{n+1}^+$ layers are unchanged from (002) in pure ZnO (0.26 nm), but the octahedral RO_2^- planes force a local 17% increase in the *d* spacing (0.30 nm) on either side of the inclusion layers (Figure 3.11d). The *d* spacings were determined by taking an intensity line profile across an inclusion in a HR-STEM image and measuring the distance between peaks. This change in *d*-spacing on either side of the In/Ga inclusions corresponds with that reported by Yan et al. and Jie et al. on IZO (*186, 204*). This significant increase in *d* spacing around the inclusion layer is associated with a large amount of lattice strain.

To approximate an n value for the 10/10 IGZO nanowires, the number of atomic layers in each $MZn_nO_{n+1}^+$ slab was counted for several nanowires Figure 3.11e). The average n is 11, but the most frequent is 6. n can be related to the inter-inclusion spacing (ℓ) between RO_2^- layers by the following equation:

$$\ell(\text{nm}) = 0.61_4 + 0.26_2\, n, \qquad (7)$$

where 0.61_4 nm corresponds to twice the distance of the d spacing immediately adjacent to the RO_2^- octahedral layers and 0.26_2 nm corresponds to the (002) d spacing for wurtzite within the $MZn_nO_{n+1}^+$ slabs (subscripts indicate insignificant figures). Using equation *(7)*, the average spacing between RO_2^- octahedral layers in the 10/10 IGZO nanowires 3.50 nm and the most frequent is 2.19 nm.

The amount of metal deposition was varied to determine its effect on RO_2^- layer density (Figure 3.12a-d). The surface of the 40/40 IGZO nanowire shown in Figure 3.12d appears rough due to the presence of oxide particles left over after the solid-state diffusion process. However, most IGZO nanowires in the sample did not show surface particles. Line intensity profiles drawn perpendicular to the RO_2^- inclusions were used to generate power spectra (Figure 3.12e-h) from the HR-STEM images shown in Figure 3.12a-d. The power spectra show the most common frequencies ($1/\ell$) within the nanowires, providing information regarding the RO_2^- layer spacings and the periodicity of the spacings. The range of frequencies obtained from the 10/10 IGZO power spectrum match the n values that were manually counted in Figure 3.11e. As the thickness of metal deposition is increased the most common frequencies shift to higher $1/\ell$ (smaller n, smaller ℓ) indicating that the distance between RO_2^- layers decreases with increased metal deposition. The periodicity also increases with metal deposition, which can be seen in the

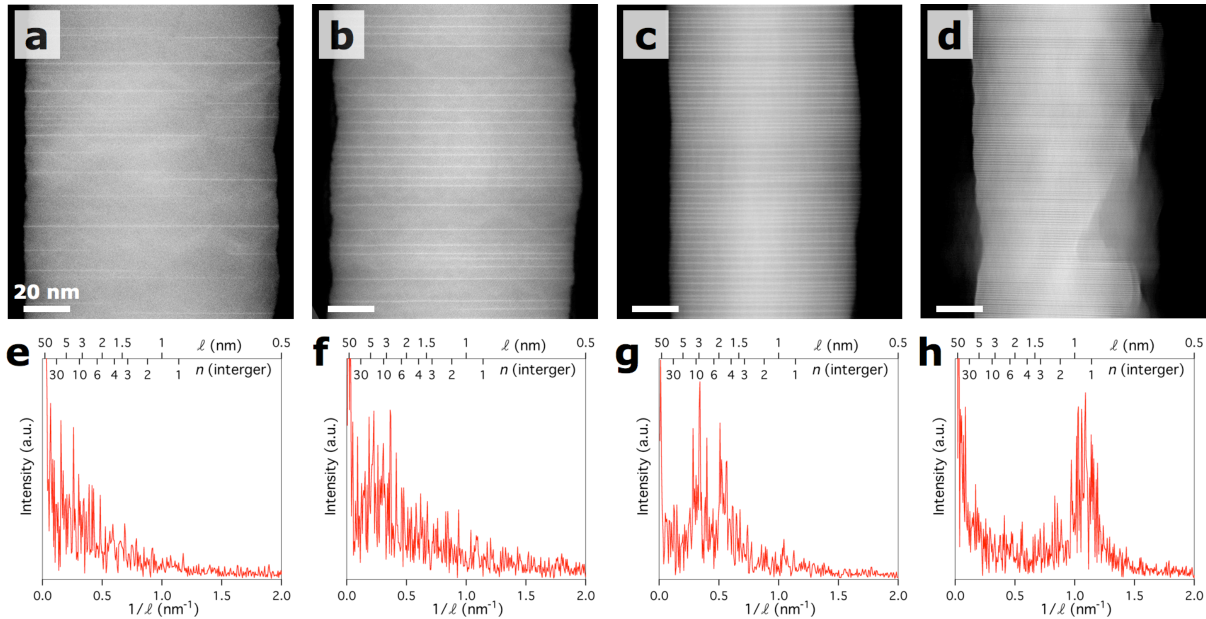

Figure 3.12: IGZO metal coating thickness dependence. a-d) High-angle annular dark field images of annealed IGZO nanowires distinguishes the presence of heavier elements as brighter regions. prepared with 5 nm of In/5 nm of Ga (**a**), 10/10 (**b**), 20/20 (**c**), and 40/40 (**d**). **e-f**) The fast Fourier transform of the line intensity profiles obtained from (**a-d**).

emergence of distinct peaks (Figure 3.12g-h). The power spectrum of 40/40 IGZO indicates that the majority of RO_2^- layers in the 40/40 IGZO are separated by 2 or 3 layers of $MZn_nO_{n+1}^+$, which can be visually confirmed in the HR-STEM image taken from same 40/40 IGZO nanowire sample (Figure 3.11b). While Figure 3.12h only contains information about a single HR-STEM image, it is in good agreement with the XRD measurement on the nanowire array in Figure 3.8c. It is evident from these power spectra that both *n* and the superlattice periodicity can be controllably tuned by adjusting the amount of metal deposition.

3.4.b. Structural analysis of IFZO nanowires

As in IGZO nanowires, manipulation of the *n* value is also easily controlled in the indium iron zinc oxide system by varying the thickness of the metal coating. Figure 3.13 shows the dependence of inclusion density IFZO as a function of metal deposited, from 10 nm In/5

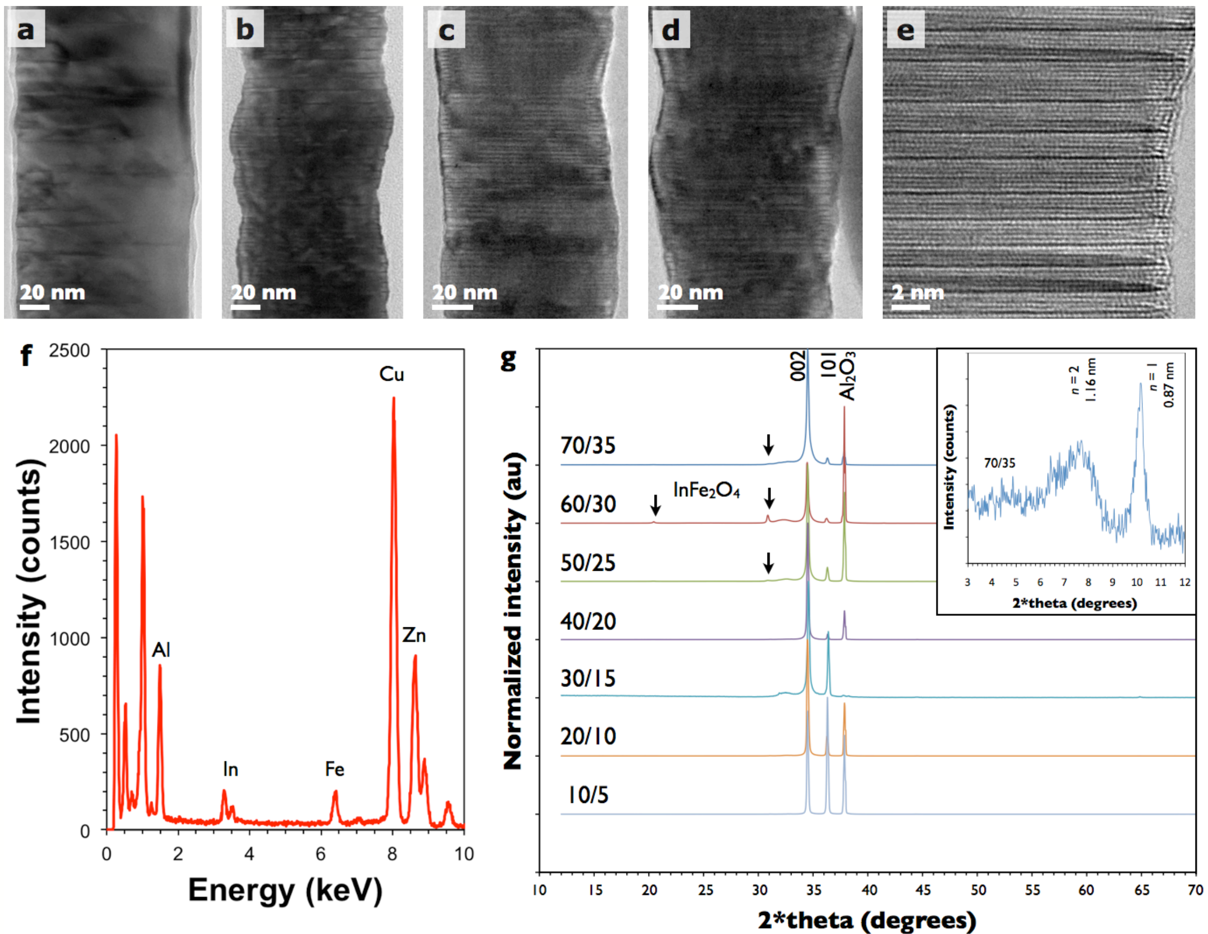

Figure 3.13: IFZO metal coating thickness dependence. a-d) TEM images of annealed IFZO nanowires prepared with 10 nm of In/5 nm of Fe (**a**), 30/15 (**b**), 50/25 (**c**), and 70/35 (**d**). **e**) HRTEM of a 70/35 IFZO nanowire. **f**) EDS spectrum of 70/35 IFZO. **g**) XRD of several IFZO preparations. $InFe_2O_4$ is observed in the samples high metal loadings. Low-angle XRD of 70/35 IFZO showing $n = 2$ and $n = 1$ diffraction peaks (inset).

nm Fe to 70 nm In/35 nm Fe. In 10/5 IFZO (Figure 3.13a), few inclusions are observed and many do not extend completely through the nanowire. However, in Figure 3.13c-d, there is enough metal that the inclusions are completely formed and the average layer spacing is 2.5 nm. Characterization by EDS shows that these samples are 1:1 In:Fe (± 10%) due to the molar volumes of each metal (Fe: 7.1 mol/cm^3, In: 15.7 mol/cm^3). X-ray diffraction indicates that the nanowires arrays remain highly oriented, as only the ZnO 002 and 101 and substrate peaks are observed (Figure 3.13g). For 50/25 IFZO and samples with higher loading, a small amount of $InFe_2O_4$ is observed. In the 70/35 IFZO, low angle peaks corresponding to $n = 1$ and $n = 2$ periodicity is observed.

The high directionality of e-beam evaporated iron (as opposed to thermal evaporation of In and Ga) preferentially deposits at the top of the nanowire array (Figure 3.14a). Additionally, the high melting point of iron acts to limit metal diffusion across the nanowire surface, as in InGa, so highly-loaded IFZO nanowires tend to have a large amount of indium and iron deposited at the nanowire tips, sometimes leading to joined nanowires as shown in Figure 3.14b. Further, HRTEM of the nanowire tips reveal two phases (Figure 3.14c): an IFZO-structured phase and a non-layered phase, which may be the $InFe_2O_4$ phase observed in XRD (Figure 3.13g).

In addition to varying the (In+Fe):Zn ratio, IFZO nanowires were prepared with 1:2 and 1:4 In:Fe ratio (Figure 3.15). Surface particles were observed in the 1:2 and 1:4 In:Fe samples, which were identified as pure Fe_2O_3 by EDS. EDS analysis of particle-free regions of 20/20 and 20/40 IFZO samples revealed enhanced but non-stoichiometric incorporation of Fe, 1:1.6 and 1:1.9, respectively. As previous attempts to prepare $Fe_2O_3(ZnO)_n$ were unsuccessful, it was already known that Fe_2O_3 is unreactive at 900 °C. Given that the phase diagrams for In-Fe and In-Fe-O show that liquid indium metal can accommodate ~1% iron, it is surprising that the diffusion of In into ZnO facilitates the diffusion of Fe into ZnO at even faster rates (*210, 211*).

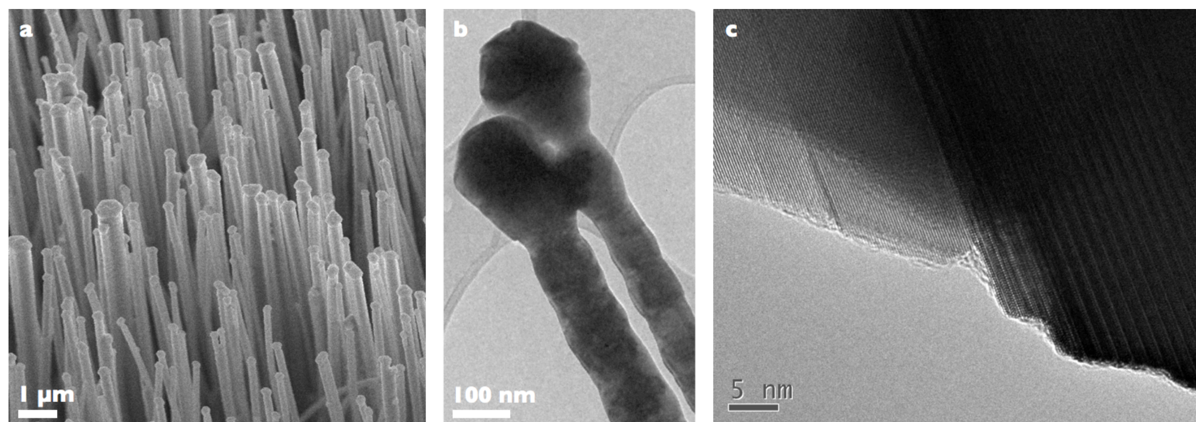

Figure 3.14: IFZO nanowire tips. a) SEM image of IFZO nanowires. **b**) TEM image of IFZO nanowire tips. **c**) HRTEM of the nanowire tip. The layered IFO phase is on the right and then $InFe_2O_4$ phase on the left.

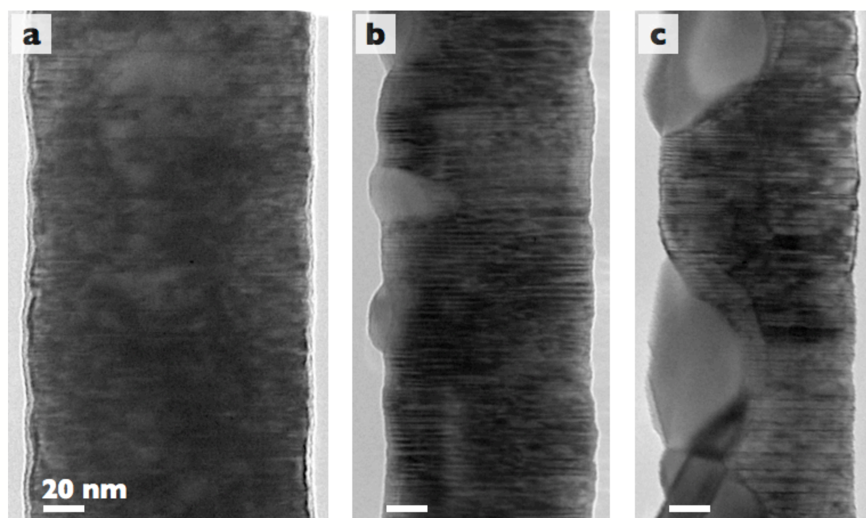

Figure 3.15: Varying In:Fe in IFZO. TEM images of IFZO prepared with varying In:Fe ratios. 1:1 20/10 IFZO (**a**), 1:2 20/20 IFZO (**b**), and 1:4 20/40 IFZO (**c**).

3.4.c. Structural analysis of IZO nanowires

Early preparations of IZO nanowires were performed without oxidation of the indium metal coating. These IZO samples did not exhibit a strong correlation between deposition thickness and inclusion density, especially above 15 nm of In (Figure 3.16). In 25 IZO, inclusions are especially irregular and large surface particles of In_2O_3 are formed (Figure 3.16d). These particles are routinely observed in all preparations of IZO at 900 °C and do not decrease with increasing reaction time. At this time, it was not possible to anneal at higher temperatures without significant decomposition. As the observed particles were far larger than the deposited metal films, it was suspected that indium metal (melting point = 157 °C) was melting and undergoing Ostwald ripening to form larger, unreactive droplets before eventually being oxidized. It remains unclear why a similar behavior is not observed in IGZO, in which indium and gallium can form a eutectic and melt at even lower temperatures.

In order to prevent the coating from melting and ripening, a plasma etcher was used to oxidize In^0 to In_2O_3 (melting point = 1910 °C). X-ray photoelectron spectroscopy measurements were collected to confirm the change in oxidation state (Figure 3.17a). The O 1*s* peak was observed in both samples due to ZnO. While a shift in the In $3d_{5/2}$ was not as large as previously reported for oxidation of In to In_2O_3 (+1.4 ± 0.2 eV), a positive shift was observed and the oxidized peak is in fair agreement with the reported value for In_2O_3 (444.9 eV) (*212*). The treatment did not have any discernible effect on the ZnO NWs by TEM analysis (Figure 3.17b-c).

With this simple additional step, more uniform IZO nanowires were prepared, even for 10 IZO (compare Figure 3.16b to Figure 3.17d). By repeating the deposition, oxidation, and annealing steps, compositions as high as 75 IZO were prepared. However, oxidizing the metal film did not improve annealing for thick indium oxide films and large indium droplets continue to suffer from low reactivity at 900 °C. New synthetic techniques for developed to prepare IZO at higher temperatures.

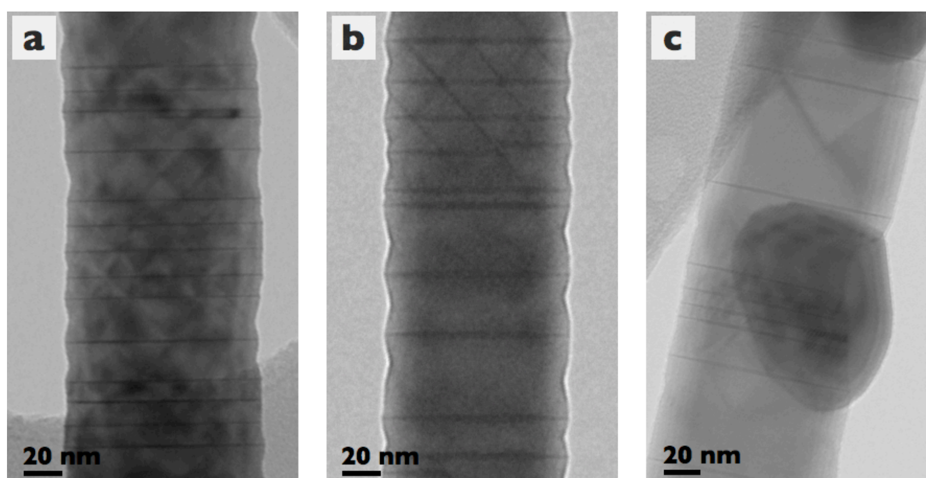

Figure 3.16: IZO nanowires. TEM images of IZO nanowires prepared from a 5- (**a**), 10- (**b**), and 15-nm (**c**) In^0 metal coating. The inclusions are relatively low and irregularly spaced in all preparations. Surface particles of In_2O_3 are commonly observed (**c**).

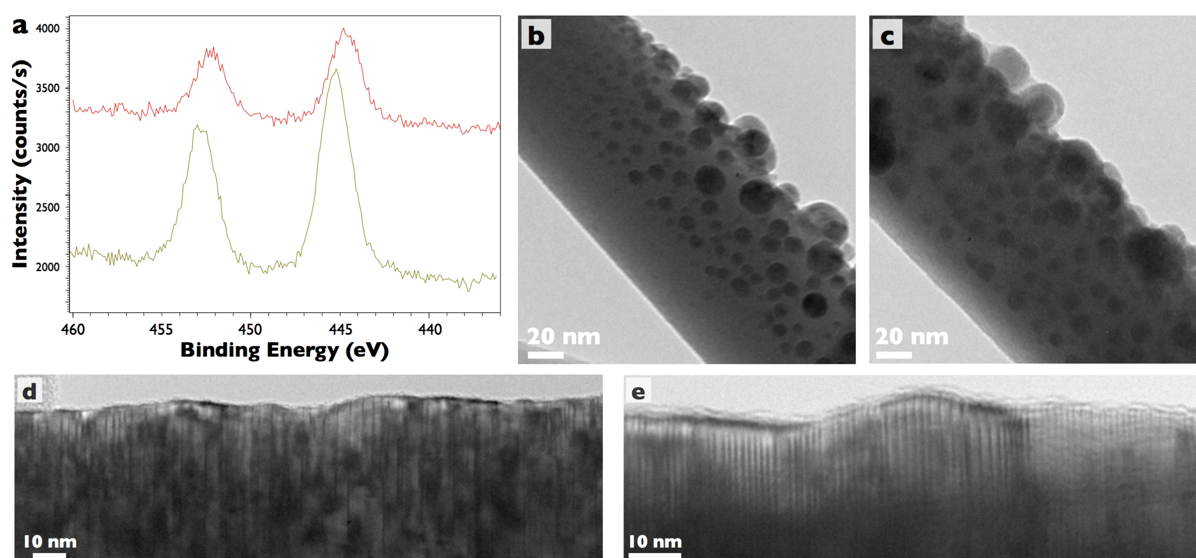

Figure 3.17: IZO nanowires prepared after metal oxidation. a) X-ray photoelectron spectroscopy spectrum of the indium metal coating on ZnO nanowires before (top) and after (bottom) oxygen plasma treatment. Literature reports that the In $3d_{5/2}$ peak in In_2O_3 is shifted +1 eV relative to In^0. **b-c**) TEM images of the In coating before (**b**) and after (**c**) oxidation treatment. **d-e**) TEM images of annealed 10 IZO (**d**) and 50 IZO (**e**) nanowires. The 50 IZO sample was deposited in 4 steps.

Sealed-tube annealing technique

ZnO stability is clearly improved by annealing in pure oxygen gas, but nanowire decomposition remains a problem in sparse arrays and single-nanowire samples. Additionally, increasing the annealing temperature might improve the reactivity of thick metal films, improve sample uniformity, and allow for new compositions, such as $Fe_2O_3(ZnO)_n$ or $ErRO_3(ZnO)_n$ nanowires,

that have yet to be prepared. Initially, it was believed that increasing the oxygen partial pressure alone was enough to limit decomposition and that increasing the pressure above one atmosphere during annealing might allow for annealing at higher temperature.

To achieve higher pressures, samples were sealed inside of a quartz tube filled with oxygen at 1 atm. In elevating the temperature to 1050 °C for annealing, the internal pressure is increased to 4.4 atm. An 8-inch long quartz tube (OD: 12.75 mm, ID: 10.5 mm) was prepared with one sealed end and a pinch point three inches from the sealed end. Metal coated substrates were loaded through the pinch point and a rubber septum was fitted over the open end of the quartz tube. The tube was purged with oxygen using a fully-inserted 8-inch syringe needle and a second short syringe needle inserted just inside the septum to allow venting. The tube was sealed at the pinch point by an oxymethane torch and then annealed.

Using these techniques, IZO and IGZO nanowires were successfully prepared using thick metal coatings that are unreactive under normal annealing conditions at 900 °C without oxidation or repeated deposition cycles. Sputtered-Au-grown ZnO nanowire arrays were prepared with 50 nm In and 40 nm In and 40 nm Ga, without plasma etcher treatment. After annealing at 900 °C (~3.9 atm) for 1 hour, the In-coated sample was unreacted and had formed surface In_2O_3 particles (Figure 3.18a). When the temperature was increased to 1050 °C (~4.4 atm, 1 hour), inclusions are formed in both IZO and IGZO (Figure 3.18b-c). However, all nanowires observed in TEM still showed signs of surface etching and were less than 4 μm long, likely due to the fragility of the nanowires and breakage during annealing or TEM grid preparation. SEM imaging shows significant damage in ZnO and IZO at 1050 °C, with malformed and fallen nanowires (Figure 3.19).

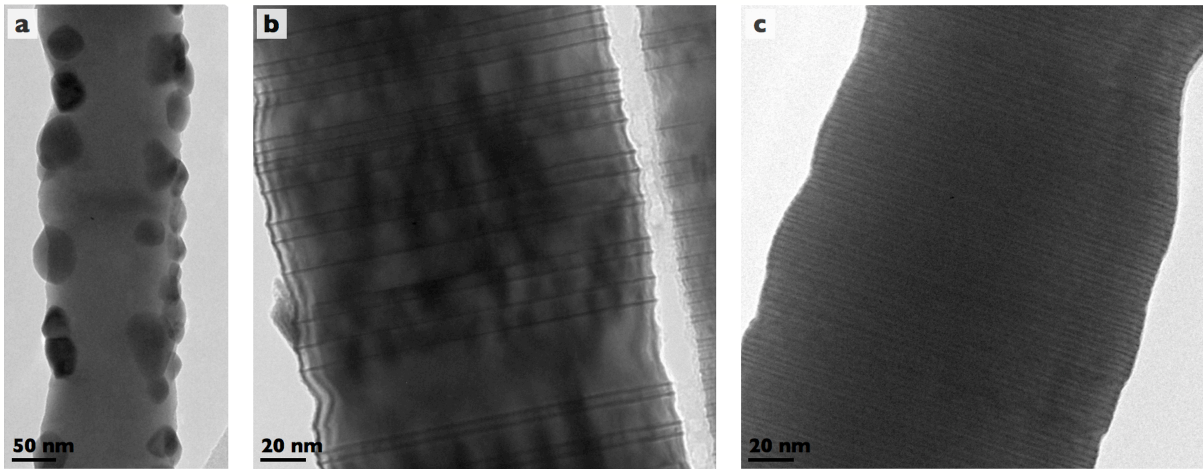

Figure 3.18: TEM of annealed nanowires by sealed-tube method. a) ZnO nanowire with 50 nm of In^0 annealed at 900 °C, ~3.9 atm, 1 hour. **b-c**) 50 IZO (**b**) and 40/40 IGZO (**c**) nanowires after annealing at 1050 °C, ~4.4 atm, 1 hour.

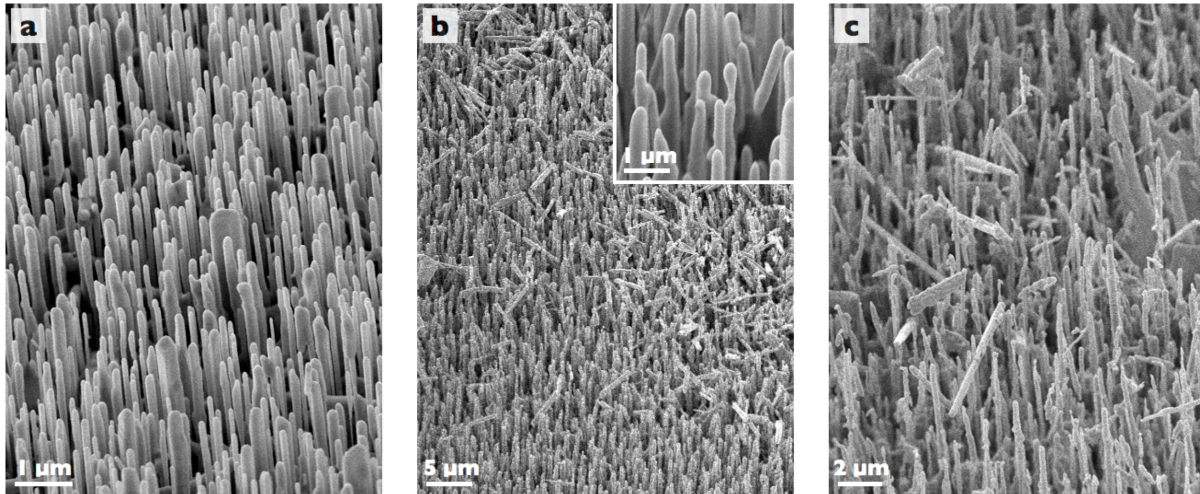

Figure 3.19: SEM of annealed nanowire arrays by sealed-tube method. **a**) ZnO nanowires annealed at 900 °C, ~3.9 atm, 1 hour. **b-c**) ZnO (**b**) and IZO (**c**) nanowires after annealing at 1050 °C, ~4.4 atm, 1 hour. Inset shows magnified view of individual nanowires.

"Sandwich" annealing technique

Following the partial success of the sealed-tube experiments, attempts were made at increasing the local concentration of ZnO vapor to decrease the decomposition rate. Initial attempts included annealing IZO substrates on a boat of ZnO powder (substrate face up and face down), but this did not yield any significant improvements. Inspired by an IGZO thin-film synthesis, the metal-coated ZnO substrate was covered with another ZnO nanowire substrate (*203*). This not only introduces a local ZnO vapor source but also limits diffusion allowing for the ZnO decomposition to equilibrate with ZnO vapor.

IZO nanowires were prepared from a sputtered-Au ZnO array and were coated with 50-nm In metal without oxidation. A second uncoated substrate of sputtered-Au ZnO nanowires were placed on top and annealed in pure oxygen at 1100 °C for 2 hours. The resulting nanowires were exceptionally stable against corrosion in this configuration and although the SEM shows a large number of unoriented nanowires disconnected from the substrate, the majority of the nanowires appear to be greater than 5 μm in length (Figure 3.20a). It is unclear if the loose nanowires are from the IZO substrate or the sacrificial substrate and whether than can be easily removed by sonication without damaging the IZO array. Few surface particles are observed, and minimal etching is observed (Figure 3.20b-c). Conjoined IZO nanowires are observed more frequently than in other IZO samples and often appear to be epitaxially matched and single-crystalline (Figure 3.20c). Additionally, the nanowires prepared at higher temperature are much more ordered, in terms of periodicity and zigzag structures, compared to IZO nanowires prepared at 900 °C. This technique offers a possible direction forward to higher-quality, single-composition IZO nanowires, especially if combined with a more uniform deposition technique.

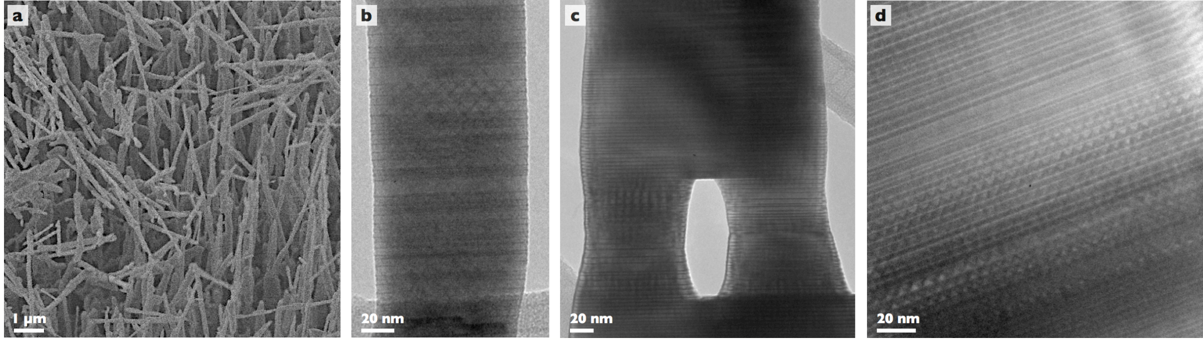

Figure 3.20: "Sandwich" Annealing of IZO. a) SEM image of nanowires prepared by annealing with a second ZnO nanowire substrate pressed against the ZnO/In^0 substrate. **b-d**) TEM images of prepared IZO nanowires, displaying no surface particles, low surface roughening, and high inclusion density.

3.4.d. Structural analysis of other MZO nanowire compositions

In addition to the indium-containing MZO compositions, attempts have been made at $Fe_2O_3(ZnO)_n$, $Y_2O_3(ZnO)_n$, $Er_2O_3(ZnO)_n$, and $ErRO_3(ZnO)_n$ nanowires using the conversion synthesis and electron-beam evaporated metal films. Unfortunately, inclusions have not been observed in any of these materials after annealing at 900 °C. Even brief reactions at 1075 °C have failed to turn up any partial inclusions in $Y_2O_3(ZnO)_n$. In all cases, we observe oxide particles on the ZnO nanowire surface after annealing (Figure 3.21).

While numerous other compositions of MZO materials have been prepared in the bulk phase, much higher temperatures are utilized over multiple day reactions. An incomplete list (arranged by temperature) of the various MZO elemental compositions and preparation conditions is compiled from literature in Table 3.1. Unsurprisingly, the indium-containing composi-

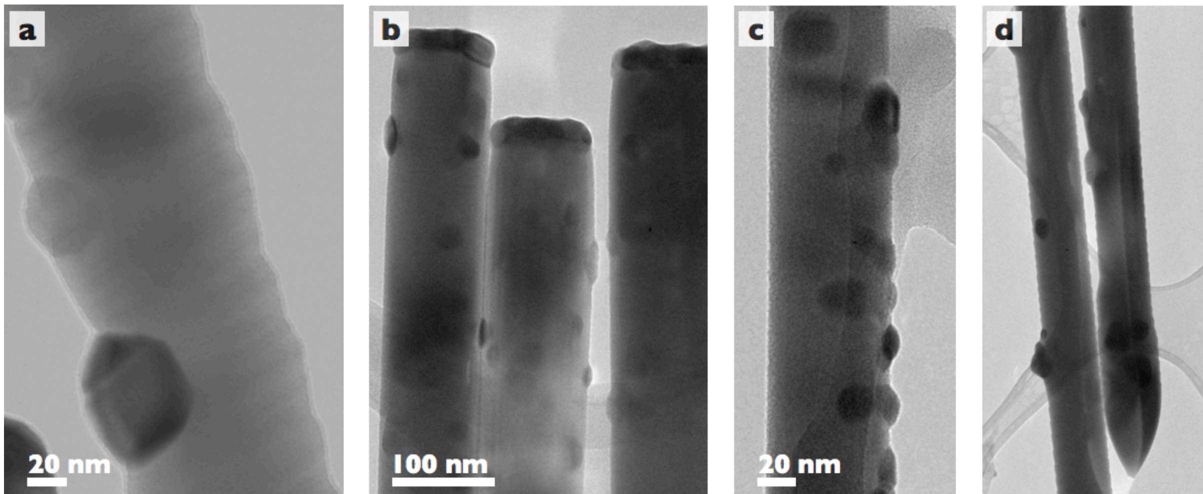

Figure 3.21: Non-indium-containing MZO nanowires. TEM images of unsuccessful attempts at other MZO compositions. These samples were prepared with 15 nm of Fe (**a**), 26 nm of Y (**b**), 25 nm of Er (**c**), and 12.5 nm of Er and 12.5 nm of Fe (**d**).

tions require the lowest necessary temperature, leading to their ease in nanowire preparation. MZO alloys prepared from heavier elements might provide even more thermoelectric benefit than materials prepared from lighter elements. The sandwich annealing technique may possibly make $Fe_2O_3(ZnO)n$ feasible, as this is the next lowest-temperature preparation after the indium-based MZO materials.

Table 3.1: Literature annealing conditions of various bulk MZO compositions.

Composition	Temperature (°C)	Time (days)	Ref.
$In_2O_3(ZnO)_4$	1100	3	(*180*)
$InFeO_3(ZnO)_{10}$	1150	7	(*182*)
$InGaO_3ZnO$	1150	7	(*184*)
$Fe_2O_3(ZnO)_{13}$	1300	7	(*191*)
$LuFeO_3ZnO$	1350	2	(*182*)
$LuGaO_3ZnO$	1350	3	(*182*)
$YbFeO_3ZnO$	1350	2	(*182*)
$YbGaO_3ZnO$	1350	1	(*182*)
$Ga_2O_3(ZnO)_9$	1350	11	(*184*)
$ErFeO_3(ZnO)_9$	1450	4	(*182*)
$ErGaO_3(ZnO)_4$	1450	4	(*182*)

3.5. Mechanism of conversion synthesis

The diffusion rates of In, Ga, and Zn within ZnO are extremely high at the 900 °C annealing temperature, with values of 6.62×10^{-12}, 1.09×10^{-14}, and 1.13×10^{-12} $cm^2 s^{-1}$, respectively (*213, 214*). DFT calculations show that Zn atoms diffuse through ZnO using Zn vacancies (*215*). Based on their activation energies for diffusion, In and Ga are also thought to diffuse through Zn vacancies, though some controversy exists regarding their true activation energies (*214, 216, 217*). One possible mechanism is that In and Ga diffuse into the nanowire, which strain and deform the wurtzite lattice of the pure ZnO. This strain is eventually relaxed by creating octahedral In/Ga inclusions and trigonal bipyramidal layers. However, this mechanism would likely produce perfectly spaced inclusion layers and an organized zigzag structure, which is not observed in nanowires prepared by the conversion chemistry technique.

Defects such as edge dislocations, stacking faults, and inversion domain boundaries are known to attract impurities and can assist in the formation of impurity inclusions (*218*). In some of the nanowires synthesized in this study, especially those made with lower amounts of In and Ga, partial inclusions were observed (Figure 3.22). The ends of these partial inclusions are usually associated with edge dislocations with the dislocation line lying at the leading edge of the MO_2^- plane (*190*). Edge dislocations can be seen in Figure 3.22b in the HR-STEM image of two

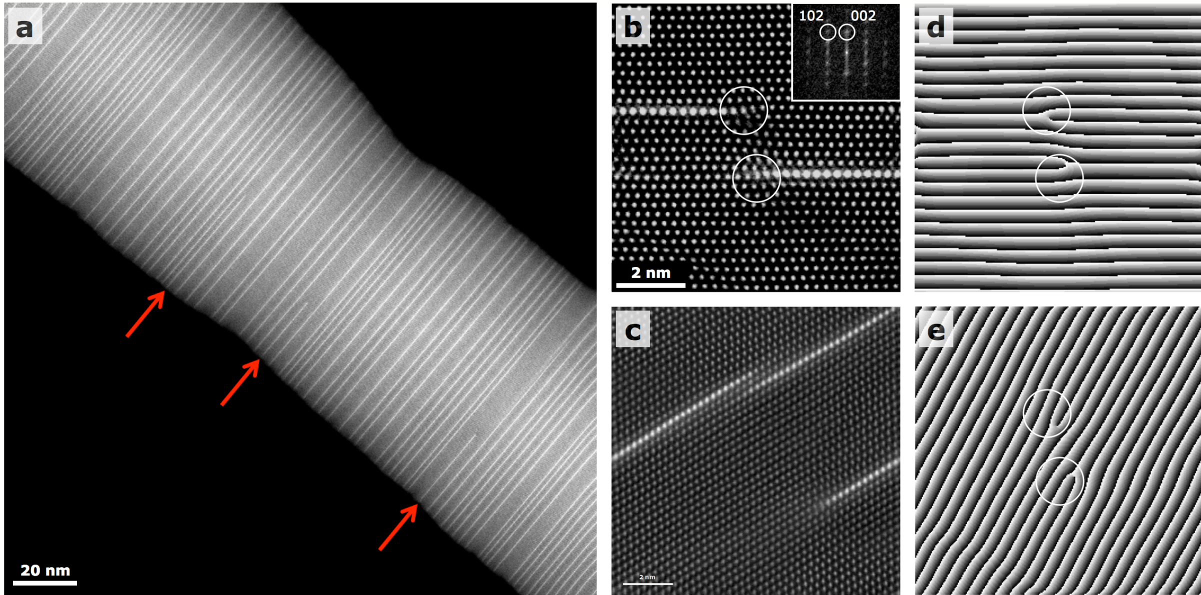

Figure 3.22: Edge dislocations at partial layers. **a**) Z-contrast STEM image of a 10/10 IGZO nanowire. The arrows indicate the presence of partial inclusions, all of which are connected to one side of the nanowire. **b**) HR-STEM image of IGZO oriented on the [010] zone axis with two incomplete MO_2^- layers and the corresponding FFT (inset). **c**) Z-contrast HR-STEM image of IGZO showing three partial inclusions. The two partial inclusions at the top of the image appear to be merging together via edge dislocation climb to create a single complete inclusion layer. **d-e**) Moiré images of the 002 (**d**) and 102 (**e**) reflections clearly showing the presence of edge dislocations at the end of each incomplete MO_2^- layer.

partial inclusions. Moiré images taken along the 002 and 102 reflections clearly show the presence of the edge dislocations. Partial inclusions are always connected to one surface of the nanowire (Figure 3.22a), indicating that the growth of the inclusion starts at the surface and proceeds across the diameter of the nanowire until it either reaches the opposite side or connects with an inclusion growing from the opposite side (Figure 3.22c).

If the inclusions are growing through a defect-assisted process and the inclusion formation begins at the nanowire surface, then the edge dislocation must somehow nucleate near the surface. One possible scenario is that the edge dislocations are formed on the nanowire surface via heterogeneous nucleation, which occurs with the help of defects such as impurity atoms. Since In has a larger radius compared to Zn, the dissolution of In within the wurtzite lattice will create strain. The presence of dislocations within the lattice can relax some of this strain if the In atoms diffuse towards the dislocations and eventually occupy those lattice positions below the edge dislocations where the lattice is already expanded. The edge dislocation basically creates a "hole" in which the larger In atoms can sit. Due to the high diffusion rate of In within the ZnO lattice, the In atoms can rapidly concentrate at the sites of edge dislocations. Since the In atoms have a mutual attraction they can crystallize into another phase (octahedrally coordinated MO_2^-) which will flow in one direction towards the dislocation. The growth of the inclusion will continue along the dislocation until the concentration of In within the lattice decreases to the point at which equilibrium is reached. In the lower concentration samples, more partial inclusions can be observed, likely resulting from insufficient quantities of In atoms necessary to complete the inclusions. In the 40/40 samples with higher concentrations of In, no partial inclusions were observed. Given that inclusion formation is driven by the inhomogenous presence of metal pre-

cursor at the surface, there is little order observed until very high metal loadings, when every possible inclusion position is occupied.

It is suspected that the defect-assisted octahedral layer formation causes local changes in the layer stacking but that a high activation energy limits the propagation of the reordering through the $MZn_nO_{n+1}^+$ slab. As a result, the second inversion to reorient the polarity in the slab layer is accomplished through random defects, rather than an ordered defect such as the modulated zigzag layer. In order to observe an organized zigzag structure, much higher annealing temperatures are necessary.

Since In and Ga are substitutional dopants, Zn atoms must diffuse out when the In and Ga atoms diffuse in. The Zn atoms diffuse to the surface of the nanowire, leading to a modulation in the diameter (Figure 3.22a). In areas of higher inclusion density, the diameter of the nanowire is slightly thicker (more In and Ga diffused in, more Zn diffused out) compared to areas of lower inclusion density. However, this can also be explained by etching of the ZnO nanowire at high temperature, which is inhibited by the presence of inclusion layers that act to increase the thermal stability of ZnO.

While the phase diagram for bulk IZO (Figure 3.1) covers the temperature ranges from 1100-1400 °C, several compositions of IZO and IGZO have been prepared in the bulk by annealing at 1050 °C by a simple solid state reaction of In_2O_3 and ZnO powders in air for 48 hours. However, no IZO or IGZO phases were observed by XRD for bulk powders annealing at 900 °C. On the other hand, the conversion synthesis for MZO nanowires has shown that solid state diffusion occurs spontaneously in ZnO nanowires at 900°C, given that the metal coatings are thin and particle ripening is prevented. This suggests that the thermodynamics of MZO formation at low temperature are made favorable by the surface energy contribution of ZnO nanowires and small metal and metal oxide surface particles. During annealing, free energy is reduced by the formation of the MZO structure or by the ripening of surface particles. Thus, the nanoscale metal thin films and droplets deposited by the evaporator are ideal for MZO formation, while thicker coatings and large surface particles have decreased or no reactivity.

A schematic illustration summarizing the surface processes in IZO formation is shown in Figure 3.23. Metal particles on the surface may be oxidized by the oxygen atmosphere at elevated temperatures, diffuse on the surface, ripen, and contribute to inclusion formation. As surface particles diffuse or are depleted, inclusions may be cut off from an indium source, resulting in partial inclusions. ZnO decomposition occurs increasingly rapidly at high temperatures resulting in surface faceting, but may stabilized by local Zn and O_2 vapor concentrations, as well as surface oxide particles and MZO inclusions. Small metal indium oxide particles readily contribute to IZO formation, while large particles and thick films are inactive at 900 °C (but increasingly reactive as temperature is increased to 1100 °C). Finally, ZnO counterdiffusion along inclusions to the surface may contribute to the faceted appearance of annealed nanowires.

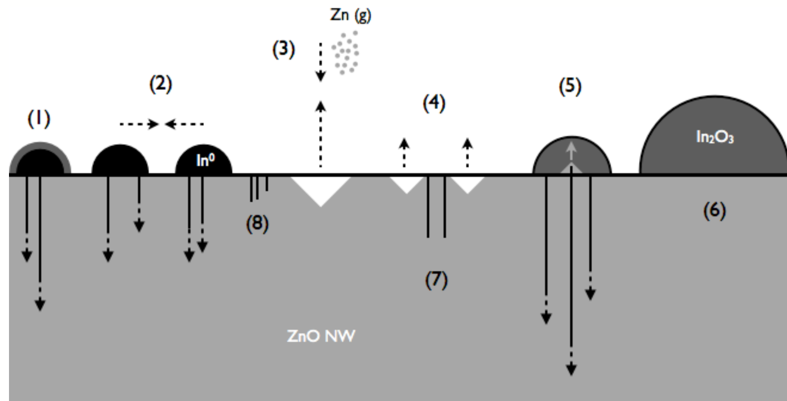

Figure 3.23: Schematic diagram of the ZnO nanowire surface in IZO formation. ZnO is indicated by light gray, In_2O_3 by dark gray, and In^0 by black. Inclusions are represented by solid lines. Dotted lines inclusion diffusion. (1) Liquid In^0 particle is oxidized by high-temperature and oxygen atmosphere. (2) Liquid In^0 diffuse across surface and ripen into large particles. (3) ZnO NW is thermally unstable and vaporizes, but the decomposition is in equilibrium with the local Zn vapor concentration. (4) Inclusions lend stability to ZnO, limited etching in areas of high inclusion density. (5) ZnO counterdiffusion into the surface particles is suspected. (6) Large In_2O_3 particle is inactive at 900 °C and no inclusions are formed. (7) Partial inclusions that have depleted the indium source on the surface. (8) Partial inclusions that have been cut off from an indium source due to particle diffusion (2).

3.6. Optical Properties

The absorption and PL emission properties of indium zinc oxide have been well reported, especially in the nanowire literature, but remains largely unknown for IGZO, IFZO, and other compositions (*196, 205*). Kudo and Mikami report a large shift in the absorbance onset (as measured by diffuse reflectance) from from 385 in ZnO to 480 nm in bulk IZO_3 powder, which they attribute to an intrinsic band transition given the steep onset and no apparent shoulder features (*196*). However, PL studies of IZO, IGZO and $InAlO_3(ZnO)_n$ nanowires, observe band-edge PL emission at 3.20 eV, compared to 3.28 eV in ZnO, suggesting that the mechanism of absorption is not due to a change in band gap, but rather from defect states (*205, 206, 219*). Given the 17% local lattice strain observed around the inclusion layer in IGZO nanowires (Figure 3.11d), it is reasonable to believe that both mechanisms have a role in the observed shift.

Bulk samples of IZO, IGZO, and IFZO were prepared by solid state reaction at 1100 °C. The absorption spectra was measured in an integrating-sphere-equipped UV/Vis spectrometer, which allowed for the collection of both transmission and diffuse reflection (Figure 3.24). $IGZO_3$ showed a minimal shift in absorption compared to ZnO (410 nm vs. 388 nm). IZO_5, which appears bright yellow, has an absorption onset of 465 nm. $IFZO_3$ has two shoulders and an absorption tail that extends out to 600 nm (it was determined to be free of contamination by XRD). Assuming that the band gap is modified by lattice strain within the slab layer, it is reasonable that IZO has a larger shift than IGZO, given the ionic radii. As the ionic radius of iron is intermediate of gallium and indium, we would expect the band gap of IFZO to be intermediate of IGZO and IZO, which is observed near the IFZO peak when the shoulders are ignored. These two extra features in IFZO are likely due to the strong visible transitions associ-

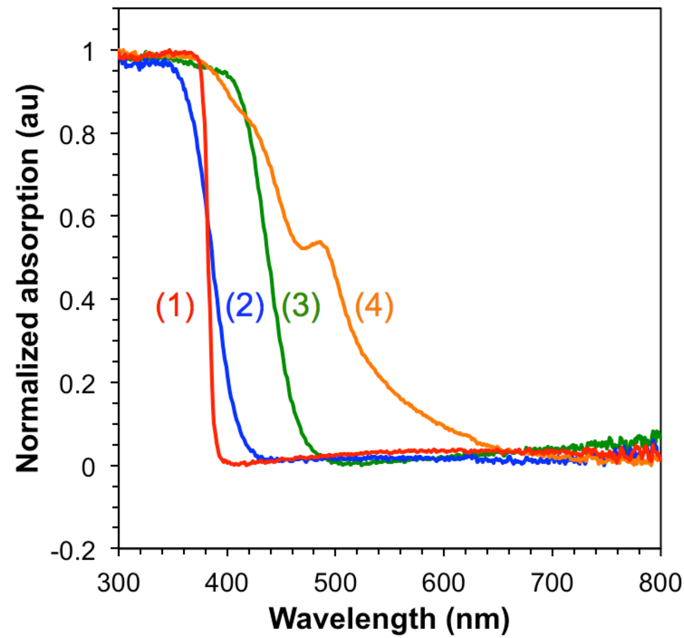

Figure 3.24: UV-visible absorption spectra of ZnO and MZO bulk powders. Spectra was collected using an integrating sphere to account for scattering and reflection. In order of onset is ZnO (1), 388 nm, $IGZO_3$ (2), 410 nm, IZO_5 (3), 465 nm, and $IFZO_3$ (4), 600 nm.

ated with iron and perhaps metal-metal charge transfer. The PL emission of the bulk powders was tested to gain more insight on the change in band gap of the different species, but no band-edge emission was observed from the IZO and IGZO samples when illuminated with a 325 nm laser. IFZO had no emission at all, suggesting a high concentration of non-radiative trap states.

The absorption and emission properties of MZO nanowire arrays prepared with the conversion synthesis were also studied. The 40/40 IGZO nanowire array behaves very similarly to bulk IGZO, shifting to an absorption onset of 410 nm with a loss in the sharpness of the curve (Figure 3.25a). The IZO and IFZO nanowire arrays were much lower performing than their bulk counterparts (Figure 3.25b), with onsets of 420 and 500 nm, respectively, although these spectra are difficult to interpret due to the strong scattering of visible light due to the nanowire array (reflection data was unavailable to account for scattering). While the initial ZnO nanowire arrays had strong band edge emission, this was lost after conversion and no significant band-edge emission was observed in IZO and IGZO (Figure 3.25c). In both cases, a broad defect emission band was centered at 540 nm, which may possibly be related to the normally observed *green* emission in ZnO (at 506 nm in the initial ZnO arrays here).

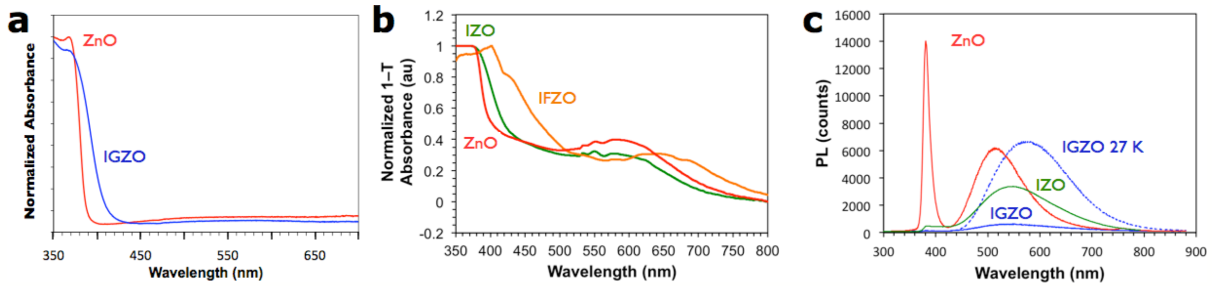

Figure 3.25: UV-visible absorption and PL spectra of ZnO and MZO nanowire arrays. **a**) Integrating sphere absorbance spectra of ZnO (red) and 40/40 IGZO (blue) nanowires. **b**) Absorbance (1 – T) spectra of ZnO (red) 50 IZO (green), and 70/35 IFZO (orange) nanowires. The high background across the visible spectrum is due to scattering by the nanowire array. **c**) PL spectra of ZnO, 40/40 IGZO, and 50 IZO. The initial ZnO NWs have strong band-edge PL emission, but this is lost after conversion to IGZO, which only emits defect PL. Even at 27 K (dotted line), only defect emission is observed.

3.7. Transport properties

The presence of the MO_2^- inclusions alters both the thermal and electrical properties in the converted IGZO nanowires. While ZnO can exhibit relatively high intrinsic electrical conductivity due to formation of oxygen vacancies acting as donor states, the introduction of slight amounts of Al, In, or Ga can further increase the conductivity when substituted for Zn (*164*). Electrical devices were made by either drop-casting or micro-manipulating nanowires onto a Si chip with 200 nm of thermal oxide on the surface. The nanowires were top-contacted using metallic contacts defined by standard photolithography techniques. Ti/Au was used as the contact and Ohmic contact was achieved after rapid thermal annealing (*155*). Seebeck coefficients were determined by measuring the thermal voltage induced by passing current through a heating coil near the nanowire. The contacts where used as resistive thermometers to measure the temperature difference across the nanowire. Thermal transport in individual nanowires was accomplished using pre-fabricated MEMS devices, upon which single nanowires were physically manipulated using thin tungsten probe tips. Full descriptions of the measurement scheme can be found in reference (*220*).

The increased electrical conductivity observed at room temperature in the IGZO nanowires when compared to the ZnO nanowires is consistent with that of a slightly doped semiconductor (Figure 3.26a). However, considering the relatively large amount of In and Ga incorporation (greater than 2% atomic of metal atoms each from EDS), the observed increase in conductivity is smaller than expected. While the In and Ga impurities can act as electrical dopants in ZnO when substituted for tetrahedrally-coordinated Zn, In and Ga also sit in the trigonal bipyramidal sites, helping to preserve electroneutrality and reducing the number of generated carriers. Moreover, the MO_2^- inclusions can act as barriers to oxygen diffusion leading to decreased conductivity by suppressing the formation of oxygen vacancies (*221*). Interestingly, the linear temperature-dependent resistance of IGZO, as seen in Figure 3.26a, is not typical behaviour for a slightly doped semiconductor (of which pure ZnO nanowires are an example) nor of a degenerately doped semiconductor (which should give metallic behaviour). This deviation from the classical semiconducting behaviour indicates a departure from the typical ther-

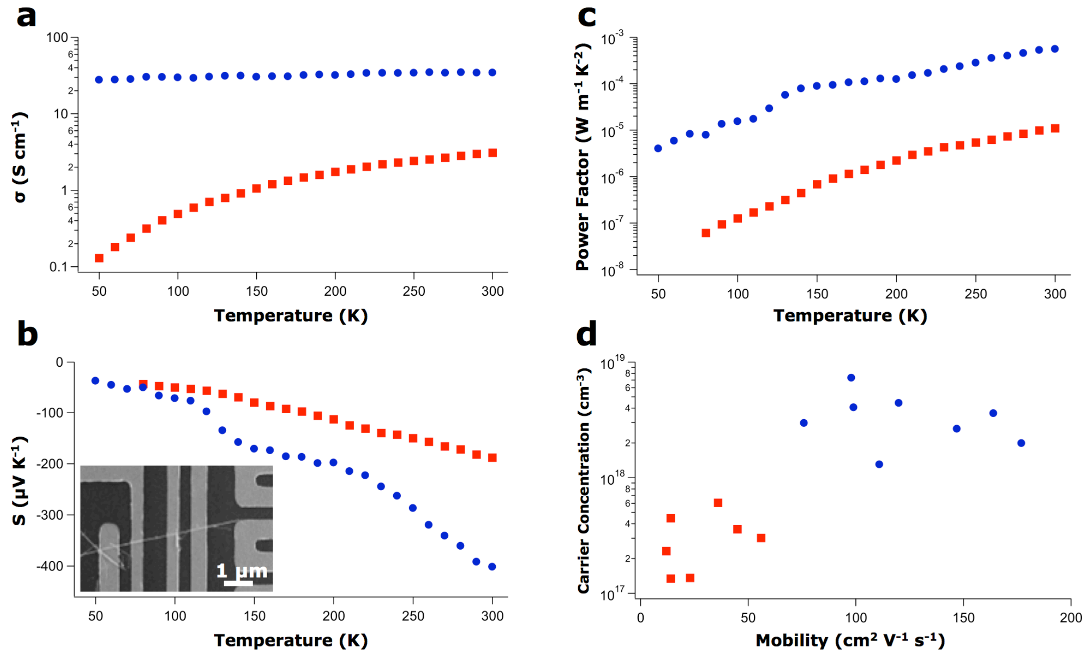

Figure 3.26: Single-nanowire electrical measurements. a) Electrical conductivity as a function of temperature for a 120-nm diameter 5/5 IGZO nanowire (blue circles) and a 110-nm diameter ZnO nanowire (red squares). **b-c**) Seebeck coefficient (**b**) and power factor (**c**) as a function of temperature measured for the same nanowires in (**a**). Inset shows a SEM of an individual nanowire in a four-point FET/Seebeck device. **d**) Carrier concentration as a function of mobility, as measured from the FET geometry. No diameter dependence was observed for ZnO or IGZO nanowires in the range of 75–130 nm.

mally-activated mechanism. The octahedral layers could be acting as potential barriers to electron diffusion, leading to alternative transport mechanisms such as pseudo variable-range hopping or percolation conduction (*222*).

The presence of the inclusion layers also has an effect on the Seebeck voltage (Figure 3.26b). At 300 K, the Seebeck coefficient grew in magnitude from –188 μV K^{-1} in ZnO nanowires to –402 μV K^{-1} in IGZO nanowires. This increase may be an effect of the potential barriers, which could act as low-energy electron filters (*223*). When a temperature gradient is applied, charges diffuse to states of lower chemical potential. While most of these states are on the colder side, unoccupied states on the hotter side allow for charge diffusion in the opposing direction, thereby limiting the overall potential that can develop for a given temperature gradient. Charges that participate in back diffusion are referred to as "cold electrons" (for n-type semiconductors) since they posses lower carrier energy. However, potential barriers with appropriate energy levels can act as low energy charge filters by preferentially affecting their mobility (*224*). By limiting the amount of back diffusion, a larger potential can develop, resulting in an increased Seebeck coefficient.

Aside from filtering, the possibility exists that electronic quantum confinement caused by closely spaced inclusion layers contributes to the rise in Seebeck values (*49*). Since ℓ values of less than 2.34 nm (exciton Bohr radius of ZnO) were observed, thermopower enhancement might be due to slight changes in the density of states near the Fermi level (*225*). While difficult to quantify at this time, the random nature of the single crystalline, polytypoid nanowires per-

haps plays a role in these and other transport phenomena. Further theoretical and experimental investigations are required in order to paint a clearer picture of this general nanowire system.

Regardless of the source of enhancement, when increases from both the electrical conductivity and the Seebeck coefficient are combined, the resulting power factor ($S^2\sigma$) for the IGZO nanowires is 0.6 mW m^{-1} K^{-2}, which is 58 times larger than that for pure ZnO nanowires and approximately 6 times greater than the highest reported bulk IZO value at 500 K (Figure 3.26c) (*226*).

To ensure that the observed Seebeck enhancement is not due to mere increases in impurity scattering, FET mobilities were measured on the same nanowires from which the electrical conductivity and Seebeck coefficient were determined (Figure 3.26d). Both carrier concentration and mobility enhancements were observed when compared to the pure ZnO nanowires. This indicates that the carrier concentration, and not the mobility, is the limiting factor in the electrical conductivity, contrary to what may have been suspected based on the defects that accompany each MO_2^- layer. Furthermore, 177 cm^2 V^{-1} s^{-1} at 300 K is more than twice the field effect mobility value previously measured in single crystalline IGZO thin films (*221*). The nature of the mobility enhancement in the polytypoid IGZO nanowires over IGZO thin films is not fully understood. However, the enhancement over the single crystalline ZnO nanowires may be explained by the induced strain at the MO_2^- layer interfaces. It is well established that piezoresistive materials, both crystalline and amorphous, demonstrate mobility changes with the application of stress (*227, 228*). As seen in Figure 3.11d, the 17% difference in the *d* spacing at the octahedral/wurtzite interface produces a significant amount of strain. Although the inclusions are perpendicular to the transport direction, the mobility could be enhanced by possible strain-induced changes to the electronic band structure. Further theoretical and experimental work is necessary to determine the extent to which strain plays a role in this polytypoid system.

Not only do the nanostructured features influence the electronic properties, but they also act as important phonon scattering interfaces, thereby limiting the lattice thermal conductivity (*229*). Compared to literature values for the bulk material, ZnO nanowires demonstrate up to five-fold reduction of thermal conductivity at room temperature (Figure 3.27b) (*230*). An estimation of the average phonon mean free path as a function of temperature shows that the limiting factor is the nanowire diameter until the 150–200 K range, where other scattering mechanisms, such as impurity and umklapp scattering, begin to limit the conductivity. As seen in Figure 3.27b, the linear segment of the ZnO nanowire plot begins to plateau around that temperature range. The IGZO nanowires, on the other hand, show no such plateau, indicating that the MO_2^- layers are limiting the average phonon mean free path throughout the measured temperature range. At 300 K, IGZO nanowires exhibit a thermal conductivity of 3.3 W m^{-1} K^{-1}, which is only slightly lower than what has been observed for IZO (n = 3,4) in the bulk (*202*). However, since bulk IZO has both higher inclusion density and periodicity, it is surprising that the more disordered 5/5 IGZO nanowires exhibit comparable thermal transport properties. While higher inclusion densities are expected to limit the average phonon mean free path, the disordered nature of the polytypoid IGZO structure combined with the nanowire geometry produces similar effects on overall thermal energy propagation, as seen in other systems (*231*).

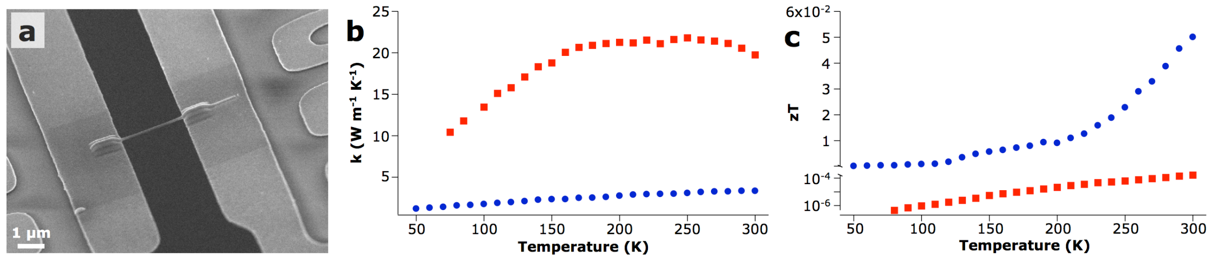

Figure 3.27: Thermoelectric measurements. a) SEM of an individual 5/5 IGZO nanowire bridging two suspended membranes on a prefabricated MEMS device used for thermal conductivity measurements. **b**) Thermal conductivity as a function of temperature for both a 120-nm 5/5 IGZO nanowire and a 90-nm ZnO nanowire. **c**) Figure of merit, *zT*, of 5/5 IGZO nanowires compared with ZnO nanowires showing an enhancement of 2.5 orders of magnitude after alloying.

As a direct result of the enhancements from all three thermoelectric parameters, *zT* was increased from 1.7×10^{-4} for ZnO nanowires to 0.055 for the IGZO nanowires at 300 K, an enhancement of 2.5 orders of magnitude (Figure 3.27c) (*202, 232*). Such *zT* values represent a factor of ~10 enhancement when compared to the bulk IZO superlattice samples. It is worth noting that oxide-based thermoelectric modules are typically employed at elevated temperatures (700-1000 K) in actual application, where further power factor enhancements are expected.

4. Titanium oxide-ilmenite nanowires

In another demonstration of conversion chemistry, an easily scaleable solid state preparation is used to react rutile (TiO_2) nanowires with transition metals to form ilmenite-structured ternary metal oxides. Given the epitaxial match between rutile and ilmenite, the nanowire geometry is maintained through the conversion process despite a change in crystal structure. By controlling the extent of the reaction, different rutile-ilmenite heterostructures are prepared for $CoTiO_3$, $NiTiO_3$, $MnTiO_3$, and $Co_{0.5}Ni_{0.5}TiO_3$. Ilmenite materials have greatly enhanced visible light absorbance and are potentially useful photoanode materials for photoelectrochemical water photolysis.

4.1. Introduction

Since the first demonstration of water photolysis by the Honda-Fujishima with the rutile-phase of titanium oxide (*65*), TiO_2 and ternary titanates have been one of the most researched semiconductor materials. While rutile is photostable and abundant, it is a large band gap material (E_g = 3.0 eV) and cannot efficiently utilize the solar spectrum, nor does it have a proper band alignment for photolysis at pH 7. While other materials have been demonstrated for overall water splitting, rutile is still one of the most common photoanode materials for tandem water photolysis schemes when combined with an appropriate photocathode such as silicon or indium phosphide. There are many reports of doping and other modifications to increase the visible absorption of rutile, as well as to reduce the overpotential requirements without relying on expensive platinum metal.

There are two major groups of $A\mathrm{TiO}_3$ structured titanates: perovskites and ilmenite. While perovskite forms when r_A and r_{Ti} are highly mismatched, ilmenite (A = Mn, Fe, Co, Ni, Mg) forms an ordered corundum structure with alternating layers of AO_6 and TiO_6 octahedra when r_A is similar to r_{Ti} (Figure 4.1). The ilmenite family have the smallest band gaps among ternary titanates: 2.4 eV in $MnTiO_3$ and $CoTiO_3$, 2.5 eV in $FeTiO_3$, and 2.8 in $NiTiO_3$ (*233*). Flat-band measurements have shown that the reduction in band gap is at the expense of the CB position, indicating that these materials are less useful for overall water photolysis than rutile. Additionally, the ilmenite family suffers from a number of material properties that make them ill-suited as photoanode materials. All of the ilmenite materials were determined to have low or no photocurrent due to both low quantum efficiency and high electrical resistivity. The inherent $O^{2-} \rightarrow Ti^{4+}$ transition occurs at ~3.7 eV for all ilmenite structures, while the visible absorption increase is due to the $A^{2+} \rightarrow Ti^{4+}$ charge transfer (*234*). However, the geometry of the ilmenite crystal structure in $NiTiO_3$ leads to low oscillator strength for $Ni^{2+} \rightarrow Ti^{4+}$, which is probably general to the other ilmenites. While holes generated in $NiTiO_3$ are thought to reach the surface, they tend to lead to photocorrosition rather than water oxidation because the Ni^{3+} intermediate

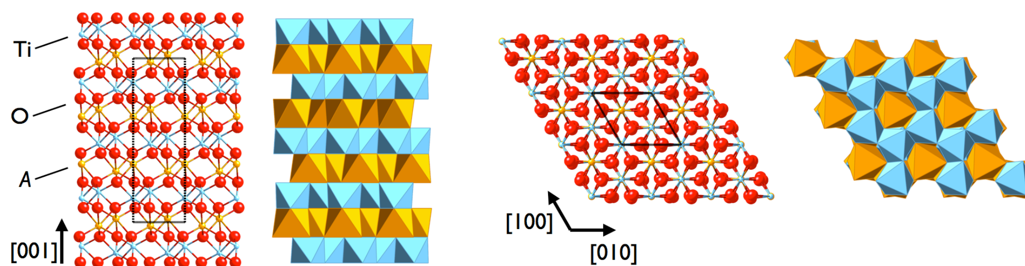

Figure 4.1: Ilmenite crystal structure. Atomic and polyhedra structure models of ilmenite, $ATiO_3$, along the *a* and *c* directions. Titanium cations and polyhedra are indicated by blue, *A* cations and polyhedra are indicated by yellow and oxygen anions in red.

is not positioned correctly to oxidize water (*234, 235*). Similar stability problems have been observed in $FeTiO_3$ (*236*), while no photocurrent has been observed in $MnTiO_3$ (*237*) and $CoTiO_3$ (*237, 238*). Oxygen evolution rates for $NiTiO_3$ and $CoTiO_3$ during illumination in a $KBrO_3$ sacrificial reagent solution were measured and found to be an order of magnitude less than rutile, anatase, and perovskite titanates under the same conditions (*239*).

Given the water oxidation catalytic activity of manganese oxides and cobalt oxides and their similarity to the Mn_3CaO_4-cubane structure believed to be the basis for photosynthetic water oxidation (*240*), these ilmenite materials may be useful as electrocatalysts and co-catalysts for water oxidation (*241-243*). Garcia-Mota et al. used DFT calculations to determine the optimal relationship between surface binding energies of OER intermediates in doped rutile materials (*241*). The study predicted that that activity of 6% doping of Cr, Mn, or Mo- in rutile TiO_2 may have activities similar to RuO_2, one of the best OER catalysts. The improved activity of the doped rutile nanowires as predicted by DFT has been observed experimentally (*244*).

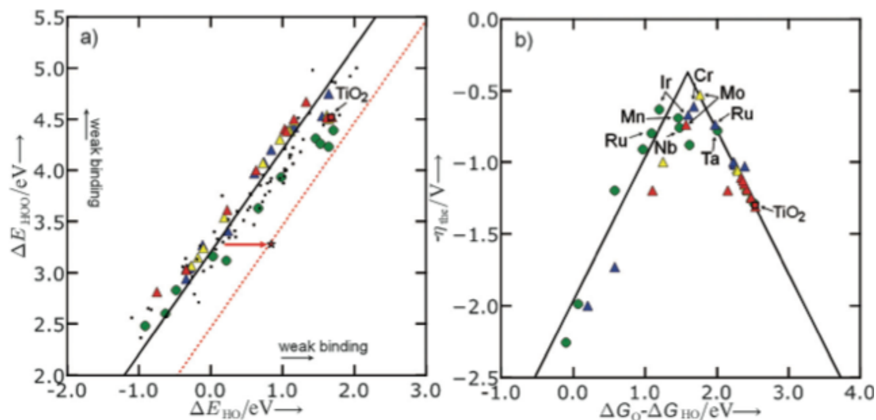

Figure 4.2: Computational study of OER activity for doped rutile materials. a) Adsorption energies of HOO* as a function of the adsorption energy of HO* on the surfaces of $MTi_{15}O_{32}$ (*M*=V, Nb, Ta, Cr, Mo, W, Mn, Fe, Ru, Ir, Ni, colored points). The small black circles correspond to DEHOO as a function of DEHO on pure oxides. The red star indicates where the binding energies need to be for an ideal electrocatalyst. **b**) Calculated theoretical overpotentials plotted as a function of ΔG_{O*}–ΔG_{HO*} for $MTi_{15}O_{32}$. The volcano curve is established by using the scaling relation between ΔG_{HOO*}–ΔG_{O*} and ΔG_{O*}–ΔG_{HO*}. Green circles stand for configurations in which the dopant is five-fold coordinated. Triangles stand for configurations in which the dopant is six-fold-coordinated: 6c-M (blue), 6c-Ms1 (red), and 6c-Ms2 (yellow). This image was adapted from reference (*241*).

Following the conversion technique proposed in Chapter 3, a similar synthetic technique was devised for ilmenite nanowires. First, rutile nanowires were prepared using a gram-scale molten salt flux synthesis. Second, a metal coating of $A(OH)_2$ was deposited on the prepared nanowires using a chemical bath deposition (CBD) method. This method can potentially be scaled up to gram scale deposition, but can be substituted with other techniques for depositing a metal (A^0) or metal salt (A^{2+}) coating. Finally, the core-shell nanowires are annealed at high temperature, typically 825 °C, for 0.5–4 hours. In varying the shell thickness and annealing conditions, it is possible to produce $ATiO_3$-decorated r-TiO_2 nanowires, $ATiO_3$–r-TiO_2 segmented nanowires, and fully converted $ATiO_3$ nanowires. This conversion chemistry method has been demonstrated to prepare $CoTiO_3$ (CTO), $NiTiO_3$ (NTO), and $MnTiO_3$ (MTO).

4.2. Synthesis of rutile-ilmenite nanowires

Rutile nanowires were synthesized using a high-temperature molten salt flux synthesis. TiO_2 nanoparticles (Degussa P25, 70% a-TiO_2, 25% r-TiO_2, average diameter 25 nm), disodium hydrogen phosphate (Na_2HPO_4), and sodium chloride were mixed in a mortar and pestle in a 1:1:4 ratio by weight (*244, 245*). The mixture was transferred to an alumina crucible and annealed in air at 825 °C for 8 hours. The resulting mixture was boiled in Millipore-filtered deionized water for 1-2 hours until all large chunks had dissolved into a suspended nanowires and dissolved salts. After centrifugation, the water and excess salt were decanted. Nanowires were washed with 1 M HCl acid, rinsed with water, and dried. The resulting nanowires grew in the <001> direction and averaged ~100 nm in diameter and no evidence of anatase, NaCl, or phosphorous compounds were observed in XRD.

The metal coating was deposited by a chemical bath deposition technique for $Co(OH)_2$, $Ni(OH)_2$, and $Mn(OH)_2$. No suitable chemistry was found for the deposition of Fe^{2+} films, but $Fe(OH)_3$ can be deposited using the same chemistry (attempts to reduce it to Fe^{2+} afterwards failed). For $CoTiO_3$-decorated r-TiO_2 nanowires, a solution of 0.25 M $Co(NO_3)_2$ and 0.1 M urea was used for the chemical bath. For completely converted $CoTiO_3$ nanowires, the concentrations were increased as high as 0.5 M $Co(NO_3)_2$ and 0.75 M urea. The necessary $A(OH)_2$ concentrations for equivalent depositions of $Ni(OH)_2$ and $Mn(OH)_2$ are approximately 1/2 and 1/5 of $Co(NO_3)_2$, respectively, with no changes to urea concentration. In a glass scintillation vial, 10 mL of growth solution was used for every 5 mg of r-TiO_2 nanowires. The reaction was carried out at 90 °C on a hot plate for 1.5–3 hours, and then hot filtered through 0.5 μm filter paper. All three metal hydroxides could be decomposed to their metal (II) oxides by annealing at ~350 °C in inert atmospheres, but this was not necessary prior to high-temperature annealing.

The high-temperature annealing for solid-state conversion was performed in a tube furnace under argon atmosphere to prevent oxidation of the metal species. The metal-coated nanowires were dropcasted onto a quartz slide in a thick film and placed in the center of the tube furnace. To form *A*TiO3 surface particles, 5 minutes of annealing at 825 °C was sufficient. For segmented and fully converted nanowires, the samples were annealed at 900 °C for 1-4 hours with ramp rates of ~15 °C/min. The nanowires were redispersed in DI water or spectroscopic-grade isopropanol using an ultrasonicator. For short annealing times, a 3-foot long quartz tube was used (for a 2-foot-wide furnace) with the sample placed in the tube but just out-

side of the furnace. After sufficient time for the tube to purge and the furnace to ramp up to temperature, the excess quartz tube was slid into the furnace until the sample was positioned in the center of the furnace. The system generally equilibrated after 60 seconds, rather than the ~10 minutes needed for the furnace to ramp from room temperature to 825 °C.

4.3. Structural analysis of rutile-ilmenite nanowires

The r-TiO_2 synthesis produced phase-pure nanowires with average dimensions of 100 nm diameter and 10 μm length. The chemical bath deposition for $Co(OH)_2$, $Ni(OH)_2$, and $Mn(OH)_2$ formed free particles in solution as well as coatings or attached particles on the nanowires: $Co(OH)_2$ tends to form lamellar structures, $Ni(OH)_2$ tends to form sheet structures, and $Mn(OH)_2$ tends to forms particles (Figure 4.3). There was no any observable changes or damage to the r-TiO_2 by TEM. The coating morphology was unchanged for thick depositions of $Co(OH)_2$ and $Ni(OH)_2$, but attempts to increase the $Mn(OH)_2$ coating instead resulted in large 0.3-1 μm particles.

Annealing the core-shell nanowires at 825 °C for 5 minutes tended to produce CTO particles on the nanowire surface, which were visible in nearly all nanowires within a given sample. The particle dimensions varied widely depending on both the CBD parameters and local variation, but were typically 20-50 nm deep, 20–60 nm wide, and 80-100 nm long (Figure 4.4a). The formation of the ternary phase was confirmed by EDS measurements of the surface particles, which were approximately 1:1 *A*:Ti by peak area (as calculated by EDAX Genesis software) while the *A* peak was undetectable or insignificant in regions of the nanowires without obvious particle formation (Figure 4.4d). X-ray diffraction was used to characterize dispersed nanowire films and also confirmed the incomplete conversion of rutile TiO_2 to $ATiO_3$ (Figure 4.4e). All $ATiO_3$ species have the same diffraction pattern, but the lattice parameters decrease for Mn>Co>Ni, in agreement with the periodic trends for ionic radius.

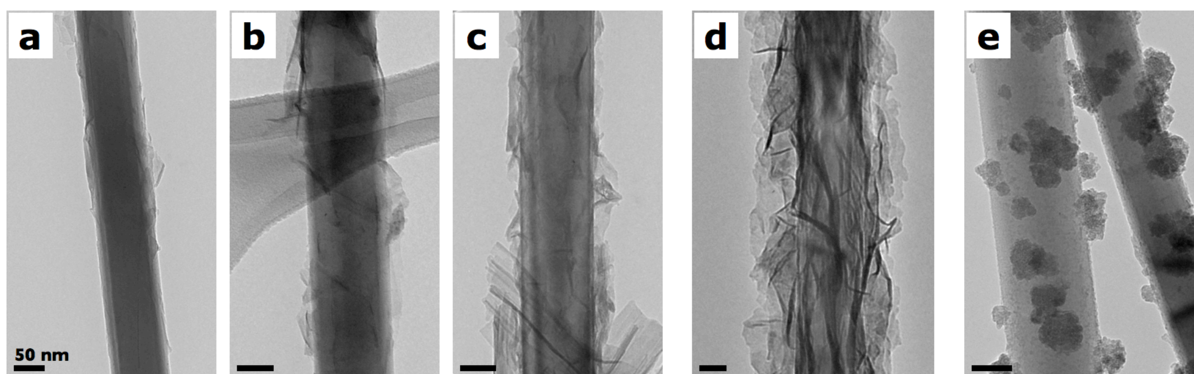

Figure 4.3: Chemical bath deposition of metal hydroxide coatings. a-e) TEM images of rutile nanowires coated with $Co(OH)_2$ (**a-c**), $Ni(OH)_2$ (**d**), and $Mn(OH)_2$ (**e**). The thickness of the $Co(OH)_2$ is primarily controlled by adjusting the precursor concentrations. 0.25 M $Co(NO_3)_2$ and 0.1 M urea was used in (**a**) and 0.5 M $Co(NO_3)_2$ and 0.75 M urea was used in (**c**).

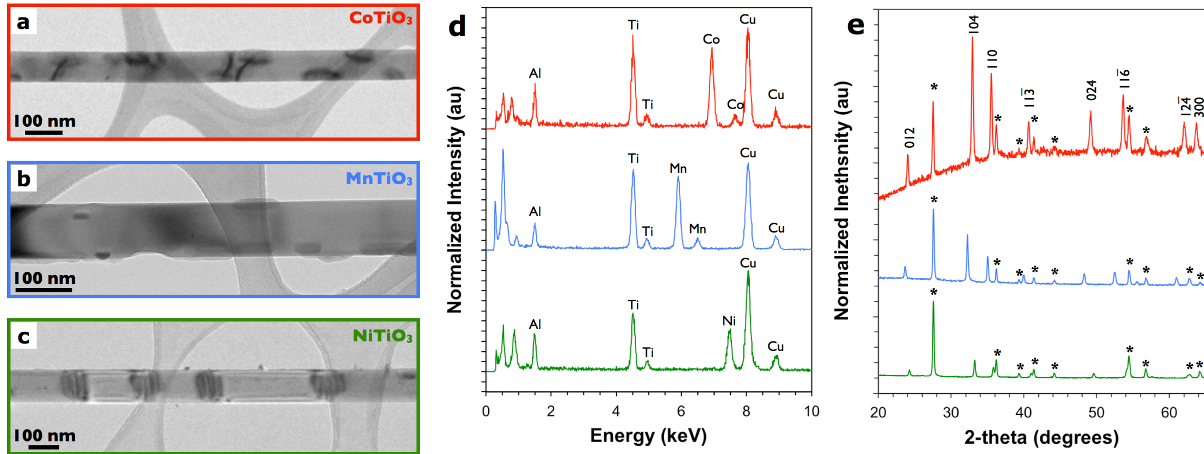

Figure 4.4: Rutile nanowires with various titanate surface particles. a-c) TEM images of rutile nanowires with surface particles of $CoTiO_3$ (**a**, red), $NiTiO_3$ (**b**, blue), and $MnTiO_3$ (**c**, green) after high-temperature conversion. **d**) EDS spectra of an ATiO$_3$ particle from each sample, indicating the approximately 1:1 A:Ti ratio in each each. Cu and Al peaks are from the sample holder and grid. **e**) X-ray diffraction patterns of the converted nanowires showing both rutile (*) and ATiO$_3$ (indexed for $CoTiO_3$, otherwise unlabeled). The patterns are normalized to the rutile 110 peak at 28°.

Increasing the amount of metal hydroxide coating using the CBD procedure was sucessful for Ni and Co films, but annealing at 825 °C lead to highly disordered and and irregularly-formed surface particles, even after 8-hour anneals. The annealing temperature was increased to 900 °C, which made it possible to obtain segmented nanowires with alternating regions of ATiO$_3$ and r-TiO$_2$ for A = Co, Ni. MTO segmented nanowires were not possible due to the poor coating of the $Mn(OH)_2$. For CTO, the interfaces were always observed to be perpendicular to the nanowire growth axis (Figure 4.5a). However, few perfect interfaces were observed in NTO/rutile segmented NWs and segments were typically bounded by segments with interfaces perpendicular to the nanowire axis (90°), 33° from the nanowire axis, and less commonly, 62° from the nanowire axis (Figure 4.5b). To confirm the elemental identity of each segment, Z-contrast STEM imaging was used to help identify the ATiO$_3$ segments from rutile segments (Figure 4.5c). Despite the small difference in atomic number (Z_{Ti} = 22, Z_A = 25-28), additional contrast was provided by the higher atomic density of ilmenite. To confirm that the brighter regions did in fact correspond to ilmenite, EDS line-scan spectra were collected to measure the spatial dependence of A (Figure 4.5d).

HRTEM imaging was used to identify lattice orientation at the different interfaces. The perpendicular interfaces were identified as TiO$_2$ <001> (the growth direction) and ATiO$_3$ <1-10>. The structure model of these surfaces (Figure 4.5e) helps visualize the similarity of the oxygen sublattice in these specific orientations, facilitating the conversion of rutile to corundum without disintegrating the overall crystal. In Figure 4.5f, we study a second epitaxial interface between ATiO$_3$ <100> and TiO$_2$ <0-31>.

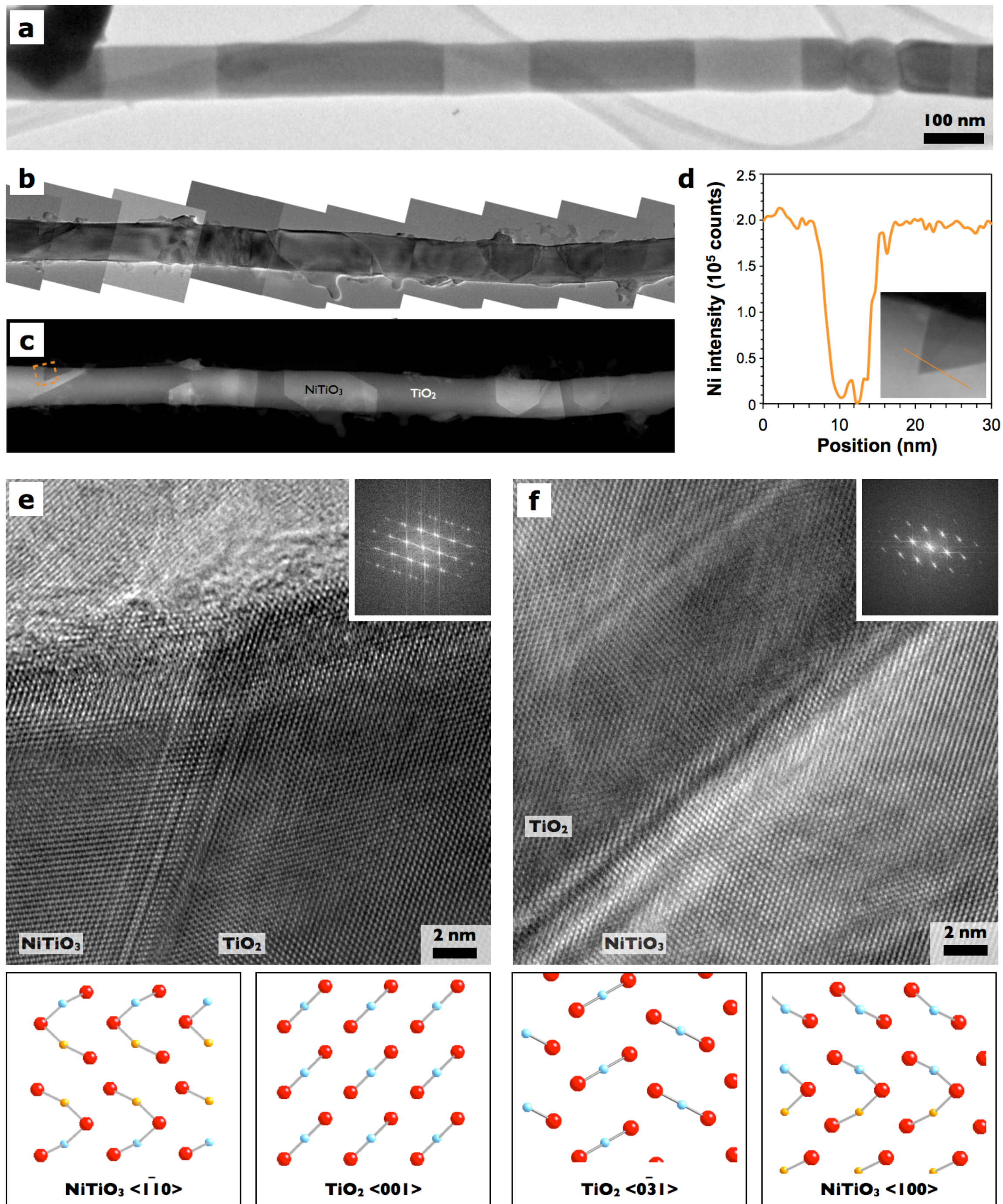

Figure 4.5: Heterojunction segmented nanowires. a) TEM image of a $CoTiO_3$/r-TiO_2 heterojunction nanowire. **b-c**) Bright-field TEM and HAADF Z-contrast STEM images of the same $NiTiO_3$/r-TiO_2 heterojunction nanowire (both panels are merged from several frames). The NTO regions appear more brightly than r-TiO_2 in (**c**) due to the higher atomic number of Ni, as well as the increased density of the corundum structure. **d**) Line-scan EDS was used to confirm that Ni was present only in the bright regions of (**c**). A plot of Ni characteristic x-ray emission intensity along the line indicated in the inset image, which corresponds to the boxed region in (**c**). **e-f**) HRTEM images of the two NTO-rutile interfaces characterized in (**d**). Inset images show the FFT pattern of the interface, while the lower panels indicate the lattice arrangement at each interface.

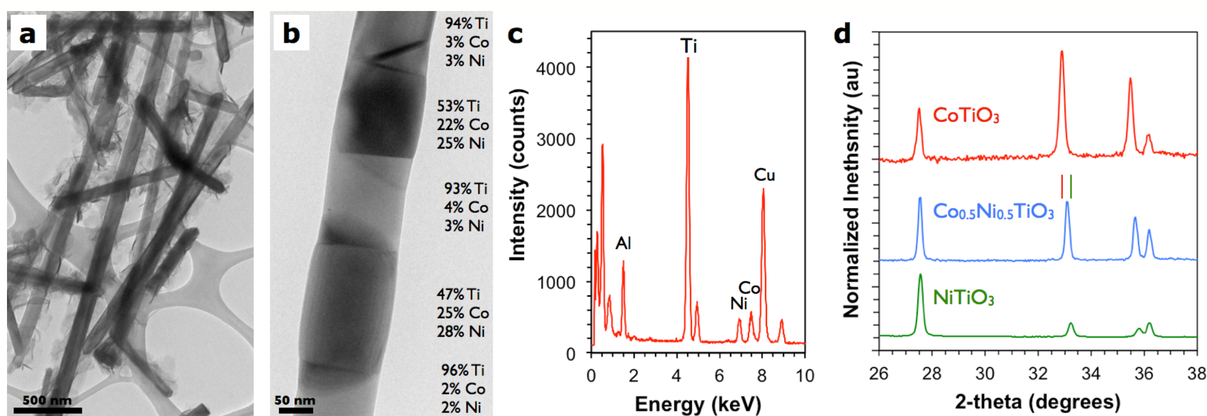

Figure 4.6: Quaternary $Co_{0.5}Ni_{0.5}TiO_3$ nanowires. a-b) Bright-field TEM images of a mixed $Co(OH)_2$ and $Ni(OH)_2$ coating on rutile nanowires (**a**) and segmented $Co_{0.5}Ni_{0.5}TiO_3$ nanowire (**b**) after high-temperature reaction. EDS measurements indicated that the *A*TiO3 segments are still 1:1 *A*:Ti and that the rutile segments are predominately Ti. **c**) EDS spectrum of $Co_{0.5}Ni_{0.5}TiO_3$. d) XRD patterns of $Co_{0.5}Ni_{0.5}TiO_3$, as well as $CoTiO_3$ and $NiTiO_3$ for comparison. Increasing nickel concentration causes a shift to higher angle (smaller lattice parameter) as the TiO_2 110 peak at 27° remains constant.

To demonstrate the flexibility of the conversion chemistry approach, the CBD growth solution was prepared with both 0.5 M $Co(NO_3)_2$ and 0.25 M $Ni(NO_3)_2$ and reacted normally (Figure 4.6). The r-TiO_2 nanowires were coated with a 47:53 mixture of $Co(OH)_2$ and $Ni(OH)_2$, as confirmed by EDS, which when annealed formed a single-phase of $Co_{1-x}Ni_xTiO_3$ ($x \approx 0.53$) to form segmented nanowires. EDS of the final nanowires showed the same Co:Ni ratio as in the metal coating, and indicated that there was 3% Co and 3% Ni in the r-TiO_2 segments. This is probably due to solid solution formation, but the large electron beam spot size and poorly defined interfaces also introduce uncertainty. XRD diffraction indicates that the $Co_{1-x}Ni_xTiO_3$ lattice parameters are intermediate of CTO and NTO.

With sufficient metal coating and annealing, it is possible to completely convert the rutile nanowires to $ATiO_3$ (A=Co, Ni). While the epitaxial match allows for the nanowires to convert without destroying the geometry, the resulting nanowires are not single-crystalline. There are two possible orientations for the $ATiO_3$ formation from r-TiO_2, leading to domains of one of two possible orientations, as shown by electron diffraction in Figure 4.7a. Because the interface and change in orientation leads to contrast during TEM imaging, EDS was used to confirm that all segments were 1:1 *A*:Ti. No evidence of rutile was observed in the XRD pattern of the fully-converted ilmenite nanowires, although for CTO nanowires, Co_2TiO_4 was observed due to a stoichiometric excess of $Co(OH)_2$ (Figure 4.7b). Using x-ray diffraction for the different ilmenite-rutile morphologies, the overall degree of conversion can be estimated by comparing the relative heights of the ilmenite 012 peak at 24° and rutile 110 peak at 28°.

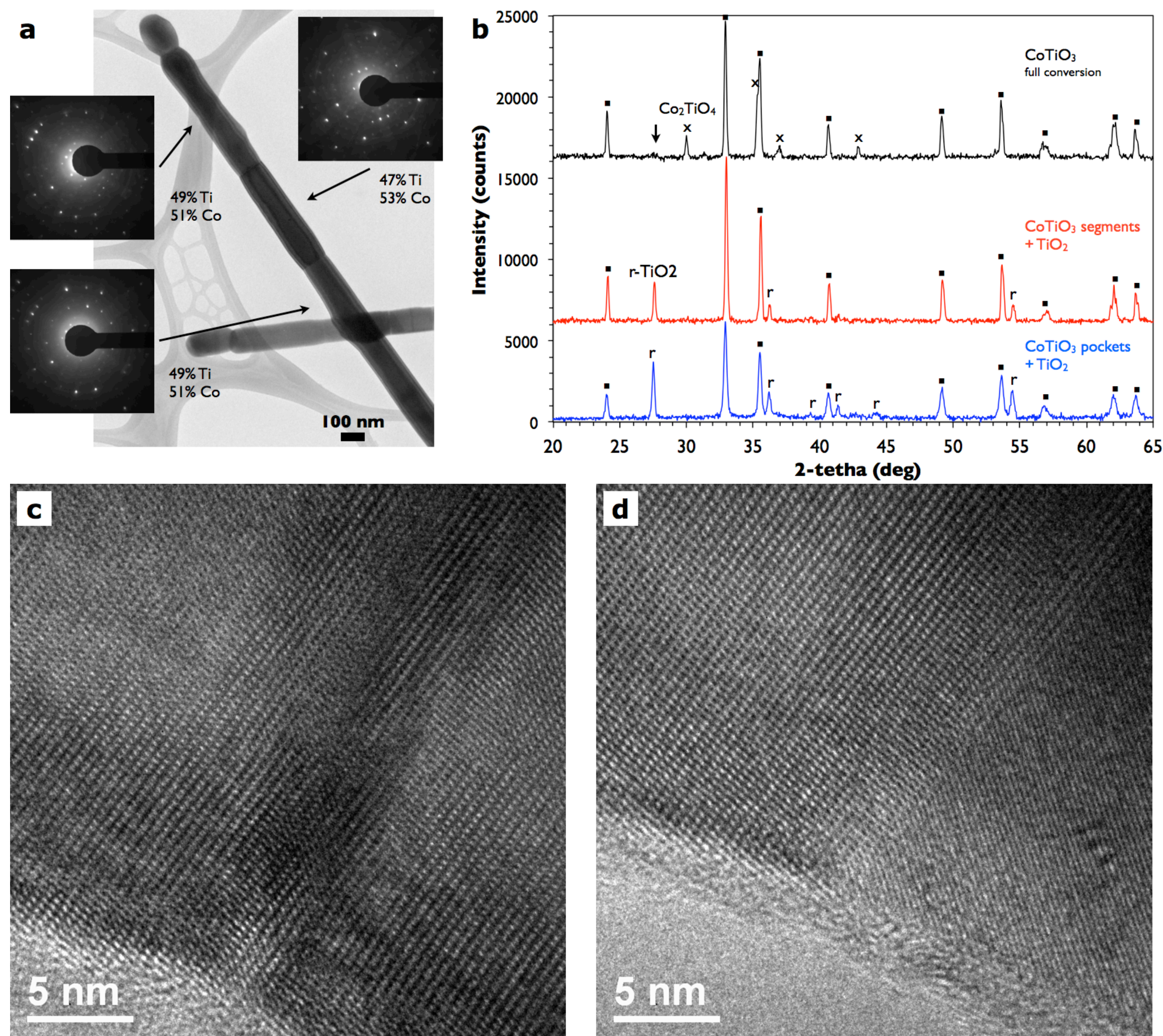

Figure 4.7: Fully-converted $CoTiO_3$ nanowires. a) Bright-field TEM image of a $CoTiO_3$ nanowire. This nanowire is fully converted, as confirmed by EDS spot measurements (software-calculated percentages of Ti and Co are indicated), but different crystal domains are visible. There are several domains for this 8-μm nanowire, which are arranged in one of two orientations as observed by electron diffraction (inset). **b**) The XRD patterns of the surface-decorated, segmented, and fully converted nanowires. The conversion progress can be estimated by comparing the $CoTiO_3$ 012 peak at 24° and the TiO_2 110 peak at 27°. No rutile is observed in the fully converted sample (position indicated by arrow), although an excess of deposited cobalt leads to the formation of a Co_2TiO_4 phase. **c-d**) HRTEM images of $CoTiO_3$-$CoTiO_3$ interfaces in fully converted nanowires.

4.4. Optical and photoelectrochemical properties

The improved visible light absorption of the ilmenite nanowire is readily apparent from the vivid color change in the materials after annealing, even for surface-decorated nanowires that contain a very small amount of ilmenite: CTO appears green, NTO appears yellow, CNTO appears blue, and MTO appears brown. The normalized absorbance spectra measured by an integrating-sphere-equipped spectrometer is shown in Figure 4.8. The absorbance characteristics of CNTO appear to be a hybrid of CTO and NTO, displaying the $Co^{2+} \rightarrow Ti^{4+}$ absorbance at 600 nm, but the band edge is shifted to higher energy, as in NTO.

The surface activity of the prepared ilmenite nanowires was evaluated by studying the overpotential voltage required to initiate the oxygen evolution reaction (OER). Overpotential is defined here as the potential at which water is oxidized under dark conditions with 0.5 mA/cm^2 of current flow. Electrodes were prepared on fluorine-doped-tin-oxide-coated glass by dropcasting a thing layer of ilmenite nanowires or ilmenite-rutile segmented nanowires and annealing at 450 °C for 30 minutes in air. While oriented arrays of nanowires with a well defined electrical contact to the substrate is preferred, there are no known conductive substrates that can survive the high-temperature preparation of ilmenite. The ilmenite working electrode, Pt mesh counter electrode, and Ag/AgCl reference electrode were used in a three electrode configuration with an electrolyte of 1 M KOH and 3 M NaCl (pH = 13.61). A Gamry Ref 600 potentiostat to construct current-voltage curves.

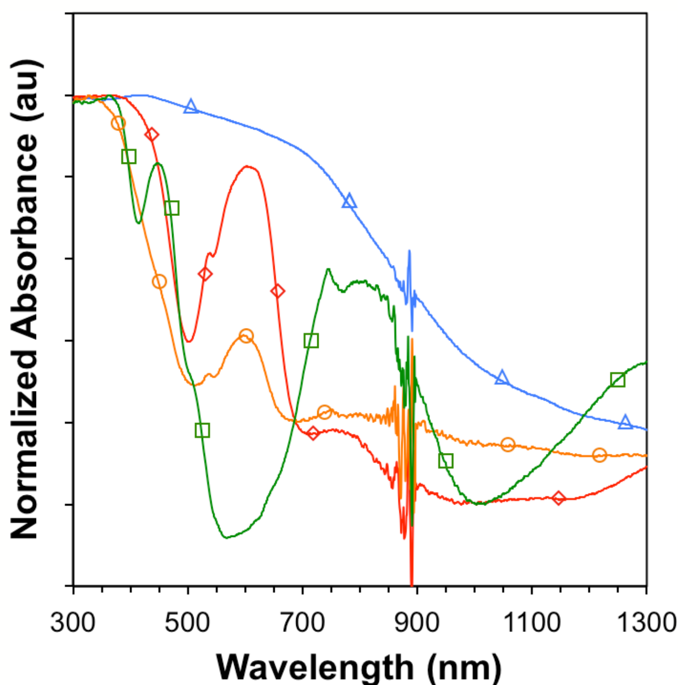

Figure 4.8: Absorbance spectra of ilmenite-rutile nanowires. Normalized absorbance spectra of $MnTiO_3$-surface decorated rutile nanowires (blue, triangles) and $CoTiO_3$- (green, squares), $NiTiO_3$- (red, diamonds), and $Co_{0.5}Ni_{0.5}TiO_3$- (orange, circles) rutile segmented nanowires. The noise at 900 nm is due to the detector change.

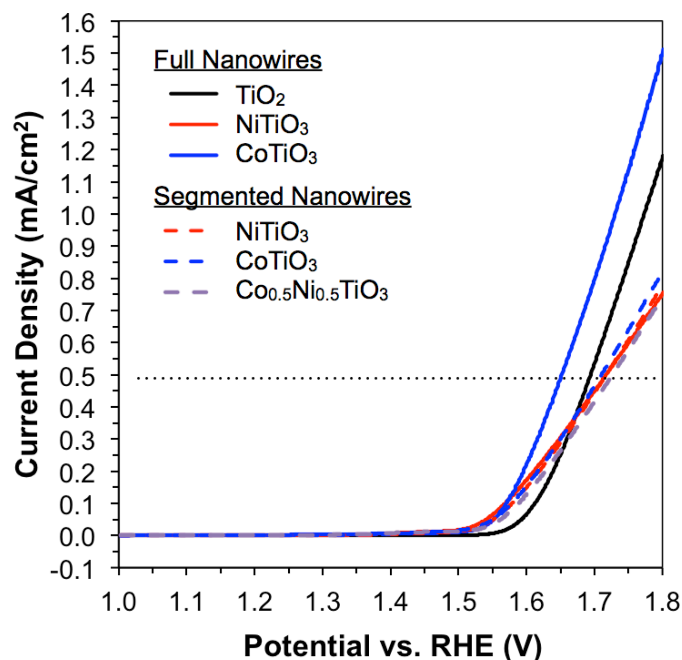

Figure 4.9: Overpotential required for water oxidation for *A*TiO_3 nanowire electrodes. I-V plot for water oxidation at pH 13.61 using electrodes prepared from TiO_2 (black), $NiTiO_3$ (red), and $CoTiO_3$ (blue) nanowires (solid lines), as well as $NiTiO_3$, $CoTiO_3$, and $Co_{0.5}Ni_{0.5}TiO_3$ (purple) segmented nanowires (dashed lines). The overpotential is defined as the potential necessary for 0.5 mA/cm^2 of current, indicated by intersection with the dotted line.

Overpotential measurements were collected on fully converted NTO and CTO nanowires, as well as NTO, CTO, and CNTO segmented nanowires, as well as rutile nanowires for comparison (Figure 4.9). The only material to outperform rutile was the fully converted CTO nanowires, although these wires were also contaminated with Co_2TiO_4, as observed by XRD (Figure 4.7b). All other samples were slightly behind rutile at 0.5 mA/cm^2, but the apparent slope suggests that these samples have much lower activity. The performance of CTO is similar to the improvements observed in Co-doped TiO_2 (*244*), but is less than conventional cocatalyst materials.

Because of the difficulty of preparing electrodes from the dispersed nanowire powders, the photocatalytic behavior of the ilmenite nanowires was also tested by measuring oxygen evolution under illumination. The powders (~2 mg) were dispersed in 3 mL of 5 mM $Fe_2(SO_4)_3$ solution to serve as a electron scavenger and loaded into a quartz cell (total volume 14 mL) with a stir bar. The cell was loaded into a glove box under argon atmosphere and purged by pumping under vacuum. The cell was illuminated by a 450 W xenon lamp and GC measurements were collected every 30 minutes to determine the oxygen and nitrogen concentration in the cell (N_2 indicates a leak and atmospheric oxygen contamination). In addition to IR light filters to reduce sample heating, a 400-nm long pass filter was used used in some experiments to reduce the amount of UV irradiation and test for visible light absorption.

Oxygen evolution measurements were tested for TiO_2 and for the ilmenite-decorated TiO_2 nanowires (Figure 4.10). As expected, rutile nanowires with the full illumination of the 450 W lamp were far more active than the other materials. While the CTO-decorated nanowires had

an evolution rate of 200 μmol g^{-1} hr^{-1} under full illumination, rutile had an estimated rate of 1750 μmol g^{-1} hr^{-1} (and depleted the sacrificial reagent in less than one hour). However, when a 400-nm long pass filter is used to reduce UV light, the rutile and CTO-decorated rutile had very similar evolution rates (21 and 23 μmol g^{-1} hr^{-1}, respectively). NTO-decorated rutile had an evolution rate of 72 μmol g^{-1} hr^{-1}, suggesting that the NTO is photoactive under visible wavelengths. MTO-decorated rutile was completely inactive.

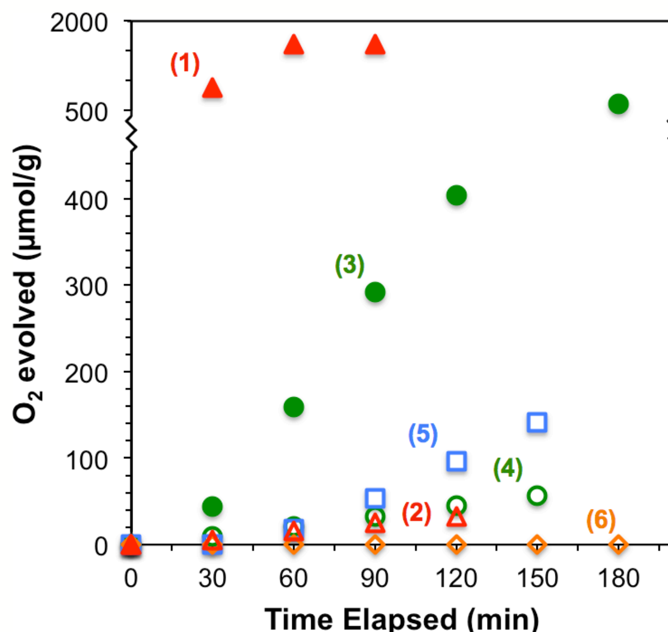

Figure 4.10: Oxygen evolution of *A*TiO_3-decorated rutile nanowires under illumination. Oxygen evolution (standardized by catalyst mass) as a function of time for as-grown TiO_2 nanowires (**1,2**, triangles) and TiO_2 nanowires with $CoTiO_3$ (**3,4**, circles), $NiTiO_3$ (**5**, squares), and $MnTiO_3$ (**6**, diamonds) surface decoration. All samples were measured in a homebuilt GC system contained in an Ar atmosphere. Powders were dispersed in a $Fe_2(SO_4)_3$ solution to serve as a sacrificial reagent. All samples were illuminated with a 450 W xenon lamp, but samples (**2, 4-6**, open symbols) had a 400-nm long pass filter installed to reduce UV irradiation. The rutile nanowires under full illumination (**1**) is estimated to produce 1750 μmol of O_2 g^{-1} hr^{-1} using the first two datapoints, but was limited by the sacrificial reagent.

5. Concluding Remarks

The results presented within this dissertation demonstrate the enormous opportunity presented by semiconductor nanostructures and materials chemistry to design new materials, both compositionally and morphologically, for advanced applications. In the case of optical materials, miniaturization towards nanoscale devices may allow for better control of light below the diffraction limit, which will lead to new devices and advances in microelectronics. In the case of energy applications, nanostructured materials will be absolutely essential to achieving high performance if we are to limit ourselves to inexpensive and abundant materials. Unfortunately, there are very few effective materials, nanostructured or not. While conversion chemistry has been demonstrated as a powerful tool for preparing new nanowire compositions, combinatorial and computational results are needed to discover interesting materials. Luckily, massive operations in these areas are underway.

The pharmaceutical industry has long relied on robotics for combinatorial chemistry. While this is one way forward, the sheer number of people in the world (or at least students enrolled in undergraduate chemistry) presents another potential combinatorial lab. The SHARK Project (Solar Hydrogen Activity Research Kit) has crowdsourced the mission to find suitable metal oxides for water oxidation photoanodes. In addition to the numerous independently-acting theoretical chemists interested in modeling materials, the Materials Genome Initiative is a federal program to develop computation methods for solving for everything from new PEC and thermoelectric materials to improved batteries and carbon capture materials. There is a great opportunity for collaboration between these research efforts and those involved with the synthesis of novel materials.

Bibliography

1. I. Freestone, N. Meeks, M. Sax, C. Higgitt. The Lycurgus Cup - A Roman nanotechnology. *Gold Bulletin* **40**, 270 (2007).
2. P. Sciau, *Nanoparticles in Ancient Materials: The Metallic Lustre Decorations of Medieval Ceramics, The Delivery of Nanoparticles* (InTech, 2012).
3. H. W. Kroto *et al.* C60: Buckminsterfullerene. *Nature* **318**, 162 (1985).
4. Q. L. Zhang *et al.* Reactivity of large carbon clusters: spheroidal carbon shells and their possible relevance to the formation and morphology of soot. *Journal of Physical Chemistry* **90**, 525 (1986).
5. E. Roduner. Size matters: why nanomaterials are different. *Chemical Society Reviews* **35**, 583 (2006).
6. C. B. Murray, D. J. Norris, M. G. Bawendi. Synthesis and characterization of nearly monodisperse CdE (E = sulfur, selenium, tellurium) semiconductor nanocrystallites. *Journal of the American Chemical Society* **115**, 8706 (1993).
7. R. S. Wagner, W. C. Ellis. Vapor-Liquid-Solid Mechanism of Single Crystal Growth. *Applied Physics Letters* **4**, 89 (1964).
8. J. ,. M. Baribeau, D. C. Houghton, T. E. Jackman, J. P. McCaffrey. Molecular Beam Epitaxy Growth of Ge on (100) Si. *Journal of The Electrochemical Society* **136**, 1158 (1989).
9. M. H. Huang *et al.* Room-Temperature Ultraviolet Nanowire Nanolasers. *Science* **292**, 1897 (2001).
10. M. Law *et al.* Nanoribbon Waveguides for Subwavelength Photonics Integration. *Science* **305**, 1269 (2004).
11. K. M. Rosfjord *et al.* Nanowire single-photon detector with an integrated optical cavity and anti-reflection coating. *Optics Express* **14**, 527 (2006).
12. P. Yang. Semiconductor nanowire building blocks: From flux line pinning to artificial photosynthesis. *MRS Bulletin* **37**, 806 (2012).
13. A. I. Hochbaum *et al.* Enhanced thermoelectric performance of rough silicon nanowires. *Nature* **451**, 163 (2008).
14. J. Tang *et al.* Solution-processed core-shell nanowires for efficient photovoltaic cells. *Nature Nanotechnology* **6**, 568 (2011).
15. C. K. Chan *et al.* High-performance lithium battery anodes using silicon nanowires. *Nature Nanotechnology* **3**, 31 (2008).
16. R. Zia, J. Schuller, A. Chandran, M. Brongersma. Plasmonics: the next chip-scale technology. *Materials Today* **9**, 20 (2006).
17. D. J. Sirbuly *et al.* Optical routing and sensing with nanowire assemblies. *Proceedings of the National Academy of Sciences* **102**, 7800 (2005).
18. P. J. Pauzauskie, P. Yang. Nanowire photonics. *Materials Today* **9**, 36 (2006).
19. Y. Li, F. Qian, J. Xiang, C. Lieber. Nanowire electronic and optoelectronic devices. *Materials Today* **9**, 18 (2006).

20. V. R. Almeida, C. A. Barrios, R. R. Panepucci, M. Lipson. All-optical control of light on a silicon chip. *Nature* **431**, 1081 (2004).

21. H. Rong *et al.* A continuous-wave Raman silicon laser. *Nature* **433**, 725 (2005).

22. H. Rong *et al.* An all-silicon Raman laser. *Nature* **433**, 292 (2005).

23. R. Yan *et al.* Nanowire-based single-cell endoscopy. *Nature Nanotechnology* **7**, 191 (2012).

24. D. J. Sirbuly *et al.* Multifunctional Nanowire Evanescent Wave Optical Sensors. *Advanced Materials* **19**, 61 (2007).

25. Y. Nakayama *et al.* Tunable nanowire nonlinear optical probe. *Nature* **447**, 1098 (2007).

26. R. N. Hall *et al.* Coherent Light Emission From GaAs Junctions. *Physical Review Letters* **9**, 366 (1962).

27. X. F. Duan, Y. Huang, R. Agarwal, C. M. Lieber. Single-nanowire electrically driven lasers. *Nature* **421**, 241 (2003).

28. Z. Zhang *et al.* Visible submicron microdisk lasers. *Applied Physics Letters* **90**, 111119 (2007).

29. T. W. Ebbesen *et al.* Extraordinary optical transmission through sub-wavelength hole arrays. *Nature* **391**, 667 (1998).

30. A. G. Brolo *et al.* Enhanced Fluorescence from Arrays of Nanoholes in a Gold Film. *Journal of the American Chemical Society* **127**, 14936 (2005).

31. N. Fang, H. Lee, C. Sun, X. Zhang. Sub-l Diffraction-Limited Optical Imaging with a Silver Superlens. *Science* **308**, 534 (2005).

32. N. E. Glass, A. A. Maradudin, V. Celli. Diffraction of light by a bigrating: Surface polariton resonances and electric field enhancements. *Physical Review B* **27**, 5150 (1983).

33. K. Kneipp *et al.* Extremely Large Enhancement Factors in Surface-Enhanced Raman Scattering for Molecules on Colloidal Gold Clusters. *Applied Spectroscopy* **52**, 1493 (1998).

34. S. Teeters-Kennedy *et al.* Extraordinary Infrared Transmission of a Stack of Two Metal Micromeshes. *The Journal of Physical Chemistry C* **111**, 124 (2006).

35. K. Okamoto *et al.* Surface-plasmon-enhanced light emitters based on InGaN quantum wells. *Nature Materials* **3**, 601 (2004).

36. M. T. Hill *et al.* Lasing in metal-insulator-metal sub-wavelength plasmonic waveguides. *Optics Express* **17**, 11107 (2009).

37. S.-H. Kwon *et al.* Subwavelength Plasmonic Lasing from a Semiconductor Nanodisk with Silver Nanopan Cavity. *Nano Letters* **10**, 3679 (2010).

38. A. Kinkhabwala *et al.* Large single-molecule fluorescence enhancements produced by a bowtie nanoantenna. *Nature Photonics* **3**, 654 (2009).

39. D. P. Fromm *et al.* Gap-Dependent Optical Coupling of Single "Bowtie" Nanoantennas Resonant in the Visible. *Nano Letters* **4**, 957 (2004).

40. R. Oulton, F. *et al.* Plasmon lasers at deep subwavelength scale. *Nature* **461**, 629 (2009).

41. M. A. Noginov *et al.* Demonstration of a spaser-based nanolaser. *Nature* **460**, 1110 (2009).

42. R.-M. Ma *et al.* Room-temperature sub-diffraction-limited plasmon laser by total internal reflection. *Nature Materials* **10**, 110 (2011).

43. C. Wu. Analysis of waste-heat thermoelectric power generators. *Applied Thermal Engineering* **16**, 63 (1996).

44. L. E. Bell. Cooling, Heating, Generating Power, and Recovering Waste Heat with Thermoelectric Systems. *Science* **321**, 1457 (2008).

45. J. Yang. Potential applications of thermoelectric waste heat recovery in the automotive industry. *24th International Conference on Thermoelectrics, 2005* 170 (2005).

46. G. J. Snyder, E. S. Toberer. Complex thermoelectric materials. *Nature Materials* **7**, 105 (2008).

47. A. Majumdar. Thermoelectricity in Semiconductor Nanostructures. *Science* **303**, 777 (2004).

48. L. D. Hicks, M. S. Dresselhaus. Effect of quantum-well structures on the thermoelectric figure of merit. *Physical Review B* **47**, 12727 (1993).

49. L. D. Hicks, M. S. Dresselhaus. Thermoelectric figure of merit of a one-dimensional conductor. *Physical Review B* **47**, 16631 (1993).

50. A. I. Boukai *et al.* Silicon nanowires as efficient thermoelectric materials. *Nature* **451**, 168 (2008).

51. J. Lim *et al.* Quantifying Surface Roughness Effects on Phonon Transport in Silicon Nanowires. *Nano Letters* **12**, 2475 (2012).

52. M. S. Dresselhaus *et al.* New directions for low-dimensional thermoelectric materials. *Advanced Materials* **19**, 1043 (2007).

53. R. Venkatasubramanian, E. Siivola, T. Colpitts, B. O'Quinn. Thin-film thermoelectric devices with high room-temperature figures of merit. *Nature* **413**, 597 (2001).

54. T. C. Harman, P. J. Taylor, M. P. Walsh, B. E. LaForge. Quantum dot superlattice thermoelectric materials and devices. *Science* **297**, 2229 (2002).

55. K. F. Hsu *et al.* Cubic AgPb*m*SbTe2+*m*: Bulk thermoelectric materials with high figure of merit. *Science* **303**, 818 (2004).

56. D. Kraemer *et al.* High-performance flat-panel solar thermoelectric generators with high thermal concentration. *Nature Materials* **10**, 532 (2011).

57. D. J. Bradwell, H. Kim, A. H. C. Sirk, D. R. Sadoway. Magnesium Antimony Liquid Metal Battery for Stationary Energy Storage. *Journal of the American Chemical Society* **134**, 1895 (2012).

58. H. Chen *et al.* Progress in electrical energy storage system: A critical review. *Progress in Natural Science* **19**, 291 (2009).

59. Z. Yang *et al.* Electrochemical Energy Storage for Green Grid. *Chemical Reviews* **111**, 3577 (2011).

60. F. Osterloh, E., B. Parkinson, A. Recent developments in solar water-splitting photocatalysis. *MRS Bulletin* **36**, 17 (2011).

61. A. Kudo, Y. Miseki. Heterogeneous photocatalyst materials for water splitting. *Chemical Society Reviews* **38**, 253 (2009).

62. A. J. Nozik. P-N Photoelectrolysis Cells. *Applied Physics Letters* **29**, 150 (1976).

63. S. Tabata, H. Nishida, Y. Masaki, K. Tabata. Stoichiometric photocatalytic decomposition of pure water in Pt/TiO2 aqueous suspension system. *Catalysis Letters* **34**, 245 (1995).

64. J. G. Mavroides, J. A. Kafalas, D. F. Kolesar. Photoelectrolysis of water in cells with SrTiO3 anodes. *Applied Physics Letters* **28**, 241 (1976).

65. A. Fujishima, K. Honda. Electrochemical Photolysis of Water at a Semiconductor Electrode. *Nature* **238**, 37 (1972).

66. G. Hitoki *et al.* An oxynitride, TaON, as an efficient water oxidation photocatalyst under visible light irradiation. *Chemical Communications* **16**, 1698 (2002).

67. P. G. Moses, d. W. Van, Chris G. Band bowing and band alignment in InGaN alloys. *Applied Physics Letters* **96**, 021908 (2010).

68. K. Maeda *et al.* GaN:ZnO Solid Solution as a Photocatalyst for Visible-Light-Driven Overall Water Splitting. *Journal of the American Chemical Society* **127**, 8286 (2005).

69. O. Khaselev, J. A. Turner. A Monolithic Photovoltaic-Photoelectrochemical Device for Hydrogen Production via Water Splitting. *Science* **280**, 425 (1998).

70. J. Barber. Photosynthetic energy conversion: natural and artificial. *Chemical Society Reviews* **38**, 185 (2009).

71. E. Garnett, P. Yang. Light Trapping in Silicon Nanowire Solar Cells. *Nano Letters* **10**, 1082 (2010).

72. M. D. Kelzenberg *et al.* Enhanced absorption and carrier collection in Si wire arrays for photovoltaic applications. *Nature Materials* **9**, 239 (2010).

73. M. Liu, L. S. de, Nathalie, H. Park. Water photolysis with a cross-linked titanium dioxide nanowire anode. *Chemical Science* **2**, 80 (2011).

74. M. G. Walter *et al.* Solar Water Splitting Cells. *Chemical Reviews* **110**, 6446 (2010).

75. U. Ozgur *et al.* A comprehensive review of ZnO materials and devices. *Journal of Applied Physics* **98**, 041301 (2005).

76. A. Djurišić, Y. H. Leung. Optical Properties of ZnO Nanostructures. *Small* **2**, 944 (2006).

77. K. Thonke *et al.* ZnO Nanostructures: Optical Resonators and Lasing. *Advances in Solid Solid State Physics* **48**, 39 (2009).

78. D. Vanmaekelbergh, L. K. van Vugt. ZnO nanowire lasers. *Nanoscale* **3**, 2783 (2011).

79. A. Janotti, C. G. Van De Walle. Fundamentals of zinc oxide as a semiconductor. *Reports on Progress in Physics* **72**, (2009).

80. H. Morkoc *et al.* Large-band-gap SiC, III-V nitride, and II-VI ZnSe-based semiconductor device technologies. *Journal of Applied Physics* **76**, 1363 (1994).

81. J. Wu. When group-III nitrides go infrared: New properties and perspectives. *Journal of Applied Physics* **106**, 011101 (2009).

82. S. Nakamura. The Roles of Structural Imperfections in InGaN-Based Blue Light-Emitting Diodes and Laser Diodes. *Science* **281**, 956 (1998).

83. K. Minegishi *et al.* Growth of p-type zinc oxide films by chemical vapor deposition. *Japanese Journal Of Applied Physics Part 2-Letters* **36**, L1453 (1997).

84. D. C. Look, B. Claflin. P-type doping and devices based on ZnO. *physica status solidi (b)* **241**, 624 (2004).

85. M.-T. Chen *et al.* Near UV LEDs Made with in Situ Doped p-n Homojunction ZnO Nanowire Arrays. *Nano letters* **10**, 4387 (2010).

86. P. W. Tasker. Stability of ionic-crystal surfaces. *Journal Of Physics C-Solid State Physics* **12**, 4977 (1979).

87. M. Suscavage *et al.* High quality hydrothermal ZnO crystals. *MRS Internet Journal of Nitride Semiconductor Research* **4**, (1999).

88. X. Wang, J. Song, J. Liu, Z. L. Wang. Direct-Current Nanogenerator Driven by Ultrasonic Waves. *Science* **316**, 102 (2007).

89. J. C. Johnson *et al.* Near-Field Imaging of Nonlinear Optical Mixing in Single Zinc Oxide Nanowires. *Nano Letters* **2**, 279 (2002).

90. A. B. M. A. Ashrafi *et al.* Growth and characterization of hypothetical zinc-blende ZnO films on GaAs(001) substrates with ZnS buffer layers. *Applied Physics Letters* **76**, 550 (2000).

91. S. Desgreniers. High-density phases of ZnO: Structural and compressive parameters. *Physical Review B* **58**, 14102 (1998).

92. J. F. Muth *et al.* Excitonic structure and absorption coefficient measurements of ZnO single crystal epitaxial films deposited by pulsed laser deposition. *Journal of Applied Physics* **85**, 7884 (1999).

93. A. Teke *et al.* Excitonic fine structure and recombination dynamics in single-crystalline ZnO. *Physical Review B* **70**, 195207 (2004).

94. H.-J. Egelhaaf, D. Oelkrug. Luminescence and nonradiative deactivation of excited states involving oxygen defect centers in polycrystalline ZnO. *Journal of Crystal Growth* **161**, 190 (1996).

95. R. Chen *et al.* Investigation of Structured Green-Band Emission and Electron-Phonon Interactions in Vertically Aligned ZnO Nanowires. *The Journal of Physical Chemistry C* **114**, 17889 (2010).

96. O. D. Jayakumar *et al.* Green emission from ZnO nanorods: Role of defects and morphology. *Scripta Materialia* **62**, 662 (2010).

97. Y. Jiao *et al.* Suppression of Green Emission in ZnO Nanorods-A Discussion on Surface and Interior Structural Quality Manipulation. *The Journal of Physical Chemistry C* **114**, 208 (2010).

98. R. Dingle. Luminescent Transitions Associated With Divalent Copper Impurities and the Green Emission from Semiconducting Zinc Oxide. *Physical Review Letters* **23**, 579 (1969).

99. C. W. Teng *et al.* Refractive indices and absorption coefficients of Mg*x*Zn1-*x*O alloys. *Applied Physics Letters* **76**, 979 (2000).

100. H. Yoshikawa, S. Adachi. Optical Constants of ZnO. *Japanese Journal of Applied Physics* **36**, 6237 (1997).

101. D. J. Gargas *et al.* Whispering Gallery Mode Lasing from Zinc Oxide Hexagonal Nanodisks. *ACS Nano* **4**, 3270 (2010).

102. J. M. Hvam. Exciton-exciton interaction and laser emission in high-purity ZnO. *Solid State Communications* **12**, 95 (1973).

103. F. H. Nicoll. Ultraviolet ZnO laser pumped by an electron beam. *Applied Physics Letters* **9**, 13 (1966).

104. D. M. Bagnall *et al.* Optically pumped lasing of ZnO at room temperature. *Applied Physics Letters* **70**, 2230 (1997).

105. P. Yu *et al.* Room-temperature gain spectra and lasing in microcrystalline ZnO thin films. *Journal of Crystal Growth* **184**, 601 (1998).

106. J. C. Johnson *et al.* Single Nanowire Lasers. *Journal Of Physical Chemistry B* **105**, 11387 (2001).

107. P. Yang *et al.* Controlled Growth of ZnO Nanowires and Their Optical Properties. *Advanced Functional Materials* **12**, 323 (2002).

108. D. Gargas, J., M. E. Toimil-Molares, P. Yang. Imaging Single ZnO Vertical Nanowire Laser Cavities Using UV-laser Scanning Confocal Microscopy. *Journal of the American Chemical Society* **131**, 2125 (2009).

109. B. E. A. Saleh, M. C. Teich, *Fundamentals of Photonics* (Wiley-Interscience, ed. 2nd, 2007).

110. Y. Chen *et al.* Stimulated emission and optical gain in ZnO epilayers grown by plasma-assisted molecular-beam epitaxy with buffers. *Applied Physics Letters* **78**, 1469 (2001).

111. S. L. McCall *et al.* Whispering-gallery mode microdisk lasers. *Applied Physics Letters* **60**, 289 (1992).

112. A. K. Bhowmik. Polygonal optical cavities. *Applied Optics* **39**, 3071 (2000).

113. J. Wiersig. Hexagonal dielectric resonators and microcrystal lasers. *Physical Review A* **67**, 023807 (2003).

114. K. J. Vahala. Optical microcavities. *Nature* **424**, 839 (2003).

115. M. Hovinen *et al.* Blue-green laser-emission from ZnSe quantum-well microresonators. *Applied Physics Letters* **63**, 3128 (1993).

116. L. Mahler *et al.* Vertically emitting microdisk lasers. *Nature Photonics* **3**, 46 (2009).

117. B. Min *et al.* High-Q surface-plasmon-polariton whispering-gallery microcavity. *Nature* **457**, 455 (2009).

118. K. Srinivasan, O. Painter. Linear and nonlinear optical spectroscopy of a strongly coupled microdisk-quantum dot system. *Nature* **450**, 862 (2007).

119. J. Wiersig *et al.* Direct observation of correlations between individual photon emission events of a microcavity laser. *Nature* **460**, 245 (2009).

120. A. Tamboli, C. *et al.* Room-temperature continuous-wave lasing in GaN/InGaN microdisks. *Nature Photonics* **1**, 61 (2007).

121. Q. Song, H. Cao, S. T. Ho, G. S. Solomon. Near-IR subwavelength microdisk lasers. *Applied Physics Letters* **94**, 061109 (2009).

122. T. Nobis *et al.* Whispering gallery modes in nanosized dielectric resonators with hexagonal cross section. *Physical Review Letters* **93**, 103903 (2004).

123. D. Wang *et al.* Lasing in whispering gallery mode in ZnO nanonails. *Journal of Applied Physics* **99**, 093112 (2006).

124. C. Kim *et al.* Whispering-gallery-modelike-enhanced emission from ZnO nanodisk. *Applied Physics Letters* **88**, 093104 (2006).

125. T. Nobis *et al.* Optical whispering gallery modes in dodecagonal zinc oxide microcrystals. *Superlattices and Microstructures* **42**, 333 (2007).

126. L. Sun *et al.* Direct observation of whispering gallery mode polaritons and their dispersion in a ZnO tapered microcavity. *Physical Review Letters* **100**, 156403 (2008).

127. X. Zhang *et al.* Whispering gallery modes in single triangular ZnO nanorods. *Optics Letters* **34**, 2533 (2009).

128. S. Nakamura, T. Mukai, M. Senoh. Candela-class high-brightness InGaN/AlGaN double-heterostructure blue-light-emitting diodes. *Applied Physics Letters* **64**, 1687 (1994).

129. M.-P. Lu, M.-Y. Lu, L.-J. Chen. p-Type ZnO nanowires: From synthesis to nanoenergy. *Nano Energy* **1**, 247 (2012).

130. U. Ozgur, D. Hofstetter, H. Morkoc. ZnO Devices and Applications: A Review of Current Status and Future Prospects. *Proceedings of the IEEE* **98**, 1255 (2010).

131. D. C. Look *et al.* Evidence for Native-Defect Donors in n-Type ZnO. *Physical Review Letters* **95**, 225502 (2005).

132. d. W. Van, Chris G. Hydrogen as a Cause of Doping in Zinc Oxide. *Physical Review Letters* **85**, 1012 (2000).

133. A. F. Kohan, G. Ceder, D. Morgan, d. W. Van, Chris G. First-principles study of native point defects in ZnO. *Physical Review B* **61**, 15019 (2000).

134. T. S. Bjørheim *et al.* H and Li Related Defects in ZnO and Their Effect on Electrical Properties. *The Journal of Physical Chemistry C* **116**, 23764 (2012).

135. A. Kovalenko *et al.* Evidence of Unintentional n-Doping in ZnO Nanorods. *The Journal of Physical Chemistry C* **114**, 9498 (2010).

136. W.-J. Lee, J. Kang, K. J. Chang. Defect properties and p-type doping efficiency in phosphorus-doped ZnO. *Physical Review B* **73**, 024117 (2006).

137. C. H. Park, S. B. Zhang, S.-H. Wei. Origin of p-type doping difficulty in ZnO: The impurity perspective. *Physical Review B* **66**, 073202 (2002).

138. U. Wahl, J. G. Correia, S. Decoster, T. Mendonca. Lattice location of the group V elements As and Sb in ZnO. *Proceedings of SPIE* **7603**, (2010).

139. S. Limpijumnong *et al.* Alternative sources of p-type conduction in acceptor-doped ZnO. *Applied Physics Letters* **97**, 072112 (2010).

140. A. Janotti, C. G. Van De Walle. Native point defects in ZnO. *Physical Review B* **76**, 165202 (2007).

141. A. Janotti, E. Snow, C. G. Van De Walle. A pathway to p-type wide-band-gap semiconductors. *Applied Physics Letters* **95**, 172109 (2009).

142. S. B. Zhang, S.-H. Wei, A. Zunger. Intrinsic n-type versus p-type doping asymmetry and the defect physics of ZnO. *Physical Review B* **63**, 075205 (2001).

143. B. Xiang *et al.* Rational synthesis of p-type zinc oxide nanowire arrays using simple chemical vapor deposition. *Nano letters* **7**, 323 (2007).

144. E. C. Lee, K. J. Chang. Possible p-type doping with group-I elements in ZnO. *Physical Review B* **70**, 115210 (2004).

145. M. G. Wardle, J. P. Goss, P. R. Briddon. Theory of Li in ZnO: A limitation for Li-based p-type doping. *Physical Review B* **71**, 155205 (2005).

146. E.-C. Lee, Y.-S. Kim, Y.-G. Jin, K. J. Chang. Compensation mechanism for N acceptors in ZnO. *Physical Review B* **64**, 085120 (2001).

147. K. K. Kim *et al.* Realization of p-type ZnO thin films via phosphorus doping and thermal activation of the dopant. *Applied Physics Letters* **83**, 63 (2003).

148. M.-P. Lu *et al.* Piezoelectric Nanogenerator Using p-Type ZnO Nanowire Arrays. *Nano letters* **9**, 1223 (2009).

149. Y. R. Ryu *et al.* Synthesis of p-type ZnO films. *Journal of Crystal Growth* **216**, 330 (2000).

150. Y. R. Ryu, T. S. Lee, H. W. White. Properties of arsenic-doped p-type ZnO grown by hybrid beam deposition. *Applied Physics Letters* **83**, 87 (2003).

151. S. Chu *et al.* Electrically pumped ultraviolet ZnO diode lasers on Si. *Applied Physics Letters* **93**, 181106 (2008).

152. S. Limpijumnong, S. B. Zhang, S.-H. Wei, C. H. Park. Doping by Large-Size-Mismatched Impurities: The Microscopic Origin of Arsenic- or Antimony-Doped p-Type Zinc Oxide. *Physical Review Letters* **92**, 155504 (2004).

153. O. Schmidt *et al.* Effects of an Electrically Conducting Layer at the Zinc Oxide Surface. *Japanese Journal of Applied Physics* **44**, 7271

154. O. Schmidt *et al.* Analysis of a conducting channel at the native zinc oxide surface. *Superlattices and Microstructures* **39**, 8 (2006).

155. J. Goldberger, D. J. Sirbuly, M. Law, P. Yang. ZnO nanowire transistors. *Journal Of Physical Chemistry B* **109**, 9 (2005).

156. D. C. Look. Quantitative analysis of surface donors in ZnO. *Surface Science* **601**, 5315 (2007).

157. C. Swartz, H. Transport and surface conductivity in ZnO. *Journal of Materials Research* **27**, 2205 (2012).

158. S. Lany, A. Zunger. Anion vacancies as a source of persistent photoconductivity in II-VI and chalcopyrite semiconductors. *Physical Review B* **72**, 035215 (2005).

159. B. Claflin, D. C. Look, S. J. Park, G. Cantwell. Persistent n-type photoconductivity in p-type ZnO. *Journal of Crystal Growth* **287**, 16 (2006).

160. T. Ohgaki *et al.* Positive Hall coefficients obtained from contact misplacement on evident n-type ZnO films and crystals. *Journal of Materials Research* **23**, 2293 (2008).

161. O. Bierwagen, T. Ive, d. W. Van, Chris G., J. S. Speck. Causes of incorrect carrier-type identification in van der Pauw-Hall measurements. *Applied Physics Letters* **93**, 242108 (2008).

162. D. R. Khanal, J. Wu. Gate coupling and charge distribution in nanowire field effect transistors. *Nano letters* **7**, 2778 (2007).

163. M. H. Huang *et al.* Catalytic growth of zinc oxide nanowires by vapor transport. *Advanced Materials* **13**, 113 (2001).

164. G.-D. Yuan *et al.* Tunable n-type conductivity and transport properties of Ga-doped ZnO nanowire arrays. *Advanced Materials* **20**, 168 (2008).

165. B. Y. Zhang *et al.* Investigation on the formation mechanism of p-type Li–N dual-doped ZnO. *Applied Physics Letters* **97**, 222101 (2010).

166. H. Q. Yan, R. He, J. Pham, P. Yang. Morphogenesis of One-Dimensional ZnO Nano-and Microcrystals. *Advanced Materials* **15**, 402 (2003).

167. H. Q. Yan *et al.* Dendritic nanowire ultraviolet laser array. *Journal of the American Chemical Society* **125**, 4728 (2003).

168. J. Fallert *et al.* Lasing dynamics in single ZnO nanorods. *Optics Express* **16**, 1125 (2008).

169. M. Zimmler, A. *et al.* Laser action in nanowires: Observation of the transition from amplified spontaneous emission to laser oscillation. *Applied Physics Letters* **93**, 051101 (2008).

170. R. E. Slusher *et al.* Threshold characteristics of semiconductor microdisk lasers. *Applied Physics Letters* **63**, 1310 (1993).

171. R. Ushigome *et al.* GaInAsP microdisk injection laser with benzocyclobutene polymer cladding and its athermal effect. *Japanese Journal of Applied Physics Part 1* **41**, 6364 (2002).

172. J. C. Johnson, H. Q. Yan, P. Yang, R. J. Saykally. Optical cavity effects in ZnO nanowire lasers and wave-guides. *Journal Of Physical Chemistry B* **107**, 8816 (2003).

173. A. Taflove, S. C. Hagness, *Computational Electrodynamics: The Finite-Difference Time-Domain Method, Third Edition* (Artech, Norwood, 2000).

174. A. Farjadpour *et al.* Improving accuracy by subpixel smoothing in the finite-difference time domain. *Optics Letters* **31**, 2972 (2006).

175. S.-W. Chang, S. Chuang, Lien. Fundamental Formulation for Plasmonic Nanolasers. *IEEE Journal of Quantum Electronics* **45**, 1004 (2009).

176. J. Lee *et al.* p-Type Conduction Characteristics of Lithium-Doped ZnO Nanowires. *Advanced Materials* **23**, 4183 (2011).

177. T. T. Zhao *et al.* Growth ambient dependent electrical properties of lithium and nitrogen dual-doped ZnO films prepared by radio-frequency magnetron sputtering. *Thin Solid Films* **518**, 3289 (2010).

178. O. Hayden *et al.* Fully Depleted Nanowire Field-Effect Transistor in Inversion Mode. *Small* **3**, 230 (2007).

179. H. Kasper. Neuartige phasen mit wurtzitahnlichen strukturen im system ZnO-In2O3. *Zeitschrift fur Anorganische und Allgemeine Chemie* **349**, 113 (1967).

180. P. J. Cannard, R. J. D. Tilley. New intergrowth phases in the ZnO-In2O3 system. *Journal of Solid State Chemistry* **73**, 418 (1988).

181. T. Moriga *et al*. Phase Relationships and Physical Properties of Homologous Compounds in the Zinc Oxide-Indium Oxide System. *Journal of the American Ceramic Society* **81**, 1310 (1998).

182. N. Kimizuka, T. Morhi. Structural classification of *R*AO3(*M*O)*n* compounds (*R* =Sc, In, Y, or lanthanides; *A* = Fe(III), Ga, Cr, or Al; *M* =divalent cation; *n* = 1–11). *Journal of Solid State Chemistry* **78**, 98 (1989).

183. N. Kimizuka, M. Isobe, M. Nakamura, T. Mohri. Syntheses and Crystallographic Data of the Homologous Compounds InFeO3(ZnO)*m*, (*m* = 1, 2, 3, 7, 11, 13, 15, and 19) and Fe2O3(ZnO)*m* (*m* = 8 and 9) in the In2O3-ZnFe2O4-ZnO System. *Journal of Solid State Chemistry* **103**, 394 (1993).

184. N. Kimizuka, M. Isobe, M. Nakamura. Syntheses and single-crystal data of homologous compounds, In2O3(ZnO)*m* (*m* = 3, 4, and 5), InGaO3(ZnO)3, and Ga2O3(ZnO)*m* (*m* = 7, 8, 9, and 16) in the In2O3–ZnGa2O4–ZnO system. *Journal of Solid State Chemistry* **116**, 170 (1995).

185. M. Nakamura, N. Kimizuka, T. Mohri. The phase relations in the In2O3–Ga2ZnO4–ZnO system at 1350° C. *Journal of Solid State Chemistry* **93**, 298 (1991).

186. Y. Yan *et al*. Polytypoid structures in annealed In2O3-ZnO films. *Applied Physics Letters* **73**, 2585 (1998).

187. Y. Yan, J. L. F. Da Silva, S.-H. Wei, M. Al-Jassim. Atomic structure of In2O3–ZnO systems. *Applied Physics Letters* **90**, 261904 (2007).

188. Isobe, M., Kimizuka, N., Nakamura, M., Mohri, T. Structures of LuFeO3(ZnO)*m* (*m*=1, 4, 5 and 6). *Acta Crystallographica Section C* **50**, 332 (1994).

189. N. Uchida, Y. Bando, M. Nakamura, N. Kimizuka. High-resolution Electron Microscopy of Homologous Compounds InFeO3(ZnO)*m*. *Journal of Electron Microscopy* **43**, 146 (1994).

190. C. Li, Y. Bando, M. Nakamura, N. Kimizuka. Relation between In ion ordering and crystal structure variation in homologous compounds In*M*O3(ZnO)*m* (*M*=Al and In; *m*=integer). *Micron* **31**, 543 (2000).

191. C. F. Li, Y. Bando, M. Nakamura, N. Kimizuka. Antiphase modulated structure of Fe2O3(ZnO)15 studied by high-resolution electron microscopy. *Journal of Solid State Chemistry* **142**, 174 (1999).

192. C. Li, Y. Bando, M. Nakamura, N. Kimizuka. A modulated structure of ln2O3(ZnO)*m* as revealed by high-resolution electron microscopy. *Journal of Electron Microscopy* **46**, 119 (1997).

193. J. L. F. Da Silva, Y. F. Yan, S. H. Wei. Rules of structure formation for the homologous In*M*O3(ZnO)*n* compounds. *Physical Review Letters* **100**, 255501 (2008).

194. M. Ohtaki, T. Tsubota, K. Eguchi, H. Arai. High-temperature thermoelectric properties of (Zn1-*x*Al*x*)O. *Journal of Applied Physics* **79**, 1816 (1996).

195. H. Hosono. Electrical and Photonic Functions in Transparent Oxide Semiconductors: Utilization of Built-in Nanostructure. *Materials Research Society Symposium Proceedings* **796**, 87 (2004).

196. A. Kudo, I. Mikami. New In2O3(ZnO)*m* Photocatalysts with Laminal Structure for Visible Light-induced H2 or O2 Evolution from Aqueous Solutions Containing Sacrificial Reagents. *Chemistry Letters* **27**, 1027 (1998).

197. H. Ohta, W. S. Seo, K. Koumoto. Thermoelectric properties of homologous compounds in the ZnO-In2O3 system. *Journal of the American Ceramic Society* **79**, 2193 (1996).

198. J. He, Y. Liu, R. Funahashi. Oxide thermoelectrics: The challenges, progress, and outlook. *Journal of Materials Research* **26**, 1762 (2011).

199. M. Kazeoka, H. Hiramatsu, W. S. Seo, K. Koumoto. Improvement in thermoelectric properties of (ZnO)5In2O3 through partial substitution of yttrium for indium. *Journal of Materials Research* **13**, 523 (1998).

200. Y. Masuda *et al.* Structure and thermoelectric transport properties of isoelectronically substituted (ZnO)5In2O3. *Journal of Solid State Chemistry* **150**, 221 (2000).

201. S. Isobe *et al.* Thermoelectric Performance of Yttrium-substituted (ZnO)5In2O3 Improved through Ceramic Texturing. *Japanese Journal of Applied Physics* **41**, 731 (2002).

202. H. Kaga, R. Asahi, T. Tani. Thermoelectric properties of highly textured Ca-doped (ZnO)*m*In2O3 ceramics. *Japanese Journal of Applied Physics* **43**, 7133 (2004).

203. H. Ohta *et al.* Single-crystalline films of the homologous series InGaO3(ZnO)*m* grown by reactive solid-phase epitaxy. *Advanced Functional Materials* **13**, 139 (2003).

204. J. S. Jie, G. Z. Wang, X. H. Han, J. G. Hou. Synthesis and characterization of ZnO:In nanowires with superlattice structure. *Journal of Physical Chemistry B* **108**, 17027 (2004).

205. C. W. Na, S. Y. Bae, J. Park. Short-period superlattice structure of Sn-doped In2O3(ZnO)4 and In2O3(ZnO)5 nanowires. *Journal of Physical Chemistry B* **109**, 12785 (2005).

206. D. P. Li, G. Z. Wang, Q. H. Yang, X. Xie. Synthesis and photoluminescence of InGaO3(ZnO)*m* nanowires with perfect superlattice structure. *The Journal of Physical Chemistry C* **113**, 21512 (2009).

207. N. W. Wang, Y. H. Yang, G. W. Yang. Indium Oxide−zinc Oxide Nanosized Heterostructure and Whispering Gallery Mode Luminescence Emission. *The Journal of Physical Chemistry C* **113**, 15480 (2009).

208. L. Xu *et al.* Synthesis and Characterization of Indium-Doped ZnO Nanowires with Periodical Single−Twin Structures. *Journal Of Physical Chemistry B* **110**, 6637 (2006).

209. N. Kimizuka, T. Mohri. Spinel, YbFe2O4, and Yb2Fe3O7 Types of Structures for Compounds in the ln2O3 and Sc2O3–*A*2O3–*B*O Systems [*A*: Fe, Ga, or Al; *B*: Mg, Mn, Fe, Ni, Cu, or Zn] at Temperatures over 1000 °C. *Journal of Solid State Chemistry* **60**, 382 (1985).

210. H. Okamoto, *Fe-In (Iron-Indium), Binary Alloy Phase Diagrams* (ASM International, Materials Park, Ohio, ed. 2, 1990), pp. 1712-1714.

211. V. Raghavan, *The Fe-In-O (Iron-Indium-Oxygen) System, Phase Diagrams Ternary Iron Alloys* (Indian Institute of Metals, Calcutta, 1989), pp. 150-152.

212. R. W. Hewitt, N. Winograd. Oxidation of polycrystalline indium studied by x-ray photoelectron spectroscopy and static secondary ion mass spectroscopy. *Journal of Applied Physics* **51**, 2620 (1980).

213. I. Broser *et al.*, *Physics of II-VI and I-VII Compounds, Semimagnetic Semiconductors* (Springer-Verlag, New York, 1982).

214. D. G. Thomas. The diffusion and precipitation of indium in zinc oxide. *Journal of Physics and Chemistry of Solids* **9**, 31 (1959).

215. P. Erhart, K. Albe. Diffusion of zinc vacancies and interstitials in zinc oxide. *Applied Physics Letters* **88**, 201918 (2006).

216. T. Nakagawa *et al.* Diffusion model of gallium in single-crystal ZnO proposed from analysis of concentration-dependent profiles based on the Fermi-level effect. *Japanese Journal of Applied Physics* **46**, 4099 (2007).

217. T. Nakagawa *et al.* Analysis of indium diffusion profiles based on the Fermi-level effect in single-crystal zinc oxide. *Japanese Journal of Applied Physics* **47**, 7848 (2008).

218. G. Popovici *et al.* Impurity contamination of GaN epitaxial films from the sapphire, SiC and ZnO substrates. *Applied Physics Letters* **71**, 3385 (1997).

219. X. Liu *et al.* Novel photoluminescence properties of InAlO3(ZnO) msuperlattice nanowires. *Chinese Physics B* **20**, 078101 (2011).

220. L. Shi *et al.* Measuring thermal and thermoelectric properties of one-dimensional nanostructures using a microfabricated device. *Journal of Heat Transfer* **125**, 881 (2003).

221. K. Nomura *et al.* Thin-film transistor fabricated in single-crystalline transparent oxide semiconductor. *Science* **300**, 1269 (2003).

222. K. Nomura *et al.* Carrier transport in transparent oxide semiconductor with intrinsic structural randomness probed using single-crystalline InGaO3(ZnO)5 films. *Applied Physics Letters* **85**, 1993 (2004).

223. A. Shakouri, J. E. Bowers. Heterostructure integrated thermionic coolers. *Applied Physics Letters* **71**, 1234 (1997).

224. L. W. Whitlow, T. Hirano. Superlattice applications to thermoelectricity. *Journal of Applied Physics* **78**, 5460 (1995).

225. R. T. Senger, K. K. Bajaj. Optical properties of confined polaronic excitons in spherical ionic quantum dots. *Physical Review B* **68**, 045313 (2003).

226. O. Malochkin, W. S. Se, K. Koumoto. Thermoelectric properties of (ZnO)5In2O3 single crystal grown by a flux method. *Japanese Journal of Applied Physics Part 2-Letters* **43**, L194 (2004).

227. Z. Alahmed, H. Fu. Polar semiconductor ZnO under inplane tensile strain. *Physical Review B* **77**, 045213 (2008).

228. H. Gleskova *et al.* Field-effect mobility of amorphous silicon thin-film transistors under strain. *Journal of Non-Crystalline Solids* **338-340**, 732 (2004).

229. G. Chen, A. Narayanaswamy, C. Dames. Engineering nanoscale phonon and photon transport for direct energy conversion. *Superlattices and Microstructures* **35**, 161 (2004).

230. U. Ozgur *et al.* Thermal conductivity of bulk ZnO after different thermal treatments. *Journal of Electronic Materials* **35**, 550 (2006).

231. C. Chiritescu *et al.* Ultralow thermal conductivity in disordered, layered WSe2 crystals. *Science* **315**, 351 (2007).

232. L. Fang *et al.* Thermoelectric and magnetothermoelectric properties of In-doped nano-ZnO thin films prepared by RF magnetron sputtering. *Journal of Superconductivity and Novel Magnetism* **23**, 889 (2010).

233. A. Agui, M. Mizumaki. Intermetallic charge transfer and band gap of MTiO3 (M = Mn, Fe, Co, and Ni) studied by O 1*s*-edge X-ray emission spectroscopy. *Journal of Electron Spectroscopy and Related Phenomena* **184**, 463 (2011).

234. C. Gutierrez, P. Salvador, J. B. Goodenough. New semiconducting oxide photoanodes for water splitting in a photoelectrochemical cell: Electrochemistry of n-type NiTiO3. *Journal of Electroanalytical Chemistry and Interfacial Electrochemistry* **134**, 325 (1982).

235. P. Salvador, C. Gutierrez, J. B. Goodenough. Photoelectrochemical Properties of n-type NiTiO3. *Journal of Applied Physics* **53**, 7003 (1982).

236. D. S. Ginley, M. A. Butler. The photoelectrolysis of water using iron titanate anodes. *Journal of Applied Physics* **48**, 2019 (1977).

237. L. G. J. De Haart, A. J. De Vries, G. Blasse. Photoelectrochemical properties of MgTiO3 and other titanates with the ilmenite structure. *Materials Research Bulletin* **19**, 817 (1984).

238. P. H. M. De Korte, G. Blasse. Water photoelectrolysis using nickel titanate and niobate as photoanodes. *Journal of Solid State Chemistry* **44**, 150 (1982).

239. Y. Oosawa *et al*. Photocatalytic Hydrogen Evolution and Oxygen Evolution Over Ternary Titanates and Relationship Between Physical-Properties and Kinetic-Properties. *New Journal of Chemistry* **13**, 435 (1989).

240. J. Barber. Photosynthetic energy conversion: natural and artificial. *Chemical Society Reviews* **38**, 185 (2008).

241. M. García-Mota *et al*. Tailoring the Activity for Oxygen Evolution Electrocatalysis on Rutile TiO2(110) by Transition-Metal Substitution. *ChemCatChem* **3**, 1607 (2011).

242. B. Limburg, E. Bouwman, S. Bonnet. Molecular water oxidation catalysts based on transition metals and their decomposition pathways. *Coordination Chemistry Reviews* **256**, 1451 (2012).

243. F. Jiao, H. Frei. Nanostructured cobalt and manganese oxide clusters as efficient water oxidation catalysts. *Energy & Environmental Science* **3**, 1018 (2010).

244. B. Liu, H. M. Chen, et al., P. Yang. Large-Scale Synthesis of Transition-metal Doped TiO2 Nanowires with Controllable Overpotential. *Journal of the American Chemical Society,* submitted (2013).

245. Y. Mao, S. Banerjee, S. S. Wong. Large-Scale Synthesis of Single-Crystalline Perovskite Nanostructures. *Journal of the American Chemical Society* **125**, 15718 (2003).